A Study of Radiative Muon-Pair Events at Z^0 Energies and limits on an additional Z' Gauge Boson

Simon Charles Blyth

St. Hugh's College, Oxford

A thesis submitted for the degree of Doctor of Philosophy
at the University of Oxford

Trinity Term 1994

A Study of Radiative Muon-Pair Events at Z^0 Energies and limits on an additional Z' Gauge Boson

Simon Charles Blyth
St. Hugh's College, Oxford

A thesis submitted for the degree of Doctor of Philosophy
at the University of Oxford

Trinity Term 1994
31/10/94

Abstract

An analysis is reported on the channel $e^+e^- \rightarrow \mu^+\mu^-(n\gamma)$, n=1,2.., using data taken with the DELPHI detector at LEP from 1990 to 1992. Differential cross sections of the radiative photons as a function of photon energy and of the angle between the photon and the muon are presented. The data are compared to the results of Standard Model calculations for this channel, and no significant deviations are observed.

The data are also used to extract the muon-pair cross section and asymmetry below the Z^0 peak by using those events with relatively hard initial state radiative photon(s). The measured cross section and asymmetry show no significant deviation from the Standard Model expectations.

These results together with the DELPHI cross section and asymmetry measurements at the LEP energies from the 1990 to 1992 running periods are used to determine limits on the Z^0-Z' gauge boson mixing angle $\theta_{Z'}$ and on the Z' mass. There is no indication of the existence of a Z'; the limits obtained on the mixing angle substantially improve upon existing limits. The 95% confidence level allowed ranges of $\theta_{Z'}$ (radians) in various models are:

$$\begin{array}{lcll}
-0.0070 & \leq \theta_{Z'} \leq & 0.0078, & E_6(\chi) \text{ model,} \\
-0.0075 & \leq \theta_{Z'} \leq & 0.0095, & E_6(\psi) \text{ model,} \\
-0.029 & \leq \theta_{Z'} \leq & 0.029, & E_6(\eta) \text{ model,} \\
-0.0068 & \leq \theta_{Z'} \leq & 0.0082, & \text{L-R(1.) model,} \\
-0.0057 & \leq \theta_{Z'} \leq & 0.0077, & \text{L-R}(\sqrt{2}) \text{ model.}
\end{array}$$

ACKNOWLEDGEMENTS

At last... let me start this final act with a quotation:

> If I have seen any further than others, it is because I have been standing on the shoulders of giants. *Isaac Newton*

My particular giants have been Pete Renton, for consistently good advice and very high shoulders, and Christine Beeston for her elegant approach to muon-pair analysis.

This thesis has been made possible by the hard work of many hundreds of people over many years, pushing forwards the limits of knowledge, technology and government funding. I thank the Nuclear and Particle Physics Department and Oxford DELPHI group for providing me with the opportunity to join this privileged band of people; enabling me to contribute, in small part, to this undertaking.

I thank Paula Collins for making office life in Geneva so unpredictable; and for all those middle of the night trips to the pit. I have indeed been fortunate to have worked and played with such a diverse group of people, I thank them all for welcoming me into the Oxford DELPHI community. While it is impossible to thank everyone individually, I would like to mention Stevie 'could be worse...' Bosworth, Rashid 'yeh yeh yeh' Zuberi, Martin 'daredevil' Bates, Tim 'chocolate' Adye and Guy 'Maudit' Wilkinson for many enjoyable interactions. A special thanks to Paul 'so..' Dauncey for getting me down my first red. Also deserving of thanks are Louis Lyons for being a sympathetic editor and Bill Williams for diligent proof reading.

In addition I would like to thank Lorraine for maintaining my sanity during my stays in Geneva, by making it a home from home, and also for the broadening of perspectives she induced.

My stays in Oxford over many years has been made enjoyable by the excellent living environment of St. Hugh's College and the friendly and eclectic community fostered there. In particular I wish to thank Rachel for smoothing my return to Oxford with a wonderful summer.

I wish to thank the taxpayers of Europe for their financial support through the auspices of the Science and Engineering Research Council.

This thesis is dedicated to my family in recognition of many years of love and support.

Contents

Introduction

After several years of successful LEP operation with rising statistics, there is excellent agreement between the data and Standard Model predictions in the energy region of the Z^0. However, previous experiments at LEP have not rigorously tested Standard Model expectations away from the Z^0 pole. These predictions depend upon the precise understanding of the large effects of electromagnetic radiative corrections.

In this thesis results from studies of photons produced in $e^+e^- \to \mu^+\mu^-$ interactions at LEP energies are used to check our knowledge of electromagnetic radiative corrections and to probe cross sections and asymmetries in the unexplored energy region between LEP and TRISTAN, and indeed all the way down to PETRA energies. The analysis presented closely follows that of the paper [1], of which I am the principal author. Investigations in the unexplored energy region are encouraged by the reported $e^+e^- \to \mu^+\mu^-$ cross section measurement which is 2σ lower than the Standard Model prediction at TRISTAN ($\sqrt{s} \sim 60$ GeV[1]) [2].

This thesis is organised as follows. Chapter 1 provides an outline of the Standard Model, concentrating on precise predictions of $e^+e^- \to f\bar{f}$ cross sections and asymmetries. In Chapter 2 the motivation for several extensions to the Standard Model and how these lead to hypothetical additional Z' bosons are discussed. The proposed extensions lead to measurable deviations in the $e^+e^- \to f\bar{f}$ cross section in the energy region below the Z^0 pole. Chapter 3 includes a brief description of the LEP accelerator and DELPHI detector, concentrating on aspects of particular relevance to this study. In Chapter 4 the selection of radiative $e^+e^- \to \mu^+\mu^-$ events where the photons are detected in the electromagnetic calorimeters is described. Measurements of the angular and energy spectra of these predominantly final state

---

[1] Natural units are used throughout with $\hbar = c = 1$, both in specifying units and in formulae.

photons are presented and a comparison with the theoretical predictions is made. Chapter 5 indicates how a selection of events with mainly initial state photons, which are not detected in the electromagnetic calorimeters, is made. These events allow the underlying Born cross section and asymmetry to be measured at reduced effective centre of mass energies, below the Z^0 pole. In Chapter 6, the results obtained in Chapter 5, together with the DELPHI measurements of hadronic cross sections and leptonic cross sections and asymmetries at LEP energies, are used to obtain limits on the parameters of additional Z' gauge bosons in several models. A summary and conclusions are provided.

Chapter 1

The Standard Model

The Standard Model of particle interactions has so far passed every test; there have been no significant deviations between its predictions and experimental observations.

The Standard Model attempts to describe the characteristics and interactions of the known and postulated particles (tables 1.1 & 1.2) in a simple framework with the minimum number of input parameters. The formalism of Quantum ElectroDynamics (QED), the theory of electromagnetism, provides the prototype from which the Standard Model was developed. In particular, it is the intimate relationship between symmetry principles and the predictions of the theory that are of utmost importance in providing a basis for the construction of a theory. The Standard Model gauge group is $\mathrm{SU}(3)_c\times$ $\mathrm{SU}(2)_L\times$ U(1), unifying strong, weak and electromagnetic interactions.

This chapter provides an outline of the Standard Model and lists relevant predictions of the model; more thorough descriptions may be found in [3].

1.1 Quantum ElectroDynamics

In the electromagnetic case, the requirement that the quantum fields describing charged particles are invariant under local gauge transformations (members of the U(1) group), forces the introduction of a new 'gauge field' A_μ, which is identified with the massless photon γ. A compensating interaction term is added to the Lagrangian density and a modification of the derivative to the covariant derivative with additional terms dependent on the gauge field introduced. The manner in which the new gauge field changes under the gauge transformation is also prescribed by the

Generation			Quantum Numbers			
I	II	III	t_f	t_f^3	y_f	Q_f
$\begin{pmatrix}\nu_e\\ e\end{pmatrix}_L$	$\begin{pmatrix}\nu_\mu\\ \mu\end{pmatrix}_L$	$\begin{pmatrix}\nu_\tau\\ \tau\end{pmatrix}_L$	+1/2	+1/2 −1/2	-1	0 −1
e_R	μ_R	τ_R	0	0	-2	-1
$\begin{pmatrix}u\\ d'\end{pmatrix}_L$	$\begin{pmatrix}c\\ s'\end{pmatrix}_L$	$\begin{pmatrix}t\\ b'\end{pmatrix}_L$	+1/2	+1/2 −1/2	+1/3	+2/3 −1/3
u_R	c_R	t_R	0	0	+4/3	+2/3
d'_R	s'_R	b'_R	0	0	-2/3	-1/3

Table 1.1: Quantum numbers for the elementary fermions.

Vector Boson	t	t^3	y	q
$\begin{pmatrix}W^+\\ Z^0\\ W^-\end{pmatrix}$	+1	+1 0 −1	0	+1 0 −1
γ	0	0	0	0
Scalar Boson				
H^0	0	0	0	0

Table 1.2: Quantum numbers for gauge bosons and Higgs in the Standard Electroweak Model

invariance requirement. These changes are made in order to maintain a consistent description after the local phase transformation. The Abelian nature of the U(1) group (i.e. the phase transformations commute) means that the photon has no self-interactions. In performing QED calculations of higher order than Born (or tree) level (e.g. figure 1.1 (a)), problems are encountered with closed-loop processes (e.g. figure 1.1 (b)) as these lead to infinities in the calculated amplitudes. Finite amplitudes are regained by a technique termed renormalisation, where the infinities are 'mopped up' into re-definitions of charges and masses to their measured values. A renormalizable theory is one in which any observable can in principle be calculated to an arbitrary order of perturbation theory, in terms of a finite number of input parameters. It has been shown that all gauge theories are renormalizable [4].

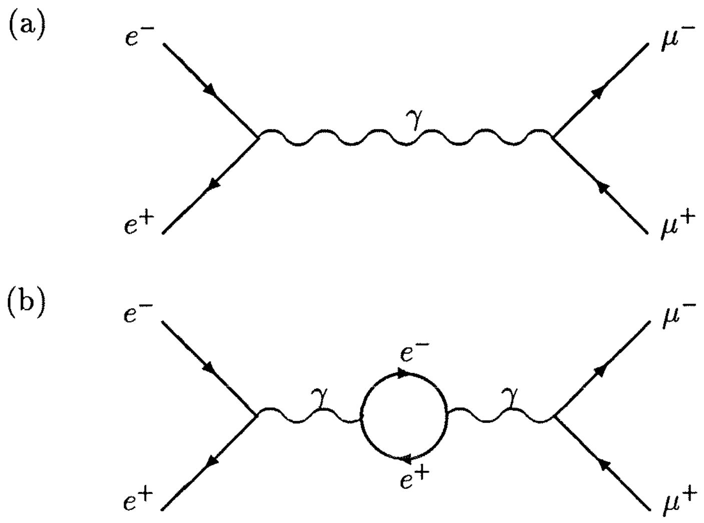

Figure 1.1: Feynman diagrams for electron positron annihilation into a $\mu^+\mu^-$ via a γ , at lowest order (a) and a higher order correction (b).

1.2 Quantum ChromoDynamics

Quantum ChromoDynamics (QCD), the theory of strong interactions between quarks, is a non-Abelian gauge theory with gauge group $SU(3)_c$, acting on the degree of freedom called 'colour' (represented by the subscript c), of which there are three types. The requirement of invariance under gauge transformations of the group $SU(3)_c$ lead to the existence of eight gauge fields corresponding to the eight generators of the group which are identified as the eight massless vector bosons called gluons.

The non-abelian nature of the $\mathrm{SU}(3)_c$ interactions results in the fundamentally different behaviour of QCD compared to QED. Analogously to the QED coupling parameter $\alpha = e^2/4\pi$, the strong interaction strength is represented by the coupling parameter α_s, which in lowest order has the form:

$$\alpha_s(Q^2) = \frac{12\pi}{(33 - 2n_f)\ln(Q^2/\Lambda^2)}; \tag{1.1}$$

where Q is the four-momentum transfer of the interaction, n_f is the number of quark flavours and Λ is a parameter specifying the QCD mass scale ($\sim$ 200 MeV). The 'running' of the coupling constant with Q^2 shows a decrease in α_s with increasing Q^2, an opposite change to that occurring in QED. This leads to *asymptotic freedom* at high Q^2 and *confinement* at low Q^2, where the coupling becomes strong. In QED the increase in the coupling at higher energies, or smaller length scales, is viewed as a result of a reduction in the bare charge screening effect of the vacuum. Analogously, an anti-screening effect is invoked in the QCD case to explain the decrease in the coupling at high energies. Vacuum fluctuations of quark loops and gluon loops (which occur as a result of gluon self-interactions) are regarded to cause a spreading of the effective colour charge, resulting in a decrease in the effective charge at smaller length scales or higher energies. The large value of α_s ($\sim$ 0.12 at 91 GeV) makes perturbative calculations in QCD significantly less precise than electroweak calculations, because higher order terms are comparatively more important.

1.3 The Standard Electroweak Model

The Standard Electroweak Model was developed by Glashow, Salam and Weinberg [5] by combining the weak and electromagnetic interactions. The gauge group of this model (often referred to simply as the Standard Model) is $\mathrm{SU}(2)_L \times \mathrm{U}(1)_y$. The path from this gauge group to physical predictions of the model is more involved than in the QED case, due to the requirement of incorporating massive vector bosons. The symmetry group results in four massless gauge fields:

- the isovector fields $W^i_\mu (i = 1, 2, 3)$ arise from local gauge invariance under $\mathrm{SU}(2)_L$ transformations (acting in weak isospin space); the subscript L indicates that the W^i_μ only couple to the left-handed fermions. These fields couple to all particles carrying weak isospin t, with a coupling constant denoted by g.

- the isoscalar field B_μ arises from local gauge invariance under $U(1)_y$ transformations acting on the weak hypercharge y, which is related to the electric charge q and the third component of weak isospin t^3 by $y = 2(q - t^3)$. This field couples to particles carrying weak hypercharge y with a coupling constant g'.

Mass terms in a Lagrangian density of the form $m_w W^\mu W_\mu$ violate both $SU(2)_L$ and $U(1)_y$ gauge invariance, thus the symmetry must be broken for massive particles to be encompassed by the model but renormalisibility must be maintained. The 'Higgs mechanism' [3] is used to give mass to the three gauge fields W^i_μ, while retaining the U(1) gauge symmetry of QED in order that its gauge field can remain massless and represent the photon. In the simplest case, referred to as the Minimal Standard Model (MSM), the spontaneous symmetry breaking is achieved with a weak isospin doublet of complex scalar fields. After application of the mechanism four gauge vector bosons are obtained; one remains massless and is identified with the photon while the other three become massive gauge vector bosons representing $W^\pm$ and Z^0. In addition the mechanism predicts one neutral scalar Higgs particle H^0, which has yet to be observed; the mass of the Higgs boson M_H is not predicted by the theory. The physical gauge fields are formed from the four fields:

$$W^\pm_\mu = \frac{1}{\sqrt{2}}\left(W^1_\mu \mp iW^2_\mu\right) \tag{1.2}$$

$$Z_\mu = \cos\theta_W W^3_\mu - \sin\theta_W B_\mu \tag{1.3}$$

$$A_\mu = \sin\theta_W W^3_\mu + \cos\theta_W B_\mu \tag{1.4}$$

where θ_W is known as the Weinberg or weak mixing angle. Although the symmetry is broken its effects are seen in the relationship of the masses and couplings of the gauge bosons. The weak mixing angle is related to the couplings, and the coupling strengths of the weak and electromagnetic interactions are related by the relationships:

$$g\sin\theta_W = g'\cos\theta_W = e \tag{1.5}$$

$$M_Z = \frac{M_W}{\cos\theta_W} \tag{1.6}$$

Comparison of low energy predictions of the Fermi point-like V-A theory of weak interactions with MSM predictions at lowest order relates the well known Fermi constant G_F to the couplings and masses:

$$\frac{G_\mathrm{F}}{\sqrt{2}} = \frac{g^2}{8\mathrm{M_W}^2} \tag{1.7}$$

Combining equations 1.5, 1.6 and 1.7 yields values for $\mathrm{M_Z}$ and $\mathrm{M_W}$ in terms of G_F, θ_W and the fine structure constant at zero Q^2, $\alpha(0)$.

$$\mathrm{M_W}^2 = \frac{\pi\alpha(0)}{\sqrt{2}\,G_\mathrm{F}\sin^2\theta_\mathrm{W}} \tag{1.8}$$

It should be noted that these masses are tree level predictions only; higher order corrections are significant and need to be considered in precision tests of the theory. The inclusion of higher orders introduces a dependence on the renormalisation scheme used. While all renormalisation schemes are in principle equivalent, giving the same result at infinite order, the results at a given order will differ between schemes. In the popular 'on-shell' scheme $\mathrm{M_W}$ and $\mathrm{M_Z}$ are used as parameters of the theory and $\sin^2\theta_\mathrm{W}$ is *defined* as:

$$\sin^2\theta_\mathrm{W} \equiv 1 - \frac{\mathrm{M_W}^2}{\mathrm{M_Z}^2}, \tag{1.9}$$

unmodified by radiative corrections. In the MSM there is a single Higgs doublet which corresponds, at the Born level, to setting the ρ parameter to unity:

$$\rho \equiv \frac{\mathrm{M_W}^2}{\mathrm{M_Z}^2\cos^2\theta_\mathrm{W}} = 1. \tag{1.10}$$

Including higher-order electroweak effects, the expression for $\mathrm{M_W}$ (equation 1.8) is modified to:

$$\mathrm{M_W}^2 = \frac{\pi\alpha(0)}{\sqrt{2}\,G_\mathrm{F}\sin^2\theta_\mathrm{W}}\cdot\frac{1}{1-\Delta r} \tag{1.11}$$

where the radiative correction Δr contains the photon vacuum polarization and the weak corrections which depend on all parameters of the model and in particular $\mathrm{M_H}$ and the top quark mass $\mathrm{M_t}$, which have no effect at tree level.

1.4 The reaction $\mathrm{e^+e^-} \to \mathrm{f\bar{f}}$

At the Born (or tree) level this interaction occurs through single photon or $\mathrm{Z^0}$ exchange in the s-channel, as shown in figure 1.2. Where the final state fermions are electrons the equivalent t-channel exchange diagrams also contribute.

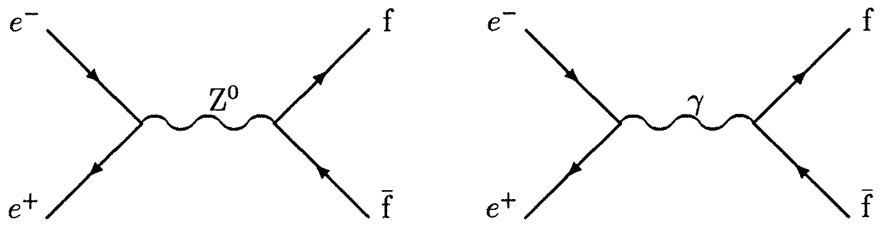

Figure 1.2: Lowest order Feynman diagrams contributing to $e^+e^- \to f\bar{f}$

The tree level Higgs exchange diagram can be neglected due to the smallness of the electron mass. The propagators for γ and Z^0 exchange can be written:

$$\begin{aligned} P_\gamma &= \frac{-ig^{\mu\nu}}{s} \\ P_Z &= \frac{i}{s - M_Z{}^2 + iM_Z\Gamma_Z}\left(-g^{\mu\nu} + \frac{q^\mu q^\nu}{M_Z{}^2}\right) \end{aligned} \tag{1.12}$$

where the term '$iM_Z\Gamma_Z$' expresses the Z^0's finite lifetime τ_Z; the width Γ_Z is related to the lifetime by $\tau_Z = \hbar/\Gamma_Z$. Feynman vertex factors for Z^0 and γ coupling to massive fermions are illustrated in figure 1.3. The couplings are expressed both in terms of the couplings to left and right handed particles c_L^f,c_R^f or in terms of axial and vector couplings a_f and v_f, where:

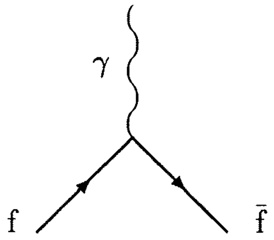

$$-ie\,Q_f\,\gamma_\mu$$

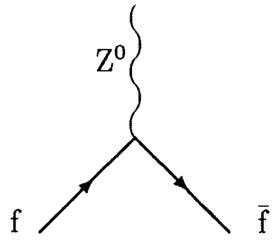

$$\frac{-ie}{\sin\theta_W\cos\theta_W}\gamma_\mu\left(c_L^f\,\frac{1-\gamma_5}{2} + c_R^f\,\frac{1+\gamma_5}{2}\right)$$

or

$$\frac{-ie}{\sin\theta_W\cos\theta_W}\gamma_\mu\tfrac{1}{2}(v_f - a_f\gamma_5)$$

Figure 1.3: The Feynman vertex factors for massive fermions to γ and Z^0 bosons

$$\begin{aligned} v_f &= t_f^3 - 2Q_f\sin^2\theta_W, \\ a_f &= t_f^3; \end{aligned} \tag{1.13}$$

t_f^3 and Q_f are the third component of the weak isospin and the charge of the fermion. Putting the vertex factors and propagators together yields the Feynman amplitude corresponding to the diagrams of figure 1.2, $\mathcal{M} = \mathcal{M}_\gamma + \mathcal{M}_{Z^0}$, where:

$$\begin{aligned} \mathcal{M}_\gamma &= ie^2 Q_f \left(\bar{f}\gamma^\alpha f\right) \frac{1}{Q^2} \left(\bar{e}\gamma_\alpha e\right) & (1.14) \\ \mathcal{M}_{Z^0} &= \frac{ig^2}{4\cos^2\theta_W} \left[\bar{f}\gamma^\alpha \left(v_f - a_f\gamma_5\right) f\right] \frac{1}{Q^2 - M_Z{}^2 + iM_Z\Gamma_Z} \left[\bar{e}\gamma_\alpha \left(v_e - a_e\gamma_5\right) e\right] \end{aligned}$$

In this expression the $\bar{e}$,e and $\bar{f}$,f within the brackets are the spinors for the initial e^+e^- pair and final $f\bar{f}$ pair respectively. The above expressions are valid only for light fermions $m_f/M_Z \ll 1$.

These invariant amplitudes yield the differential cross section for the process after summing over spin states, as a function of the centre of mass energy $\sqrt{s}$ and the polar angle θ as defined in figure 1.4:

$$\begin{aligned} \frac{d\sigma}{d\Omega} &\sim |\mathcal{M}|^2 = |\mathcal{M}_\gamma|^2 + |\mathcal{M}_{Z^0}|^2 + (\mathcal{M}_\gamma^* \mathcal{M}_{Z^0} + \mathcal{M}_\gamma \mathcal{M}_{Z^0}^*) \\ \frac{d\sigma}{d\Omega} &= \frac{\alpha^2}{4s} N_c^f \left(G_1(s).(1+\cos^2\theta) + G_3(s).2\cos\theta\right) & (1.15) \end{aligned}$$

Where N_c^f is the colour factor, 1 for leptons and $3(1+\alpha_s/\pi)$ (to first order in α_s) for the quarks, and where:

$$\begin{aligned} G_1(s) &= Q_e{}^2 Q_f{}^2 + 2Q_e Q_f v_e v_f Re[\chi_0(s)] + (v_e{}^2 + a_e{}^2)(v_f{}^2 + a_f{}^2)|\chi_0(s)|^2 \\ G_3(s) &= 2Q_e Q_f a_e a_f Re[\chi_0(s)] + 4v_e a_e v_f a_f |\chi_0(s)|^2 \\ \chi_0(s) &= \frac{1}{4\sin^2\theta_W \cos^2\theta_W} \left[\frac{s}{s - M_Z{}^2 + iM_Z\Gamma_Z}\right]. & (1.16) \end{aligned}$$

Further detail is provided in [6], in particular the article [7]. The differential cross section expression can be divided into an electromagnetic γ-exchange term independent of $\chi_0(s)$, a weak Z^0-exchange term dependent on $|\chi_0(s)|^2$ and a γ-Z^0 interference term dependent on $Re[\chi_0(s)] \sim s(s - M_Z{}^2)$.

1.4.1 Born level cross section

Integrating expression 1.15 yields the total cross section:

$$\sigma(s) = 2\pi \int_{-1}^{1} d(\cos\theta) \frac{d\sigma}{d\Omega} = \frac{4\pi\alpha^2 N_c^f}{3s} G_1(s). \qquad (1.17)$$

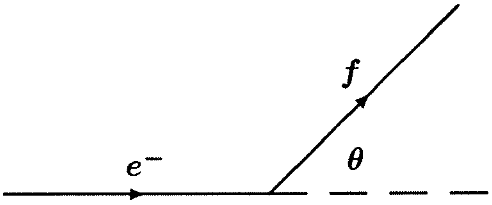

Figure 1.4: The definition of the polar angle, θ.

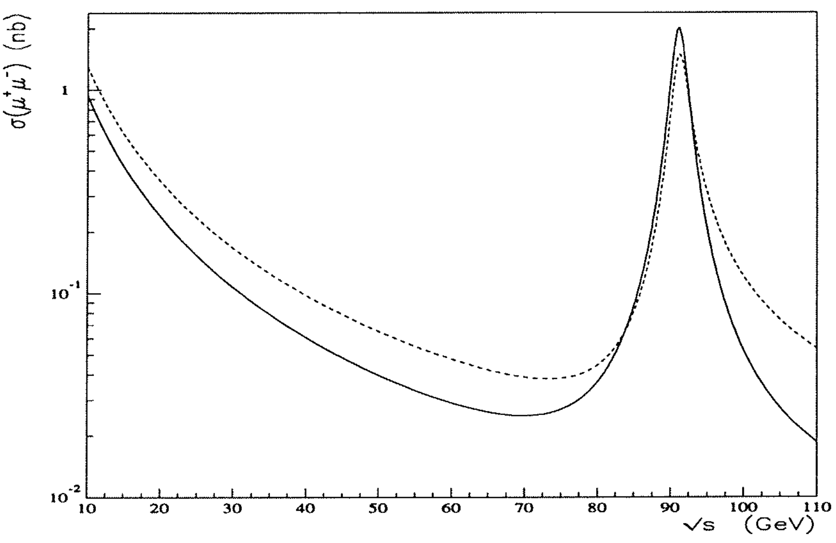

Figure 1.5: Cross section for the process $e^+e^- \rightarrow \mu^+\mu^-$ as a function of centre of mass energy for $\mathrm{M_Z} = 91.185$ GeV, $\mathrm{M_t} = 150$ GeV, $\mathrm{M_H} = 300$ GeV and $\alpha_s = 0.123$. The solid curve is the Born approximation cross section and the dashed curve is the $\mathcal{O}(\alpha)$ QED corrected curve obtained by ZFITTER.

In the energy region $\sqrt{s} \sim \mathrm{M_Z}$, Z^0-exchange is dominant, thus neglecting γ-exchange and the interference term ($\sim s(s-\mathrm{M_Z}^2)$) results in the Born-level expression:

$$\sigma(\sqrt{s} \sim \mathrm{M_Z}) = \frac{4\pi\alpha^2\mathrm{N_c^f}}{3s}\,\frac{(\mathrm{v_e}^2+\mathrm{a_e}^2)(\mathrm{v_f}^2+\mathrm{a_f}^2)}{16\sin^4\theta_\mathrm{W}\cos^4\theta_\mathrm{W}}\,\frac{s^2}{(s-\mathrm{M_Z}^2)^2+\mathrm{M_Z}^2\Gamma_\mathrm{Z}^2}. \quad (1.18)$$

The cross section can be re-expressed in terms of the 'partial widths' Γ_f and Γ_e:

$$\sigma(\sqrt{s} \sim \mathrm{M_Z}) = \frac{12\pi\Gamma_\mathrm{e}\Gamma_\mathrm{f}}{\mathrm{M_Z}^2\Gamma_\mathrm{Z}^2}\left[\frac{s\Gamma_\mathrm{Z}^2}{(s-\mathrm{M_Z}^2)^2+\mathrm{M_Z}^2\Gamma_\mathrm{Z}^2}\right], \quad (1.19)$$

where

$$\Gamma_\mathrm{f} = \frac{G_\mathrm{F}\mathrm{M_Z}^3}{6\pi\sqrt{2}}\mathrm{N_c^f}(\mathrm{a_f}^2+\mathrm{v_f}^2) = \frac{\mathrm{M_Z}}{3}\mathrm{N_c^f}\frac{\alpha(\mathrm{a_f}^2+\mathrm{v_f}^2)}{4\sin^2\theta_\mathrm{W}\cos^2\theta_\mathrm{W}}. \quad (1.20)$$

Note that the square bracket in expression 1.19 reduces to unity at $\sqrt{s} = \mathrm{M_Z}$, leaving the pole cross section σ_0^f in terms of masses and widths.

In the energy region $\sqrt{s} \ll \mathrm{M_Z}$, γ-exchange is dominant resulting in the familiar $1/s$ dependence:

$$\sigma(\sqrt{s} \ll \mathrm{M_Z}) = \frac{4\pi\alpha^2 \mathrm{N_c^f}}{3s} \mathrm{Q_e}^2 \mathrm{Q}_f{}^2 \tag{1.21}$$

The Born level and QED corrected cross sections, as discussed in section 1.5, over the energy range 10 – 110 GeV are provided in figure 1.5.

1.4.2 Born level asymmetry

The '$\cos\theta$' term in 1.15 indicates that there is an asymmetry in fermion production between the forward (polar angle θ<90°) and backward directions. This parity violation can be regarded as the signature of the weak interaction. The asymmetry is defined by:

$$\mathrm{A_{FB}} = \frac{\sigma_F - \sigma_B}{\sigma_F + \sigma_B}, \tag{1.22}$$

where σ_F & σ_B are the cross sections for production of particles in the forward & backward directions, as indicated:

$$\sigma_F = 2\pi \int_0^1 d(\cos\theta) \frac{d\sigma}{d\Omega} \qquad \sigma_B = 2\pi \int_{-1}^0 d(\cos\theta) \frac{d\sigma}{d\Omega}. \tag{1.23}$$

This gives the Born level asymmetry as:

$$\mathrm{A_{FB}^0} = \frac{3}{4} \frac{\mathrm{G_3}(s)}{\mathrm{G_1}(s)} \tag{1.24}$$

Assuming $\mathrm{v_f} \ll \mathrm{a_f}$, which is a good approximation for leptons, and $\sqrt{\mathrm{s}} \sim \mathrm{M_Z}$ yields the expression:

$$\mathrm{A_{FB}^0}(\sqrt{s} \sim \mathrm{M_Z}) = \frac{3}{4} \left[1 + \frac{2\sin^2\theta_\mathrm{W} \cos^2\theta_\mathrm{W}}{\mathrm{v_e v_f}} \left(1 - \frac{\mathrm{M_Z}^2}{\mathrm{s}} \right) \right] \mathcal{A}_\mathrm{e} \mathcal{A}_\mathrm{f} \tag{1.25}$$

where,

$$\mathcal{A}_\mathrm{f} = \frac{2\mathrm{v_f a_f}}{\mathrm{v_f}^2 + \mathrm{a_f}^2} \tag{1.26}$$

The square bracket of expression 1.25 reduces to unity at the $\mathrm{Z^0}$ pole, $\sqrt{s} = \mathrm{M_Z}$. The Born level and QED corrected asymmetries over the energy range 10 – 110 GeV are provided in figure 1.6.

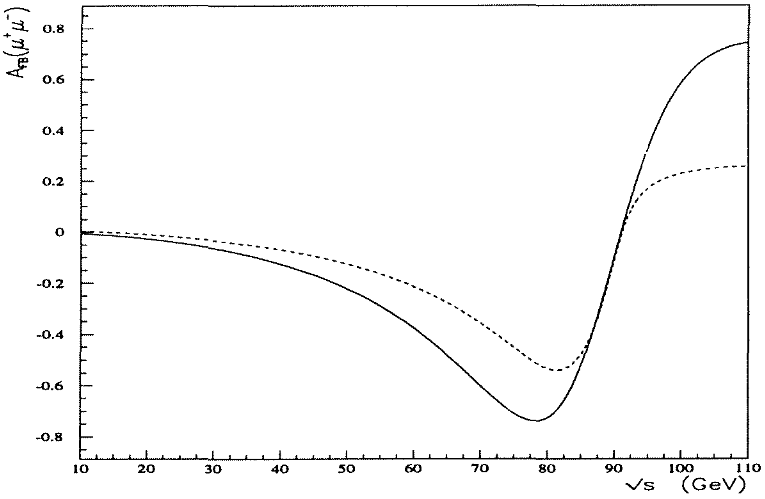

Figure 1.6: Forward-Backward asymmetry A_{FB} for the process $e^+e^- \to \mu^+\mu^-$ as a function of centre of mass energy. The solid curve is the Born approximation asymmetry and the dashed curve is the $\mathcal{O}(\alpha)$ QED corrected curve obtained from ZFITTER.

1.5 Radiative corrections

Radiative corrections to the interaction $e^+e^- \to f\bar{f}$ distort the Born-level cross sections and asymmetries at energies close to the Z^0 pole, so that the observables are substantially different from their Born-level formulae. The corrections can be conveniently separated into three classes, as illustrated in figure 1.7, which are discussed below. In this section, outlines of the characteristics and significance of the corrections are provided, a fuller discussion can be found in the volume [6]; in particular the articles [7], [8] and [9].

1.5.1 Photonic or QED Corrections

These corrections correspond to all diagrams with real or virtual photons added to the Born level diagrams; they are large and depend on experimental cuts. The dominant contribution arises from initial state radiation where a photon is radiated from the initial state, thus modifying the effective centre of mass energy. Simple kinematics shows that after radiating a photon of energy E_γ the effective centre of mass energy is reduced from $\sqrt{s}(= 2E_b$, where E_b is the beam energy) to $\sqrt{s'}$, where

$$s' = s - 2E_\gamma\sqrt{s} = s\left(1 - \frac{E_\gamma}{E_b}\right) \tag{1.27}$$

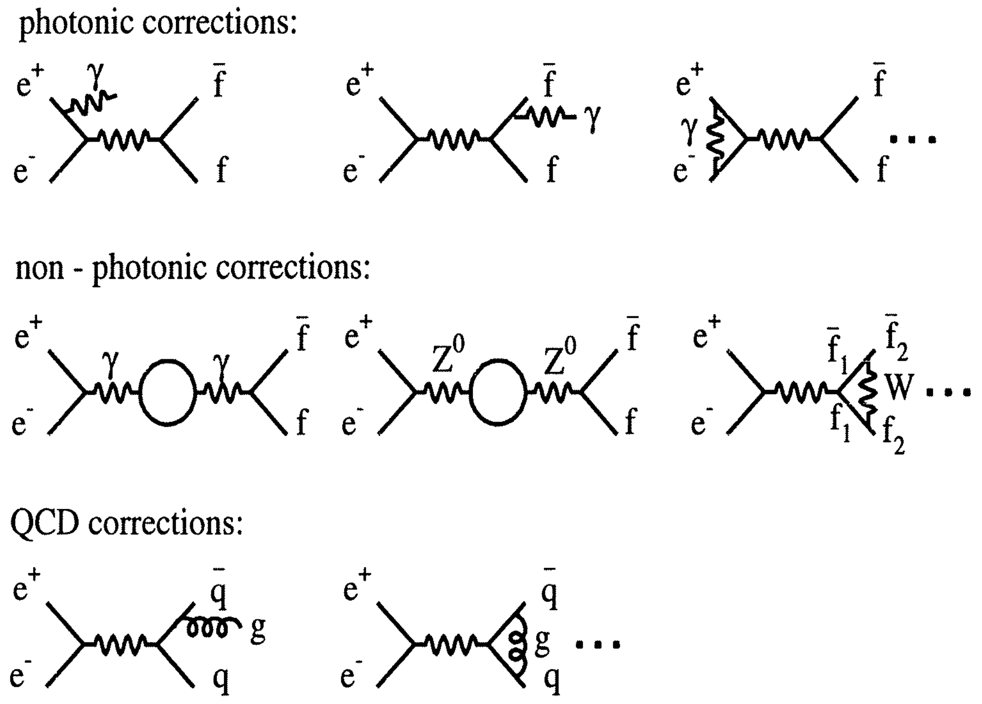

Figure 1.7: Radiative corrections to the process $e^+e^- \rightarrow f\bar{f}$.

Due to the strong energy dependence of the underlying Born cross section across the resonance, this results in a ~ 30% reduction of the Born level peak cross section and an alteration in the shape of the resonance, shifting it upwards in energy and causing a radiative tail for $\sqrt{s} > \mathrm{M_Z}$, as illustrated in figure 1.8. These purely QED effects need to be understood very precisely in order that the underlying electroweak physics can be studied. They are taken into account by convoluting the cross section including weak corrections σ^f_W by a radiator function $\mathcal{H}$, as indicated:

$$\sigma^f_{obs}(s) = \int_0^s \left[\sigma^f_W(s') \cdot \mathcal{H}(s,s') + \Delta_{\rm int}\right] ds' \,, \tag{1.28}$$

where $\Delta_{\rm int}$ accounts for the small initial-final state interference contribution to the cross section. A further photonic correction is required to account for the effects of final state radiation, this introduces an additional factor of $(1+\delta_{\rm QED})$ into the width expression 1.20 for the final state,

$$\delta_{\rm QED} = \frac{3\alpha}{4\pi} \mathrm{Q}_f{}^2 \sim 0.17\% \, \text{(for leptons)}. \tag{1.29}$$

The above correction is for the case of no cuts applied to the final state fermions; when cuts are applied larger corrections can result.

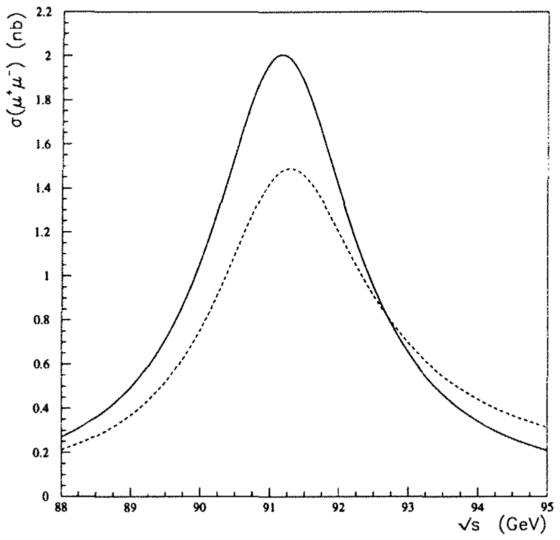

Figure 1.8: Muon pair cross section as a function of centre of mass energy for $M_Z = 91.185$ GeV, $M_t = 150$ GeV, $M_H = 300$ GeV and $\alpha_s = 0.123$. The solid curve is the Born approximation cross section and the dashed curve is the $\mathcal{O}(\alpha)$ QED corrected curve obtained by ZFITTER.

1.5.2 QCD Corrections

These corrections account for gluon radiation from quarks, modifying the $q\bar{q}$ final state and also $q\bar{q}$ internal loops, thus affecting the partial width $\Gamma_{q\bar{q}}$:

$$\Gamma_{q\bar{q}} \rightarrow \Gamma_{q\bar{q}}(1+\delta_{\mathrm{QCD}}), \tag{1.30}$$

where δ_{QCD} is an expansion of the strong coupling parameter [10]:

$$\delta_{\mathrm{QCD}} = \frac{\alpha_s(\mathrm{M_Z}^2)}{\pi} + 1.409\left(\frac{\alpha_s(\mathrm{M_Z}^2)}{\pi}\right)^2 - \cdots. \tag{1.31}$$

The strong coupling parameter at $Q^2 = \mathrm{M_Z}^2$, as described in section 1.2, is used in the expansion.

1.5.3 Electroweak corrections

These corrections are small but crucial as they depend upon the unknown or poorly known parameters of the MSM: the masses of the top quark [11] and the Higgs boson. It is through the effects of the electroweak corrections that precision tests of the MSM can be made. The corrections can be divided into three classes: propagator, vertex and box corrections corresponding to virtual diagrams with modifications to the vector boson propagators and vertices and also box diagrams with the exchange of two vector bosons. All these corrections are independent of the experimental cuts and indeed the propagator corrections are independent of the flavour of the final state fermions. A familiar example of a propagator correction is that for the photon propagator (also known as the vacuum-polarization of the photon), this is accommodated by allowing an energy dependent running electromagnetic coupling constant[1].

$$\alpha = \frac{1}{137.04} \Rightarrow \alpha(\mathrm{s} = \mathrm{M_Z}^2) = \frac{1}{128.87 \pm 0.12} \tag{1.32}$$

The box corrections are non-resonant and thus small near the Z^0 pole, allowing the violation of the factorization property between initial and final states, that is implicit in the developed formalism, to be neglected.

1.6 Improved Born Approximation

The Improved Born Approximation (IBA) [8] provides a way of accounting for many of the higher order effects in the calculation of cross sections and asymmetries, achieving a very good approximation to the full calculation, and yet retaining the simple Born level structure. Firstly the most significant weak corrections are absorbed into re-definitions of the parameters, replacing the coupling constants by energy dependent effective couplings and replacing Γ_Z in the Breit-Wigner denominator, as summarized [13]:

$$\sin^2\theta_W \Rightarrow \quad \sin^2\theta_W{}^{\mathrm{eff}} = 1 - \frac{\mathrm{M_W}^2}{\rho_f \mathrm{M_Z}^2} \tag{1.33}$$

$$\mathrm{v_f} \Rightarrow \quad \bar{\mathrm{v}}_\mathrm{f}(\mathrm{s}) = \sqrt{\rho_f}\left[\mathrm{t_f^3} - 2\mathrm{Q}_f \sin^2\theta_W{}^{\mathrm{eff}}\right] \tag{1.34}$$

$$\mathrm{a_f} \Rightarrow \quad \bar{\mathrm{a}}_\mathrm{f}(\mathrm{s}) = \sqrt{\rho_f}\,\mathrm{t_f^3} \tag{1.35}$$

$$\alpha \Rightarrow \quad \alpha(\mathrm{s}) = \frac{\alpha}{1 - \Delta\alpha(\mathrm{s})} \tag{1.36}$$

$$\Gamma_Z \Rightarrow \quad \Gamma_Z(\mathrm{s}) = \frac{\mathrm{s}}{\mathrm{M_Z}^2} \cdot \Gamma_Z(\mathrm{s} = \mathrm{M_Z}^2) \tag{1.37}$$

$$\tag{1.38}$$

The remaining weak corrections arising from box corrections and from the imaginary part of the Z^0 propagator together with terms due to γ-exchange and γ-Z^0 interference terms are accounted for in additional flavour dependent residual terms. The

---

[1] $1/\alpha(Q^2 = \mathrm{m_e}^2) = 137.0359895(61)$ from [12]

s-dependence of the effective couplings is negligible in the vicinity of the Z^0 pole. The effective rho parameter ρ_f which measures the relative strength of the neutral and charged currents is introduced in these re-definitions; it is unity at lowest order. These re-definitions lead to the width and cross section expressions (cf. 1.20,1.19):

$$\Gamma_f^{IBA} = \frac{G_F M_Z^3}{6\pi\sqrt{2}}(\bar{a}_f^2+\bar{v}_f^2)\left(1+\frac{3\alpha}{4\pi}Q_f^2\right)N_c^f(1+\delta_{QCD}) \tag{1.39}$$

$$\sigma^{IBA}(\sqrt{s}\sim M_Z) = \frac{1}{\left(1+\frac{3\alpha}{4\pi}Q_f^2\right)}\frac{12\pi\Gamma_e\Gamma_f}{M_Z^2\Gamma_Z^2}\frac{s\Gamma_Z^2}{(s-M_Z^2)^2+\frac{s^2\Gamma_Z^2}{M_Z^2}}. \tag{1.40}$$

The final state QED correction factor, discussed in section 1.5.1, appears in the denominator in the cross section expression when the partial width expressions 1.39 are used ensuring that this **final** correction is applied only once. As discussed in section 1.5.1, the dominant corrections due to initial state radiation are included by convoluting these IBA expressions with the radiator function. Note that the replacement of v_f and a_f by $\bar{v}_f$ and $\bar{a}_f$ scales the width expression by the rho parameter ρ_f. In the Minimal Standard Model this is given by:

$$\rho_f = 1+\frac{3G_F M_t^2}{8\pi^2\sqrt{2}} - \frac{11G_F M_Z^2\sin^2\theta_W}{12\pi^2\sqrt{2}}\left[\ln\left(\frac{M_H}{M_W}\right)-\frac{5}{12}\right]+\cdots, \tag{1.41}$$

indicating an approximately quadratic increase in the partial width with increasing M_t and an approximately logarithmic decrease with M_H. The dependences for the b quark case are rather different due to large vertex correction terms, from loop diagrams involving b,t and W particles. These additional corrections are large in this case, as the b and t quarks are in the same generation, leading to unsuppressed transitions. They conspire to remove substantially the M_t dependence from the partial width.

The IBA expression for the forward-backward asymmetry at $s = M_Z^2$ is (cf. 1.25):

$$A_{FB}^{0\ IBA}(\sqrt{s}\sim M_Z) = \frac{3}{4}\bar{\mathcal{A}}_e\bar{\mathcal{A}}_f + \Delta_f^{res} \tag{1.42}$$

where,

$$\bar{\mathcal{A}}_f = \frac{2\bar{v}_f\bar{a}_f}{\bar{v}_f^2+\bar{a}_f^2}. \tag{1.43}$$

The term Δ_f^{res} is the residual contribution to the asymmetry from photon exchange, the imaginary part of of the Z^0 propagator and weak box diagrams.

1.7 ZFITTER

ZFITTER is a package for the calculation of fermion pair cross sections and asymmetries with several branches of calculation techniques available, including MSM calculations as well as almost model independent approaches using effective couplings. A detailed description outlining these various branches can be found in [14], along with descriptions of the three calculation chains available, each with different treatments of the QED corrections that allowing the observables to be calculated with various cuts applied.

The MSM calculation forms the central branch of the program, calculating the observables as functions of $\mathrm{M_Z}$,$\mathrm{M_t}$,$\mathrm{M_H}$ and α_s; the calculation includes complete $\mathcal{O}(\alpha)$ weak loop corrections with a re-summation of leading higher-order terms. The higher-order terms accounted for include leading $\mathcal{O}(\alpha^2\mathrm{M_t}^2)$, complete $\mathcal{O}(\alpha\alpha_s)$ and leading $\mathcal{O}(\alpha\alpha_s\mathrm{M_t}^2)$ terms.

Chapter 2

Extensions to the Standard Model

Despite the excellent performance of the Standard Model so far, it is manifestly not the 'final' theory. Problems with the Standard Model include the large number of free parameters ($\sim$ 18) and the rather artificial way that the Higgs potential and electroweak symmetry breaking are introduced, predicting the as yet unseen Higgs boson. Also the theory does not explain the existence of three families of quarks and leptons nor does it encompass the origins of CP violation[1] or the quantization of electric charge. In addition the theory provides no reason for the particles to form left-handed doublets and right-handed singlets and does not predict particle masses. A further problem is that gravity is not included in the model.

This chapter provides a brief introduction and motivation to the various extensions to the Standard Model that suggest the existence of additional neutral heavy gauge bosons Z', of mass $\mathrm{M}_{\mathrm{Z}'}$ larger than M_{Z}. The manner in which Z' emerges in these theories is traced and the phenomenology of additional gauge bosons reviewed.

2.1 Grand Unified Theories

Many candidate extensions to the Standard Model have been suggested to address its deficiencies, the grand unified theories [15] in particular attempt to reduce the number of parameters of the model by relating the at present independent coupling constants. These theories are based upon the assertion that the electromagnetic, weak and strong interactions are different manifestations of a single interaction with

---

[1] Although it does provide the formalism to describe CP violation in the phase of the CKM matrix.

an associated gauge group G that contains the SU(3)$_c$ and SU(2)$_L\times$ U(1)$_y$ gauge groups as subgroups. In the grand unified schemes the various interactions originate from a symmetry breaking pattern of the gauge group G into the Standard Model gauge group, with the apparent strength differences of the interactions at low energies (small compared to the masses of the mediators of the interaction) being regarded as consequences of a spontaneous symmetry breakdown. Candidates for the grand unifying group which is the starting point of the symmetry breaking scheme include SU(5), SO(10) and E$_6$. The successful partial unification of the electromagnetic and weak interactions in the GSW theory has motivated the attempts to achieve further unification, however no generally accepted grand unified theory yet exists.

The vastly different energies of the unification scale ($\sim 10^{15}$ GeV) and the electroweak scale ($\sim$ 100 GeV) cause what is known as the *hierarchy problem.* It turns out that to prevent divergences on performing loop corrections to the masses of Higgs scalars in the theory a fine tuning of parameters is required (to 24 places of decimals). Avoidance of point-like couplings to fundamental scalars in composite models (like technicolour) or cancellation of divergences by additional particles in supersymmetric models circumvent the hierarchy problem.

2.2 Supersymmetry

In general, grand unified theories do not include a natural relationship between bosons and fermions. This possibility is explored in *supersymmetric* [16] models which incorporate a proposed new symmetry of nature called supersymmetry, whereby every known elementary particle has a supersymmetric partner "s-particle" which is like it in all respects other than spin. The spin 1/2 fermions have spin 0 superpartners and spin 1 bosons have spin 1/2 superpartners. Also the spin 0 Higgs scalar has a spin 1/2 superpartner called the Higgsino. None of these sparticles have been observed, indicating that the symmetry is broken. Supersymmetry is attractive as it deals with the problem of quadratic Higgs mass divergence, due to cancellation of the divergent loops of the particles by those of the sparticles[2], and brings spin into the gauge theory structure. Also some progress has been made in linking the

---

[2] For the cancellation to occur it is necessary for the sparticle mass to be less than $\sim$ 1 TeV.

theory to gravity in that applying the supersymmetry generators twice to any boson or fermion field results in a space-time transformation.

2.3 Compositeness

One of the most drastic ways of addressing the problems of the Standard Model is to follow the historical route of viewing some, or all, "elementary" particles to be composite (see [17], in particular [18]). The hope of these models is to explain the proliferation of quarks and leptons in terms of a simple underlying substructure of particles called "preons". Such compositeness models predict a spectrum of new particles including new and excited vector bosons, quarks and leptons. No satisfactory model which reproduces the lepton and quark spectrum has yet been constructed.

More success has been achieved in developing models where the compositeness is limited to the intermediate vector bosons. Models with predictions close to those of the Standard Model in the energy regions currently accessible and yet deviating at higher energies have been devised [19].

2.4 Superstrings

Superstring theories are interesting as they seem to provide a consistent description of quantum gravity while incorporating previous unification attempts together with supersymmetry. They are the first attempts at a "theory of everything", offering the hope of a theory free from adjustable parameters [20, 21].

The theories become relevant at the Planck scale, the energy ($\sim 10^{19}$ GeV) and distance ($\sim 10^{-33}$ cm) at which quantum gravitational effects become important. In these theories fundamental objects are no longer regarded as point like particles but extended one-dimensional "strings" and the observed particles correspond to the lowest energy "vibration modes" of the string. Some success has been achieved in developing an anomaly free theory using the gauge groups SO(32) and $E_8 \times E_8$. The enormous gulf between presently accessible energies and the Planck energy together with the infancy of superstring phenomenology make experimental checks of the theories problematic.

2.5 Emergence of Z' in various models

A common feature of extensions to the Standard Model is the existence of large groups in the theory. Breaking schemes must be devised to reproduce (or almost reproduce) the Standard Model gauge group to be consistent with the low energy observations. Many of the schemes include an additional gauge group factor surviving along with the Standard Model gauge group, down to energies close to the electroweak scale. These extra factors generally lead to predictions of additional neutral heavy gauge bosons Z', of mass $\mathrm{M_{Z'}}$ larger than $\mathrm{M_Z}$. In addition exotic heavy fermions are often predicted as well. The resulting deviations from Standard Model predictions must be small in order to be consistent with current observations. This requirement can be converted into limits on the parameters of the models.

The couplings of the additional gauge bosons Z' to fermions $\mathrm{a_f'}$ and $\mathrm{v_f'}$ and coupling constant g' depend on the particular model and breaking scheme.

2.5.1 $\mathrm{E_6}$ models

There is particular interest in the breakdown of the $\mathrm{E_6}$ group as it appears in grand unified theories and can be the low-energy limit of the $\mathrm{E_8 \times E_8}$ group occurring in superstring theories.

The symmetry breaking scheme of the $\mathrm{E_6}$ group is assumed to be [22]:

$$\begin{aligned} E_6 &\longrightarrow SO(10) \times U(1)_\psi \longrightarrow SU(5) \times U(1)_\chi \times U(1)_\psi \longrightarrow \\ &\longrightarrow SU(3)_c \times SU(2)_L \times U(1)_Y \times U(1)_\chi \times U(1)_\psi; \end{aligned} \tag{2.1}$$

resulting in the extra factors $\mathrm{U(1)_\chi}$ and $\mathrm{U(1)_\psi}$ which correspond to two extra gauge bosons $\mathrm{Z'_\chi}$ and $\mathrm{Z'_\psi}$. In general it is assumed that only one of them, Z', is light enough to be detected:

$$\mathrm{Z}' = \mathrm{Z}'_\chi \cos\Theta_6 + \mathrm{Z}'_\psi \sin\Theta_6, \tag{2.2}$$

where the parameter values $\Theta_6 = 0, \pi/2$ or $\tan^{-1}\sqrt{5/3}$ define the $\mathrm{E_6}(\chi)$, $\mathrm{E_6}(\psi)$ or $\mathrm{E_6}(\eta)$ models respectively. In these $\mathrm{E_6}$ models the couplings $\mathrm{a_f'}$ and $\mathrm{v_f'}$ are obtained as linear combinations of the $\mathrm{U(1)_\chi}$ and $\mathrm{U(1)_\psi}$ charges, the charges being obtained from the group properties.

2.5.2 Left-Right symmetric models

In the left-right symmetric model [23] the gauge group is $SU(2)_L \times SU(2)_R \times U(1)_{B-L}$, where B and L are the baryon and lepton numbers. This model is the simplest extension to the Standard Model that includes extra charged gauge bosons, the $SU(2)_R$ factor leading to $W^{\pm}_R$ and Z_R in addition to the standard $W^{\pm}_L$ and Z_L from $SU(2)_L$. The model predicts heavy right handed neutrinos and provides an explanation of the low mass of the observed neutrinos, by means of the see-saw mechanism [24].

The parameter α_{LR} describes the couplings of the heavy bosons to fermions; it is expressed in terms of the $SU(2)_{L,R}$ coupling constants $g_{L,R}$ and the weak mixing angle:

$$\alpha_{LR} = \sqrt{\frac{\cos^2\theta_W - \sin^2\theta_W}{\sin^2\theta_W} \cdot \frac{g_L}{g_R}}. \tag{2.3}$$

For α_{LR} at its lower bound of $\sqrt{2/3}$, the L-R model is identical to the $E_6(\chi)$ model. The upper bound corresponds to $g_L = g_R$, with value $\alpha_{LR} \sim 1.53$ for $\sin^2\theta_W = 0.23$.

2.5.3 Y and Y_L models

The Y and Y_L isoscalar weak vector bosons appear in preon models with a composite structure of the weak interactions. In the Y model the coupling is to the weak hypercharge current; the model corresponds to a preon Lagrangian of global $SU(2)_{WI} \times U(1)_Y$ symmetry, the subscripts WI and Y referring to weak isospin and weak hypercharge respectively. In the Y_L model the compositeness scale of the right-handed sector is envisaged to be larger than that of the left-handed sector, or alternatively right-handed quarks and leptons are regarded as elementary, leading to a coupling to the left-handed component of the weak hypercharge current only. The low energy limit of these models is the standard electroweak theory without the Higgs sector; the masses of leptons, quarks and weak bosons are generated as a consequence of the gauge force binding the preon subconstituents of the observed particles.

A full description of these models including how the low energy Standard Model predictions are closely reproduced is provided in [19].

2.6 Gauge Boson Mixing

In this section the phenomenology of additional gauge bosons in E_6 and Left-Right symmetric models is traced, the approach taken is as mentioned in [14] and extended in [25]. The calculation technique described is that employed by the computer packages ZFITTER and ZEFIT when used in combination.

An additional gauge boson Z' does not result in any special final state signature below production threshold, but rather can be detected (or not detected) by virtue of the three effects:

- shift in the Z^0 mass due to Z^0-Z' mixing,
- modification of Z^0 couplings due to Z^0-Z' mixing,
- virtual Z' exchange.

These lead to small modifications in the neutral current cross sections and asymmetries, thus a very precise prediction of radiative corrections is essential in searching for Z'. The third item can be neglected for large enough Z' masses, leaving the contributions due to Z^0-Z' mixing.

The neutral current Lagrangian gains an extra term due for the Z':

$$\mathcal{L} = eA_\mu J^\mu_\gamma + gZ_\mu J^\mu_Z + g' Z'_\mu J^\mu_{Z'}, \tag{2.4}$$

where the currents are of the form:

$$J^\mu_n = \sum_f \bar{f}\gamma^\mu \left[\mathrm{v_f}(n) + \gamma_5 \mathrm{a_f}(n)\right] f, \quad n = \gamma, \mathrm{Z^0}, \mathrm{Z'}. \tag{2.5}$$

The coupling constants in the Lagrangian are defined for the symmetry eigenstates, i.e. $g = (\sqrt{2}G_\mu \mathrm{M_Z}^2)^{1/2}$, whereas the renormalisation is performed for the mass eigenstates $\mathrm{M_1}$,$\mathrm{M_2}$. A matrix with mixing angle θ_M relates the mass eigenstates to the symmetry eigenstates as follows:

$$\begin{pmatrix} \mathrm{Z_1} \\ \mathrm{Z_2} \end{pmatrix} = \begin{pmatrix} \cos\theta_\mathrm{M} & \sin\theta_\mathrm{M} \\ -\sin\theta_\mathrm{M} & \cos\theta_\mathrm{M} \end{pmatrix} \begin{pmatrix} \mathrm{Z^0} \\ \mathrm{Z'} \end{pmatrix}. \tag{2.6}$$

Diagonalisation of the mass matrix and equation 2.6 lead to the relationship [26]:

$$\mathrm{t_M}^2 \equiv \tan^2\theta_\mathrm{M} = \frac{\mathrm{M_Z}^2 - \mathrm{M_1}^2}{\mathrm{M_2}^2 - \mathrm{M_Z}^2}, \tag{2.7}$$

showing the shift in M_Z from its SM value. Without mixing $M_Z = M_1$ and $M_{Z'} = M_2$. The couplings of the mass eigenstates Z_1 and Z_2 to fermions in terms of the couplings to the symmetry eigenstates are:

$$\begin{aligned} v_f(1) &= \cos\theta_M v_f + \frac{g'}{g}\sin\theta_M v_f', & a_f(1) &= \cos\theta_M a_f + \frac{g'}{g}\sin\theta_M a_f', \\ v_f(2) &= \cos\theta_M v_f' - \frac{g}{g'}\sin\theta_M v_f, & a_f(2) &= \cos\theta_M a_f' - \frac{g}{g'}\sin\theta_M a_f, \end{aligned} \tag{2.8}$$

where v_f,a_f are as defined in equation 1.13 and v_f',a_f' are the equivalent couplings for Z'. The coupling for the mass eigenstate Z_1 can be restated as:

$$\begin{aligned} a_f(1) = &\quad \left(\cos\theta_M + \sin\theta_M \frac{g'a_f'}{ga_f}\right) a_f = (1 - y_f)\, a_f, \\ \text{where :} \quad y_f = &\quad -\sin\theta_M \frac{g'a_f'}{ga_f} + (1 - \cos\theta_M) \sim -\sin\theta_M \frac{g'a_f'}{ga_f}, \end{aligned} \tag{2.9}$$

expressing the coupling $a_f(1)$ in terms of a small correction y_f to the old coupling a_f. For the special case $Q_f = -|Q_f|$, $t_f^3 = -1/2$, the IBA expressions of section 1.6 for the axial and vector couplings become:

$$\begin{aligned} \frac{\bar{v}_f}{\bar{a}_f} &= 1 - 4|Q_f|\sin^2\theta_W{}^{\text{eff}} = 1 - 4|Q_f|\sin^2\theta_W\kappa_f, \\ \bar{a}_f &= \sqrt{\rho_f}\, t_f^3, \end{aligned} \tag{2.10}$$

where κ_f and ρ_f are weak form factors expressing the weak loop corrections. The equivalent expression for the mixed couplings, equations 2.8, is:

$$\frac{v_f(1)}{a_f(1)} = \frac{v_f + \tan\theta_M v_f' g'/g}{a_f + \tan\theta_M a_f' g'/g} \equiv 1 - 4|Q_f|\sin^2\theta_W(1 - x_f), \tag{2.11}$$

which is used together with the unmixed: $v_f/a_f = 1 - 4|Q_f|\sin^2\theta_W{}^{\text{eff}}$, to define the small correction x_f in terms of couplings and θ_M. The 'IBA vertex factor' for the decay of the Z^0 boson to fermions (cf. figure 1.3) is:

$$\begin{aligned} \bar{\mathcal{V}} &\sim \left(\frac{G_\mu M_Z{}^2}{\sqrt{2}}\right)^{\frac{1}{2}} \gamma_\mu \left[\bar{v}_f - \bar{a}_f\gamma_5\right] \\ &\sim \left(\frac{G_\mu M_Z{}^2}{\sqrt{2}}\right)^{\frac{1}{2}} \gamma_\mu\sqrt{\rho_f}a_f \left[1 - 4|Q_f|\sin^2\theta_W\kappa_f - \gamma_5\right]. \end{aligned} \tag{2.12}$$

Similarly the mixed expression, using equation 2.11, for the Z_1 vertex factor is:

$$\begin{aligned} \bar{\mathcal{V}}' &\sim \left(\frac{G_\mu M_1{}^2}{\sqrt{2}}\right)^{\frac{1}{2}} \gamma_\mu \left[\bar{v}_f(1) - \bar{a}_f(1)\gamma_5\right] \\ &\sim \left(\frac{G_\mu M_1{}^2}{\sqrt{2}}\right)^{\frac{1}{2}} \gamma_\mu\sqrt{\rho_f}a_f(1 - y_f) \left[1 - 4|Q_f|\sin^2\theta_W\kappa_f(1 - x_f) - \gamma_5\right]. \end{aligned} \tag{2.13}$$

The above expressions show the replacements necessary to include the mixing effects in the form factors:

$$\begin{aligned} \kappa_f \Rightarrow \ \kappa_f^M &= (1 - x_f)\kappa_f, \\ \rho_f \Rightarrow \ \rho_f^M &= \rho_{mix}(1 - y_f)^2 \rho_f, \end{aligned} \tag{2.14}$$

where by using equation 2.7:

$$\rho_{mix} = \frac{M_Z{}^2}{M_1{}^2} = \frac{1 + \tan^2\theta_M (M_2{}^2/M_1{}^2)}{1 + \tan^2\theta_M} = 1 + \sin^2\theta_M \left(\frac{M_2{}^2}{M_1{}^2} - 1 \right). \tag{2.15}$$

Setting $\rho_{mix} = 1$ corresponds to restricting the Higgs sector to doublets; in the general case it is left as a free parameter. A more detailed discussion of the weak form factors can be found in [14]. The effective couplings accounting for the mixing become:

$$\begin{aligned} \bar{v}_f(1) &= \bar{a}_f(1) \left[1 - 4|Q_f| \sin^2\theta_W \kappa_f^M \right], \\ \bar{a}_f(1) &= \sqrt{\rho_f^M}\, t_f^3. \end{aligned} \tag{2.16}$$

Following the technique in section 1.4 combining vertex factors and the propagator for Z_1: $P_1 \sim 1/(s - M_1{}^2 + is(\Gamma_1/M_1))$ yields the matrix element $\bar{\mathcal{M}}_1$. An analogous approach to the above leads to the matrix element $\bar{\mathcal{M}}_2$ for exchange of Z_2. Combining these with the matrix element for photon exchange $\bar{\mathcal{M}}_\gamma$ results in the matrix element $\bar{\mathcal{M}}$:

$$\bar{\mathcal{M}} = \bar{\mathcal{M}}_\gamma + \bar{\mathcal{M}}_1 + \bar{\mathcal{M}}_2, \tag{2.17}$$

which is used to calculate the improved Born cross section with the effects of an additional gauge boson included. This is then convoluted to account for the dominant initial state radiation effects in the same manner as in the MSM calculation.

A different approach is taken in the Y and Y_L models with mixing parameter λ^2_{Y,Y_L} instead of $\theta_{Z'}$; a full discussion is provided in [19].

2.7 Predicted deviations from SM

Figure 2.1 shows the deviations in the Born level muon-pair asymmetries, predicted by several Z′ models. The fractional deviations in the hadronic & muon-pair Born level cross sections are shown in figure 2.2. The Z′ masses used are close to

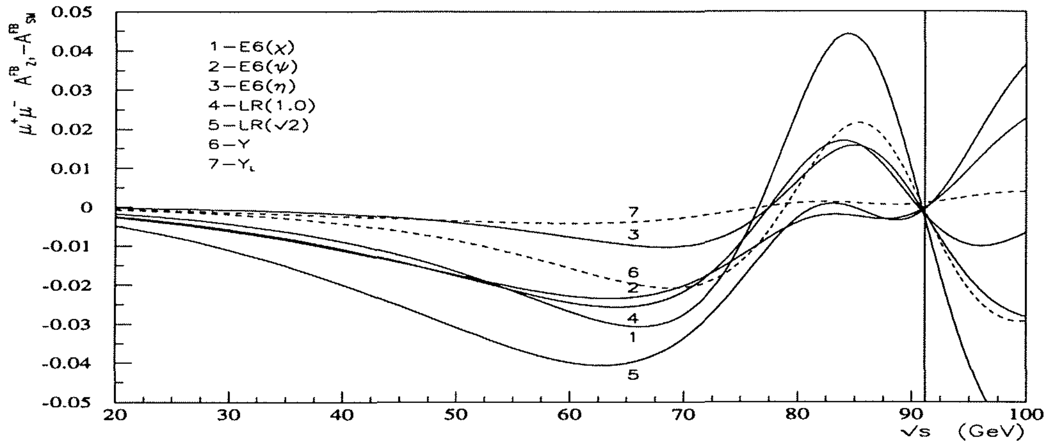

Figure 2.1: Deviations of the $e^+e^- \rightarrow \mu^+\mu^-$ asymmetry from Standard Model expectations in various models: $A_{FB}(Z') - A_{FB}(SM)$. For the E_6 and L-R models $M_{Z'}$ = 150 GeV, $\theta_{Z'}$ = 0.01 radians and for the Y and Y_L models $M_{Z'}$ = 800 GeV, λ^2_{Y,Y_L}=0.1.

the 95% C.L. lower limit values, obtained in chapter 6, with mixing parameter $\theta_{Z'}$ or λ^2_{Y,Y_L} in the middle of the 95% C.L. allowed range for the mass used.

In the energy range near the Z^0 pole position, the additional bosons' direct contributions to the cross sections are small. The deviations from SM expectations arise primarily from interference effects of the hypothesized bosons and the existing ones (γ and Z^0). The pole region behaviour is influenced by the Z'-Z^0 interference amplitude, which changes sign at the pole, resulting in an enhancement of the cross section compared to the SM value around $\sqrt{s} = M_Z - \Gamma_Z/2$ and some reduction at energies larger than the pole energy. In the region currently accessible by direct or indirect means, the largest deviations occur in the $E_6(\chi)$ and Y models; with predicted muon-pair cross section values 8% lower than the SM predictions in the region $\sqrt{s} \sim 70$ GeV, arising due to the $\gamma - Z'$ interference.

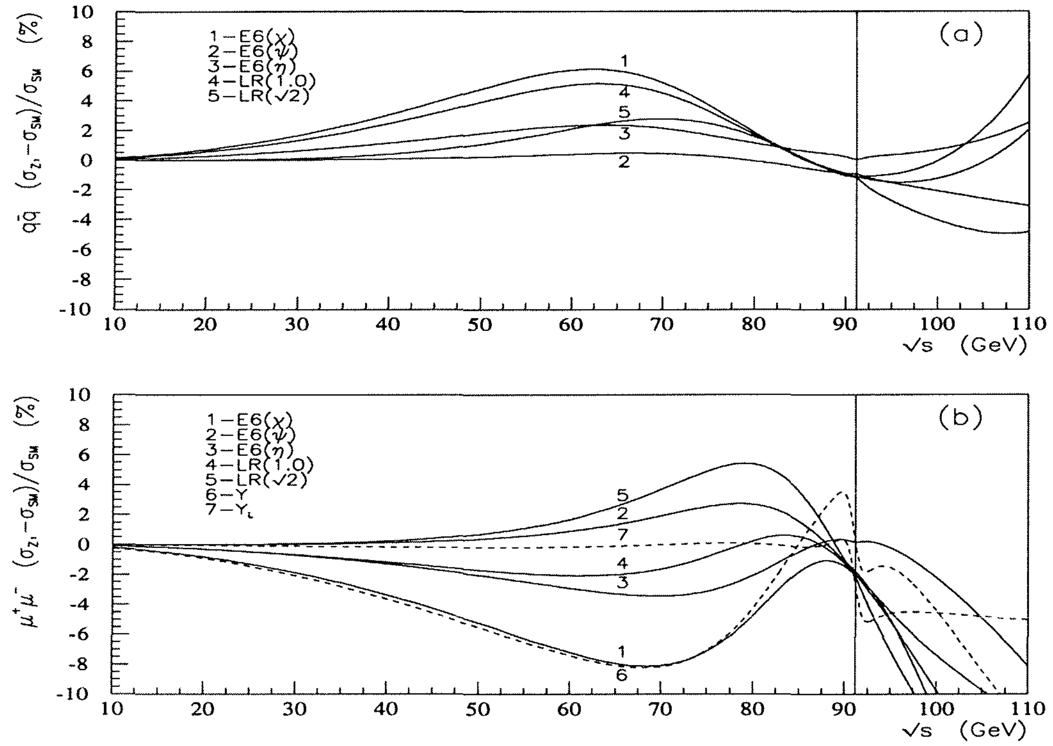

Figure 2.2: Fractional deviation: $(\sigma_{Z'} - \sigma_{SM})/\sigma_{SM}$, of (a) hadronic and (b) muon pair cross sections as functions of energy for several Z′ models. For the E_6 and L-R models $M_{Z'} = 150$ GeV, $\theta_{Z'} = 0.01$ radians and for the Y and Y_L models $M_{Z'} = 800$ GeV, $\lambda^2_{Y,Y_L} = 0.1$.

Chapter 3

LEP and DELPHI

3.1 The Large Electron Positron (LEP) Collider

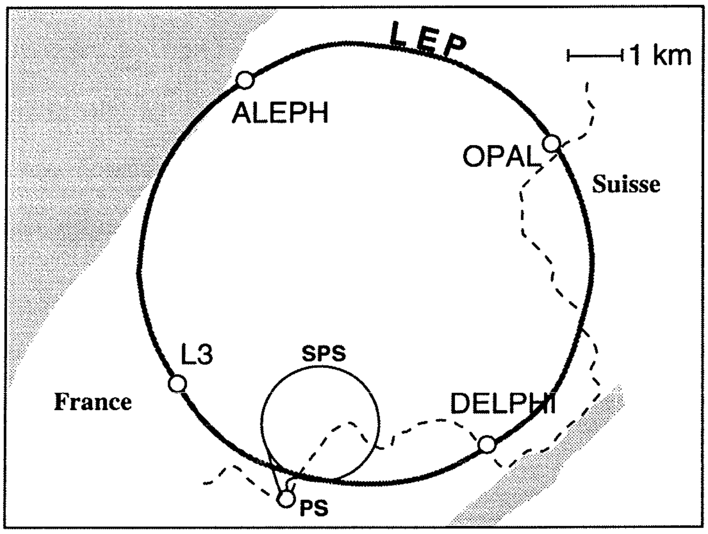

Figure 3.1: Plan of the LEP ring.

The LEP collider is an e^+e^- synchrotron storage ring currently operating close to the Z^0 pole, with beam energy $E_b \sim 45.6$ GeV; an operation phase referred to as LEP 1. Feasibility studies for a large e^+e^- collider at CERN began in the late 1970's, civil engineering commenced in 1983 and the first Z^0's were collected in August 1989. LEP is located within an underground circular tunnel of circumference 27 km, at a depth of between 50 and 170 m, stretching between the outskirts of Geneva and the foothills of the Jura mountains (see figure 3.1) The tunnel is not a perfect circle but rather is composed of eight arcs and eight straight sections, in the middle of four of which are large underground caverns housing the four experiments: ALEPH, DELPHI, L3 and OPAL.

The orbits of e^+ and e^- are controlled by some 3300 dipole magnets for bending as well as 1500 quadrupoles and sextupoles for focusing/defocusing. The energy loss per turn, ΔE, due to synchrotron radiation, for an electron of energy E circulating in LEP is:

$$\Delta E = 0.0885 \frac{\mathrm{E}^4(\mathrm{GeV})}{\rho(\mathrm{m})}, \tag{3.1}$$

where ρ is the radius of curvature. This loss is of the order of 130 MeV in the energy region of the Z^0; it is compensated for by RF cavities, which are grouped in two RF stations located close to OPAL and L3. Broadly speaking the total cost of the LEP collider is composed of two elements, the cost of RF power supplies and cavities ($\propto \mathrm{E}^4/\rho$) and the tunneling and magnet costs ($\propto \rho$). Minimization of the total cost as a function of collider radius, ρ, in order to achieve the design energy E shows the optimum radius and cost to scale as $\sim \mathrm{E}^2$. Such considerations led to the large radius of curvature of the arcs of LEP. Each of the beams is composed of eight equally spaced bunches (prior to mid 1992 four bunch operation was used), each bunch being composed of some $\mathcal{O}(10^{12})$ particles. Ideally the LEP luminosity $\mathcal{L}$[1] is given by:

$$\mathcal{L} = \frac{\mathrm{f\,bN_1N_2}}{4\pi\sigma_x\sigma_y}, \tag{3.2}$$

where f is the LEP revolution frequency, N_1 and N_2 are the number of particles per bunch, b is the number of bunches per beam and σ_x and σ_y represent the RMS beam dimensions perpendicular to the beam direction (the shape is assumed Gaussian, x is horizontal and y vertical). In LEP 1 with four bunches, where f = 10.8 kHz (one turn in 96 μs, one crossing every $\sim$ 23 μs), $N_1 = N_2 = 1.71 \times 10^{12}$, $\sigma_x = 250\ \mu$m and $\sigma_y = 15\ \mu$m the design luminosity is $1.7 \times 10^{31}\,\mathrm{cm^{-2}s^{-1}}$. After mid 1992 LEP changed from 4 bunch to 8 bunch per beam operation; the typical luminosity achieved is $1.4 \times 10^{31}\,\mathrm{cm^{-2}s^{-1}}$.

The integrated luminosities and number of hadronic Z^0's per running period for DELPHI are given in table 3.1. As shown in the table, scans of the centre-of-mass energies in a range $\sqrt{s}$=$M_Z \pm 3$ GeV were performed in 1990 & 1991 and the running in 1992 was entirely at the Z^0 peak. The data recorded by the four LEP experiments

---

[1] Luminosity is a measure of the useful flux of beam particles, it relates the event rate R to the cross section of the physical process σ in the equation: $R = \mathcal{L}\sigma$.

until the end of 1992 correspond to approximately $5 \cdot 10^6\,Z^0$ decays into hadrons and charged leptons.

Collision energy (GeV)			$\int \mathcal{L}\mathrm{d}t$ (nb^{-1})	Number of events
1990	1991	1992		
88.223			367.5	1602
	88.464		711.1	3495
89.222			444.1	3655
	89.455		632.7	6023
	90.208		622.6	10589
90.217			389.0	6777
	90.240		56.8	1018
	91.208		2482.5	70993
91.217			2831.7	83311
	91.239		4221.8	120190
		91.280	23955.0	696543
	91.953		666.1	15702
92.209			423.0	8803
	92.953		634.6	8531
93.208			467.2	5685
	93.702		681.2	6536
94.202			470.9	3565

Table 3.1: The number of hadronic events selected by DELPHI in 1990 [27], 1991 [28] & 1992 [29] and corresponding integrated luminosity at the various energy points demonstrates LEP operation and performance.

A complicated injector system, shown in figure 3.2, is used to accelerate electrons and positrons up to 20 GeV prior to injection into the main LEP ring. The diagram shows the two LINAC's (Linear accelerators) of which the first is used to deliver an intense electron beam onto a tungsten target to produce positrons and the second to accelerate both electrons and positrons to 600 MeV prior to accumulation in the EPA (Electron Positron Accumulator). After this the Proton Synchrotron (PS) and Super Proton Synchrotron (SPS) are used to accelerate electrons and positrons up to 3.5 and 20 GeV respectively.

Detailed descriptions of the design of LEP and the injector chain can be found in [30] and [31].

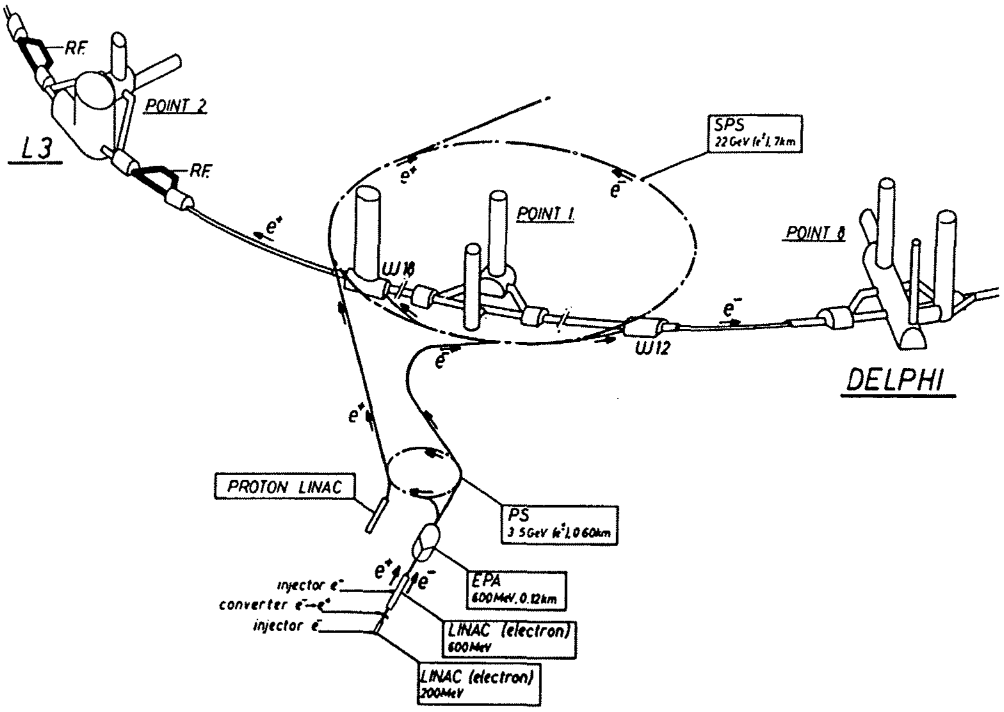

Figure 3.2: The LEP injector Complex

3.2 LEP Energy Measurement

In the determination of the mass of the Z^0, M_Z, from the energy dependence of $e^+e^- \to$ hadrons and $e^+e^- \to l^+l^-$ around the Z^0 resonance, the dominant error is from uncertainties in the LEP energy scale. As a result a great deal of effort has been expended in reducing this uncertainty using four techniques of measuring the energy; a detailed description can be found in [32].

Of the four techniques, *resonant depolarization* is by far the most precise method; it was first used towards the end of the 1991 running period. The technique relies on the natural transverse polarization which can be acquired by electrons circulating in LEP and the very accurately known relationship between the beam energy E_b and the number of spin precessions per revolution about the vertical bending field, the spin tune ν_s:

$$E_b = \frac{\nu_s \times m_e c^2}{(g_e - 2)/2} \equiv 0.4406486(1)\text{GeV} \times \nu_s, \tag{3.3}$$

where $(g_e - 2)/2$ is the anomalous magnetic moment of the electron, m_e the electron mass and c the speed of light.

Application of an oscillating horizontal magnetic field causes the spins of electrons to be slightly rotated away from the vertical axis on the each turn resulting in a depolarizing resonance if the frequency of the applied field matches the electron's spin precession frequency. Observation of the transverse polarization by means of a Compton-scattering laser polarimeter as the depolarization frequency is measured in successively smaller ranges.

Prior to application of the resonant depolarization technique the error contribution to M_Z from the LEP energy scale was ~ 20 MeV, compared to ~ 6 MeV achieved subsequently.

3.3 DELPHI in outline

The DELPHI (DEtector with Lepton, Photon and Hadron Identification) Experiment is one of the four large multipurpose detectors located on the LEP collider. The DELPHI Collaboration is composed of over 500 physicists and engineers from some 50 institutes, as shown in Appendix A. DELPHI was designed to have hadron and lepton identification over nearly 90% of the full solid angle, fine spatial granularity of all the components and three-dimensional information on every track and energy deposit.

The basic layout (shown in figures 3.3 and 3.4) is of a central 'barrel' part and two 'end-caps' (or 'forward' regions), comprising in total some eighteen different sub-detectors. Brief descriptions of the more important of these detectors for this analysis are provided below; further details can be found in [33] and the references therein.

The DELPHI coordinate system used throughout is illustrated in Appendix B, with the z direction coincident with the electron beam direction (electrons circulate anti-clockwise around the LEP ring), the y direction vertical and the x direction towards the centre of the LEP ring. A cylindrical coordinate system (R,ϕ and z) is also used; with the product Rϕ often being used in the description of points on a cylinder of radius R, the angle ϕ being taken from the positive x direction. The polar angle θ defined with respect to the positive z direction is also used.

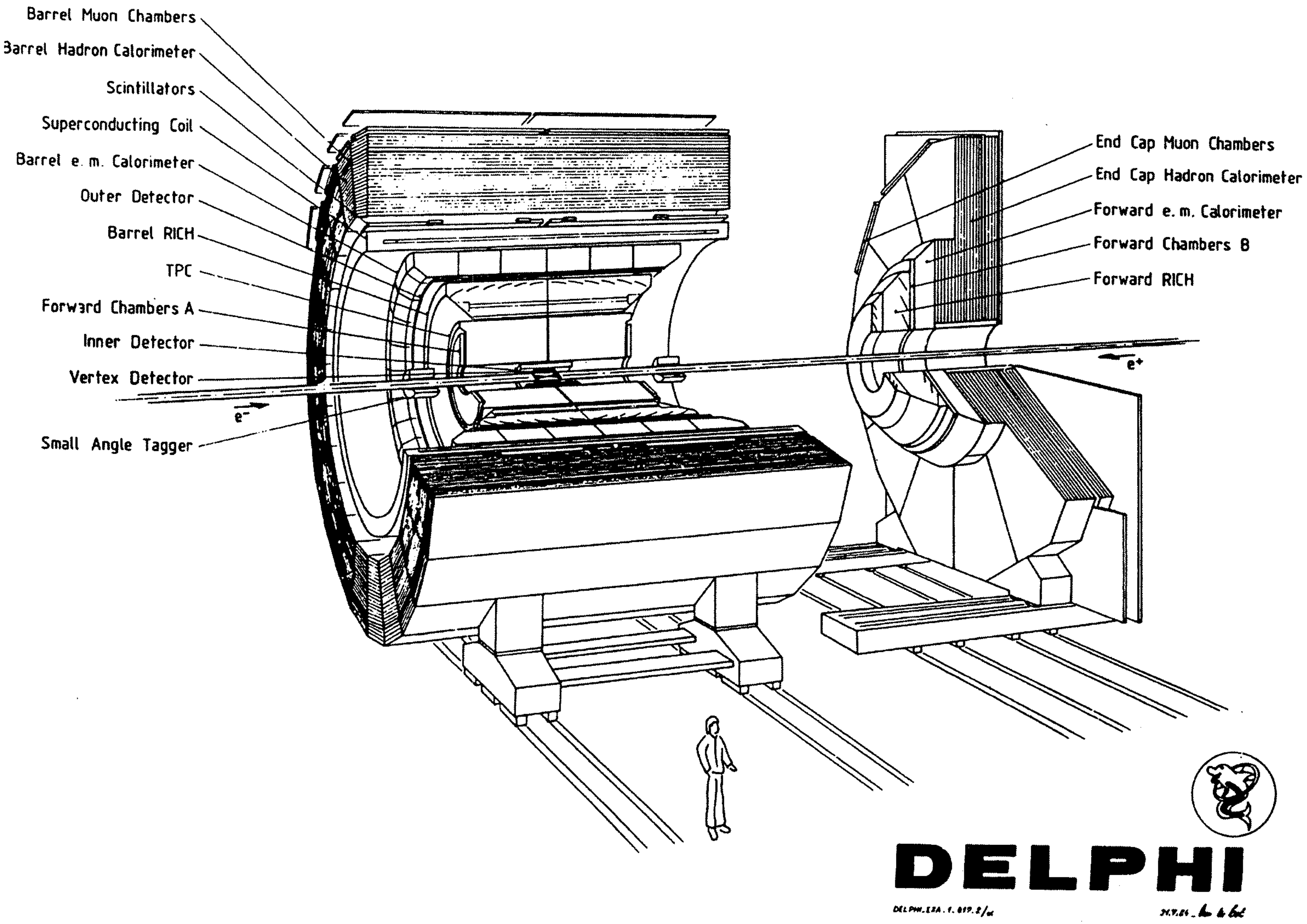

Figure 3.3: Perspective view of the DELPHI detector.

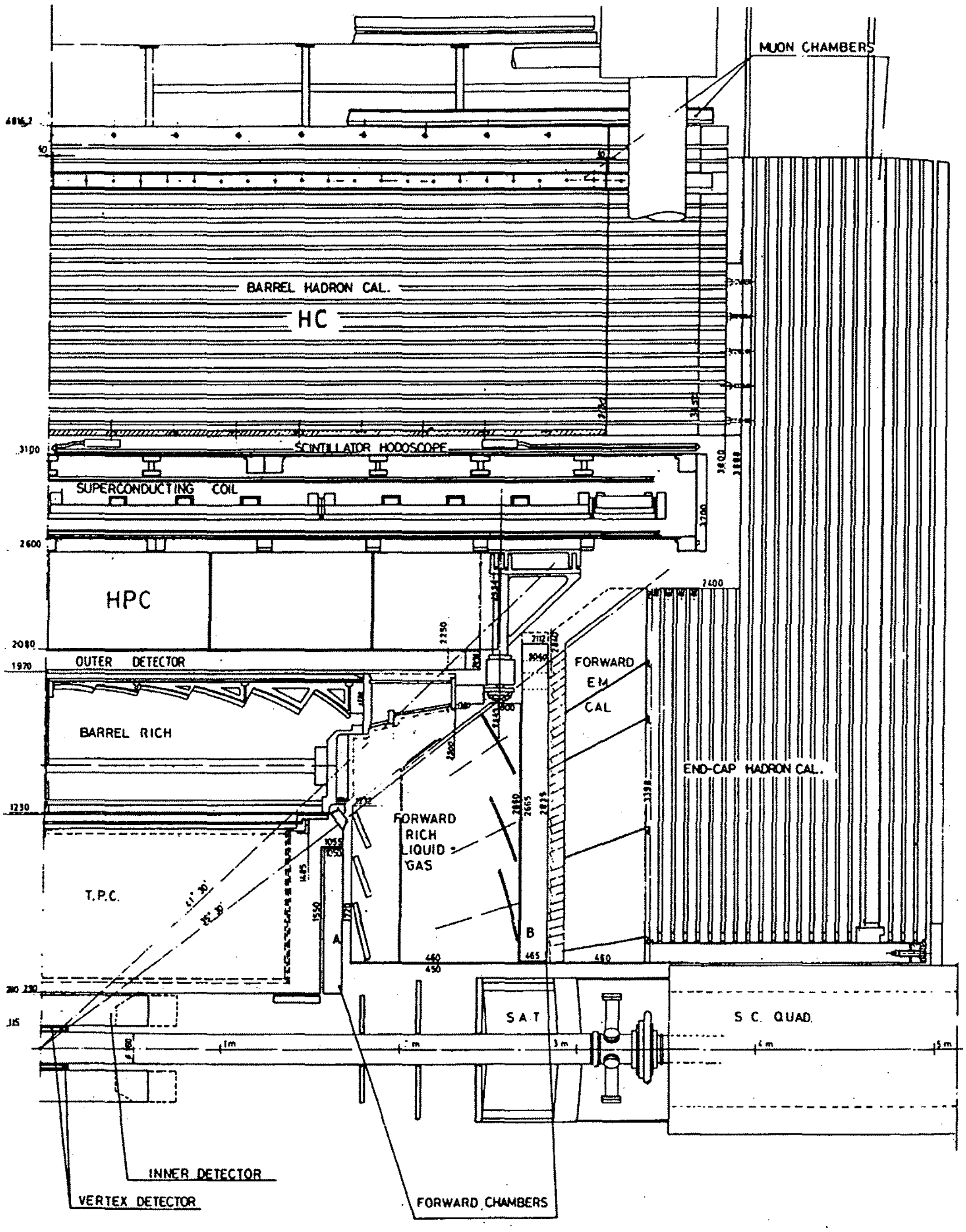

Figure 3.4: Cross-section of the DELPHI detector parallel to the e^+e^- beams.

3.4 Tracking of charged particles in DELPHI

In this section the specifications and performance of the DELPHI tracking detectors are discussed. Table 3.2 provides a summary with dimensions, acceptances and resolutions; further details and description for the main tracking detectors are provided below. A description of the techniques of combined tracking and the momentum resolution attained are also given.

The superconducting solenoid of length 7.4 m and internal diameter 5.2 m provides an approximately uniform axial magnetic field in the volume of the tracking detectors, with nominal magnitude of 1.23 Tesla. This allows the curvature of tracks produced by charged particles and thus the momenta of the particles to be measured.

In the barrel [2] the tracking is provided by the VD, ID, TPC and OD. In the forward region the TPC (down to 20°), FCA and FCB are the principal tracking detectors.

	Position/fiducial Acceptance			No. Points along Track	Resolution per point (σ) (mm)
	r (cm)	$\lvert z\rvert$ (cm)	θ(deg)		
VD (1990)	9/11	≤ 12	$37-143$	2	$r\phi$: 0.007
VD (1991)	6.3/9/11	≤ 12	$28-152$	3	
ID:					
jet chamber	$11.8-22.3$	≤ 40	$17-163$	24	$r\phi$: 0.11
trigger layer	$23-28$	≤ 50	$30-150$	5	$z :< 1$
TPC	$35-111$	≤ 134	$20-160$	16	$r\phi$: 0.23
				192	z: 0.9
OD	$198-206$	≤ 232	$43-137$	5	$r\phi$: 0.11
				3	z: 44
MUB	~ 445	≤ 385	$52-128$	$2-6$	$r\phi$: 1.5
					z: 10
FCA	$30-103$	$155-165$	$11-33$	$2\times(x,u,v)$	x,u,v: 0.3
FCB	$53-195$	$267-283$	$11-35$	$2\times(x,u,v)$	x,u,v: 0.25
MUF	$70-460$	463	$9-43$	$(2+2)\times(x,y)$	x,y: 1.0
		500			z: 10

Table 3.2: Specifications and performance of the DELPHI tracking detectors.

---

[2] The barrel region is defined as the angular acceptance of the OD: $43° < \theta < 137°$.

3.4.1 Vertex Detector (VD)

The VD [34], illustrated in figure 3.5, provides high precision measurements of the position of tracks from charged particles close to the primary collision point in the plane transverse to the beam, allowing accurate track reconstruction and precise extrapolations to the interaction region. This facilitates the reconstruction of primary and secondary vertices in hadronic events and significantly contributes to achieving good momentum resolution in leptonic events. The VD is composed of three[3] concentric shells of silicon microstrip detectors at average radii 6.3, 9 and 11 cm, referred to as the 'Closer','Inner' and 'Outer' shells, which surround the beryllium beampipe of inner radius 5.3 cm[4] and the interaction point. The microstrip detectors have a diode pitch of 25 μm and a readout pitch of 50 μm which provide precise measurements of the tracks of charged particles in the Rϕ direction.

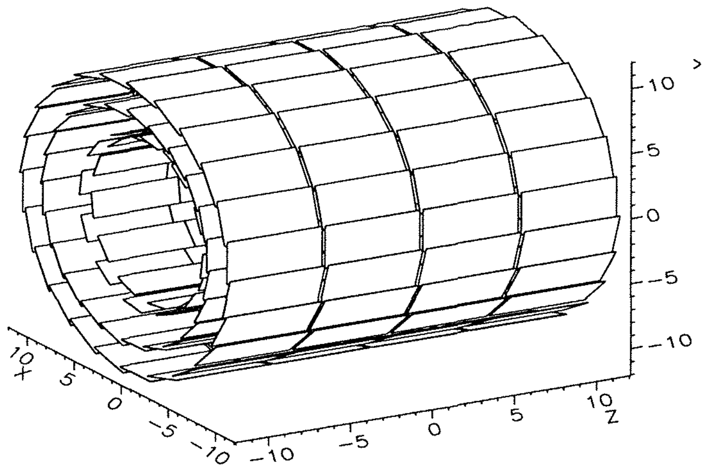

Figure 3.5: Perspective view of the three layer Microvertex detector, each shell consisting of 24 modules which are made up of 4 silicon detectors with strips parallel to the beam direction.

The intrinsic precision with which the cluster position is measured is dependent on many variables, such as the track incidence angle and the cluster size; it is in the range 6-9 μm. In order to make best use of this high precision measurement a careful

---

[3] Exceptions were in 1990 when only the Inner and Outer layers were present and 1989 when the VD was not installed.

[4] In 1990 a larger aluminium beampipe was used.

alignment procedure is performed with surveying to $\sim 20\,\mu$m (within a half-shell) initially and then alignment using data from both muon-pair and hadronic events, making use of track information from the Outer Detector (OD). This alignment uncertainty combines with the intrinsic precision to give a single track position uncertainty in the Rϕ plane of $\sigma_{\mathrm{meas(VD)}} = 11\,\mu$m.

3.4.2 Inner Detector (ID)

The ID [35] consists of two concentric parts: a jet type chamber with 24 azimuthal sectors for measurement of tracks in the Rϕ plane and 5 cylindrical MWPC[5] layers to measure the z coordinates of tracks by cathode strip readout. The field configuration and gas composition in the jet chamber are chosen to make the drift velocities proportional to the total drift distance, in the wedge shaped chamber. This facilitates the use of the ID as a fast track trigger selecting tracks coming from the interaction region as the 24 (or less) anode pulses per track will be coincident[6] or nearly so for such tracks. The outer 5 layers of MWPC each have 192 wires and 192 circular cathode strips of pitch ~ 5 mm; the wires provide fast trigger information and the cathode strips give z information.

3.4.3 Time Projection Chamber (TPC)

The TPC [36] is DELPHI's principal tracking device, the information it provides forms the basis of the pattern recognition performed in event processing. Due to the presence of the RICHs which surround it, the size of the TPC is limited; it is an annular shape with inner and outer radii of 30 and 122 cm, and length of 2×150cm. It consists of a volume of Ar/CH$_4$ (ratio 80:20) gas at 1 atmosphere divided in two by a plane at z=0. Uniform axial drift electric fields (150 V/cm) directed towards this central plane are maintained. The ionization electrons produced by a charged particle crossing the gas volume ($\sim$ 70 electrons per cm) are drifted towards one of the two readout planes at the extremities of the detector, allowing three dimensional track reconstruction from the projected Rϕ and timing information.

The readout planes are divided into six 60° sectors, shown in figure 3.6 with the first sector boundary at $\phi = 30°$, each have 1680 pads arranged in 16 circular

---

[5] MWPC stands for Multi-Wire Proportional Chamber

[6] Bending and displacement of tracks can be neglected in the 10 cm track segment of the jet chamber provided the transverse momentum is more than 1.5 GeV

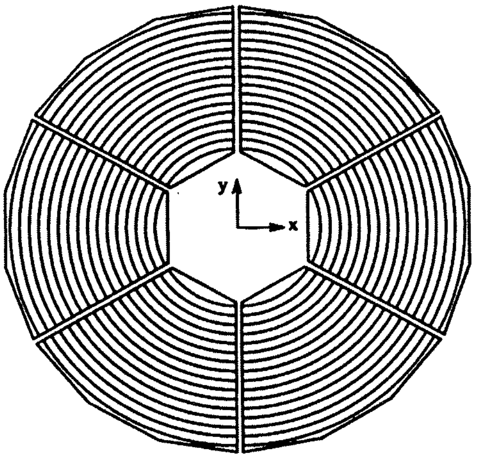

Figure 3.6: View of the 6 sectors that make up the a TPC readout plane, each sector with 16 circular pad rows.

pad rows and 192 sense wires perpendicular to a radial line through the centres of the sectors and positioned 4 mm from the cathode pad plane. Arrival times of the electrons at the sense wire anodes give the z coordinate of the track, with resolution $\sigma_z = 0.9$mm as well as the wire hit providing R information. Also the sizes of the up to 192 anode pulses provide dE/dx information, with resolution $\sigma \sim 6\%$ for 45 GeV muons. The avalanche occurring close to the anode wire results in the motion of positive ions away from the anode, inducing a pulse on the cathode pads. The pulse size is proportional to the distance from the avalanche to the pad; thus allowing the Rϕ coordinate to be reconstructed from the centre-of-gravity of induced charges on the pads, with resolution $\sigma_{R\phi}$= 120-180 μm (dependent on ϕ and z), much better than the pad dimensions.

3.4.4 Outer Detector (OD)

The OD [37] provides precise track measurements in the Rϕ plane at a radius greater than that available in the TPC. As a result the momentum resolution is improved by a large factor (>5 for fast particles). In addition the OD provides fast trigger information in both Rϕ and z.

The OD is required to fit into the annular region of inner and outer radii 1.97 & 2.08 m and length 4.86 m; between the RICH and the HPC. It consists of 24 identical planar overlapping modules arranged to form a “cylinder”. Each module is composed of 145 drift tubes arranged in 5 layers, the tubes have a square-cross-section with a central anode wire. The drift tubes are operated in the limited streamer mode with a wire diameter of 110μm. All layers provide Rϕ information, three in addition provide fast z information by relative timing of signals from both ends. The thin-walled aluminium construction of the OD leads to a total transverse thickness corresponding to 0.12% of a radiation length X_0.

3.4.5 Forward Chambers (FCA and FCB)

The forward chambers provide tracking and triggering in the endcap region, θ: 33°-11°, with drift cell construction similar to that of the OD. FCA and FCB provide 2 and 4 (x,u,v) measurements respectively from wire planes at constant $\pm$z positions; the (x,u,v) coordinates measured are non-orthogonal due to the rotation of groups of anode wires with respect to each other. For example, in FCA each side consists of 3 chambers which are turned with respect to each other by 120°. A more detailed description is provided in [38]. The resolutions obtained are $\sim$ 300$\,\mu$m per layer.

3.5 Combined tracking

Accurate extrapolation of tracks back to the vertex region and measurement of the momentum are the aims of the tracking system; the extent to which these aims are achieved is indicated by the impact parameter resolution and the momentum resolution. The impact parameter (in the Rϕ plane) is defined as the distance of closest approach of a given track to the primary interaction point in the Rϕ plane. Ideally for tracks coming from the primary vertex this should be zero, however the finite resolution of the track measurements from the sub-detectors used in the track fit (in the barrel region measurements from VD, ID, TPC and OD detectors are used) and the effects of multiple scattering of the material which the particle traverses both contribute to the impact parameter resolution. Thus the two contributions to the track extrapolation error, $\sigma_{\mathrm{R}\phi}$, are: the intrinsic measurement resolution (σ_{meas}) and the multiple scattering (σ_{scat}). Using the parametrization [39] [7]:

$$\sigma^2_{\mathrm{R}\phi} = \sigma^2_{\mathrm{meas}} + \frac{\sigma^2_{\mathrm{scat}}}{\mathrm{p}^2_{\mathrm{R}\phi}\sin\theta}, \tag{3.4}$$

---

[7] The factor of $\sin\theta$ in the 2nd term accounts for the variation of material thickness of that the particle traverses, assuming a uniform cylindrical distribution of the material.

where $p_{R\phi}$ (GeV/c) is the momentum component in the $R\phi$ plane (often termed the transverse momentum p_T) and θ is the polar angle; yields $\sigma_{\text{meas}} = 30 \pm 3\mu\text{m}$ and $\sigma_{scat} = 70 \pm 4\mu\text{m}$. The effects of multiple scattering are negligible for tracks of $p_{R\phi} > 10$ GeV/c, with the $\sigma_{R\phi}$ tending to the asymptotic value of σ_{meas}.

3.5.1 Beamspot position

The impact parameter resolution is the convolution of the track extrapolation accuracy and the precision on the determination of the primary vertex position. Electron-positron collisions within the DELPHI beampipe occur in a small region which can be described by a two-dimensional gaussian in the x-y plane with widths estimated in [40] to be $\sigma_{\text{x-beam}} = 142 \pm 5\mu\text{m}$ and $\sigma_{\text{y-beam}} = 7^{+3}_{-7}\mu\text{m}$. The technique used to determine the centre of the electron-positron interaction region or beamspot position (x_{beam},y_{beam}), on a run-by-run [8] basis is also described in [40]; typical errors obtained on x_{beam} and y_{beam} were $8\,\mu\text{m}$ and $15\,\mu\text{m}$ respectively.

3.5.2 Momentum resolution

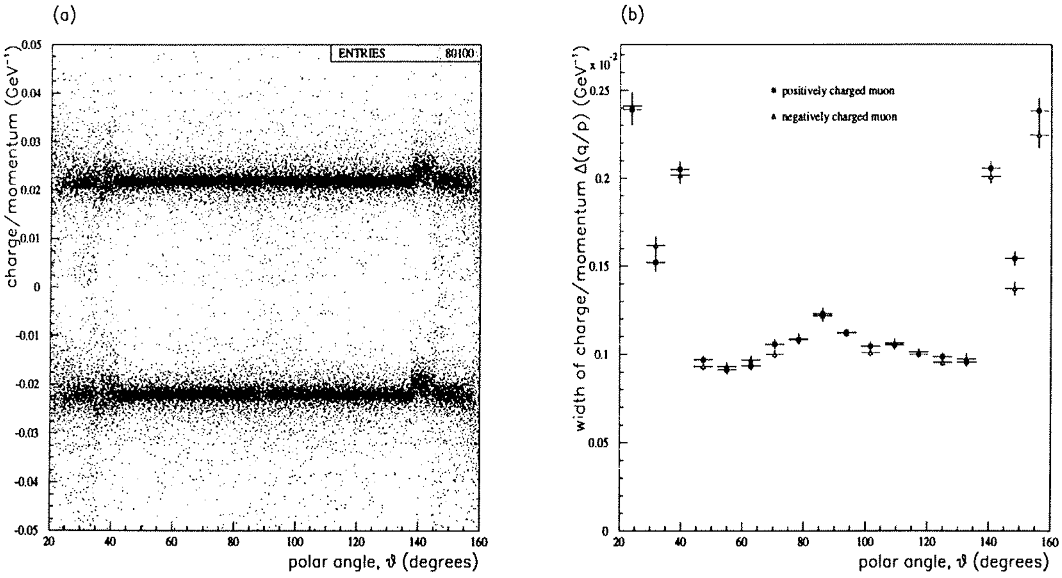

Figure 3.7: (a): Charge over momentum q/p as function of θ. (b): Gaussian widths of the q/p distributions for reconstructed μ^+ and μ^-.

The momentum resolution achieved by the combined track fit for muons in muon-pair events was obtained from the measured momenta in events selected with the

---

[8] A **run** is a period of data taking; typically $\mathcal{O}(10)$ runs make up a **fill** of the LEP machine.

'hard' selection described in section 4.2. Figure 3.7(a) shows the distribution of electric charge divided by momentum as a function of polar angle θ, for reconstructed tracks from a sample of 40050 muon-pair events.

The momentum resolution for muons with $\mathrm{p} = 45.6$ GeV, is given by $\delta\mathrm{p}/\mathrm{p} = \mathrm{p}\,\delta(1/\mathrm{p})$; $\delta(\mathrm{q}/\mathrm{p})$ for $\mathrm{q} = \pm 1$ as a function of θ is shown in Figure 3.7(b). In the barrel region $\delta\mathrm{p}/\mathrm{p} \sim 4.5\%$, rising to $\sim 11\%$ in the very forward region.

3.6 Scintillator counters

Scintillator counters: Time Of Flight (TOF) in the barrel and Forward Hodoscope (HOF) in the forward region, described in [33], provide a fast signal for incorporation in the 1st level trigger. The large time-of-flight difference of cosmic ray muons $\Delta t \sim 20$ns, compared to $\Delta t \sim 0$ns for the two muons in $\mathrm{e}^+\mathrm{e}^-$ interactions, measured in the TOF, allows cosmics to be rejected (or triggered on for alignment purposes); the time resolution achieved is $\sim 1-2$ ns. The HOF improves the trigger efficiency for beam event muons and beam-halo muons, which are useful in the alignment of the forward tracking detectors.

3.7 Calorimetry

	Position/fiducial Acceptance			Depth
	$r(cm)$	$\lvert z\rvert\,(cm)$	θ (degrees)	
HPC	$208-260$	≤ 254	$43-137$	$18X_0$
FEMC	$46-240$	$284-340$	$10-36.5$	$20X_0$
SAT	$10-36$	$233-285$	$2.5-7.7$	$28X_0$
VSAT	$\sim 6-9$	770	$5-7$ mrad	$24X_0$
HCAL (barrel)	$320-479$	< 380	$10-170$	6λ
HCAL (forward)	$65-460$	$340-489$		6λ

Table 3.3: Specifications and performance of calorimeters, X_0 and λ are defined in the text.

In this section the specifications and performance of the DELPHI calorimeters are discussed. Table 3.3 provides a summary with dimensions, acceptances and resolutions; further details and description for the main calorimeters are provided in the subsections below. Electromagnetic calorimetry is provided by the HPC in the barrel and the FEMC (often referred to as the EMF) in the forward region. Hadronic calorimetry is provided by the HCAL. The nature of the Bremsstrahlung interactions by which electromagnetic calorimeters operate, causes hadrons and muons to pass through the significant material of the electromagnetic calorimeters with little energy loss.

3.7.1 Electromagnetic calorimetry

The interactions of photons and electrons in matter at energies above 5 MeV are dominated by electron-positron pair production and by Bremsstrahlung, radiating photons while being decelerated in the Coulomb field of a nucleus. An alternating sequence of interactions of these two types leads to a 'shower' of electrons, positrons and photons which stops only when the energy of the particles falls below the critical energy (which is $\sim$ 10 MeV [41] for lead or lead glass) when ionization energy loss dominates over Bremsstrahlung energy loss. For massive particles the Bremsstrahlung interaction is inversely proportional to the square of the incident particle mass; consequently hadrons (predominantly pions) and muons deposit comparatively little energy, whereas electrons generate large and distinctive showers, and give up almost all their energy in these detectors. Photons of energy greater than 1 GeV interact with matter primarily by pair production (in the field of a nucleus to conserve momentum); a process closely related to electron Bremsstrahlung, with $\sim$ 7/9 of its cross section. Thus photons exhibit similar behaviour to electrons in the electromagnetic calorimeters.

The radiation length, X_0 [9], of a material varies with the atomic number Z approximately as $1/Z^2$. Electromagnetic calorimeters use high Z materials such as lead (Z=82), with a low X_0 value ($\sim$ 5.8 g/cm^2 cf. iron with $\sim$ 13.8g/cm^2), as these allow total containment of an electromagnetic shower within a reasonable length.

3.7.2 Material in front of calorimeters

Reconstructions of photons and electrons in DELPHI are complicated by the amount of material in front of the calorimeters leading to a considerable degradation of spatial and energy resolutions. Figure 3.8 illustrates the simulated conversion positions in material prior to the calorimeters; the detector boundaries where most

---

[9] X_0 is 1 radiation length: the thickness of material that reduces the mean energy of a particle by a factor of e, as indicated by the energy loss equation: $dE/E = -dx/X_0$, or $E = E_0 e^{-x/X_0}$

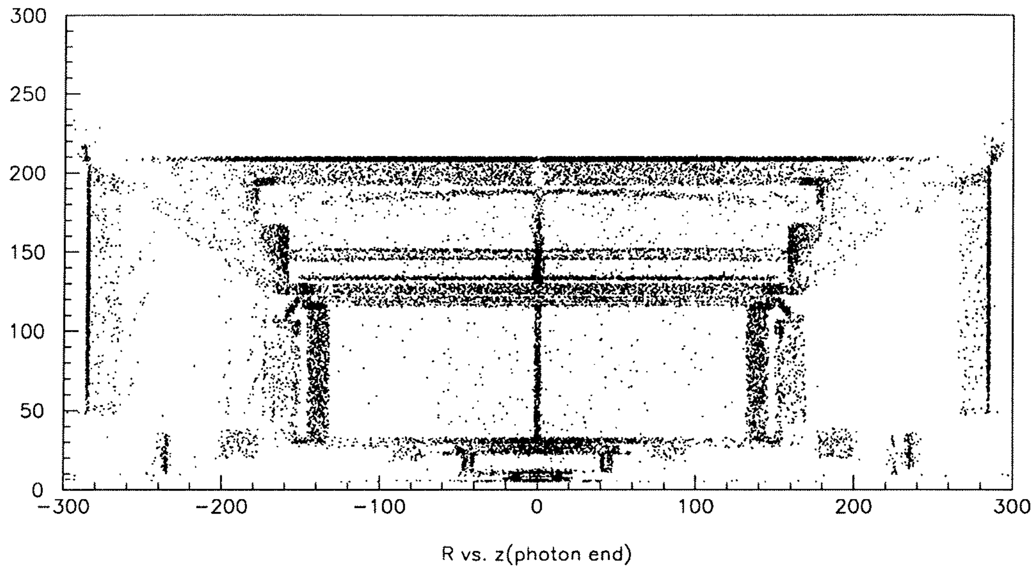

Figure 3.8: Photon conversion points from simulation, in R-z projection (scales in cm)

of the material is concentrated are clearly visible. In the barrel region this material corresponds to $\sim 0.8\,X_0/\sin\theta$ and in the forward region $\sim 2\,X_0$; as a result about 40% of photons from the interaction point convert before they reach the HPC [42].

3.7.3 High density Projection Chamber (HPC)

The HPC aims to measure the three-dimensional charge distribution induced by electromagnetic showers and by hadrons with high granularity in all coordinates. It is one of the first applications of the time projection technique to calorimetry. A polar angle range of $43^\circ<\theta<137^\circ$ is covered by the 144 trapezoidal modules that make up the HPC, segmented by 24 in azimuth and 6 in z; gaps between modules in the z direction are 1 cm, except for a 7.5 cm gap at z=0. Each module is constructed of 41 lead walls spaced by 8 mm gas gaps, the walls being constructed from trapezoidal cross section lead wires. The thickness of lead corresponds to a minimum radiation length of $18\,X_0$, ensuring total containment of the electromagnetic showers in almost all cases.

The principal of operation and construction is demonstrated by figure 3.9; the Bremsstrahlung interaction of charged particles [10] with the concentrated electric

---

[10] High energy photons are also detected due to pair production; the cross sections for electron pair production and electron Bremsstrahlung in the lead converter are comparable.

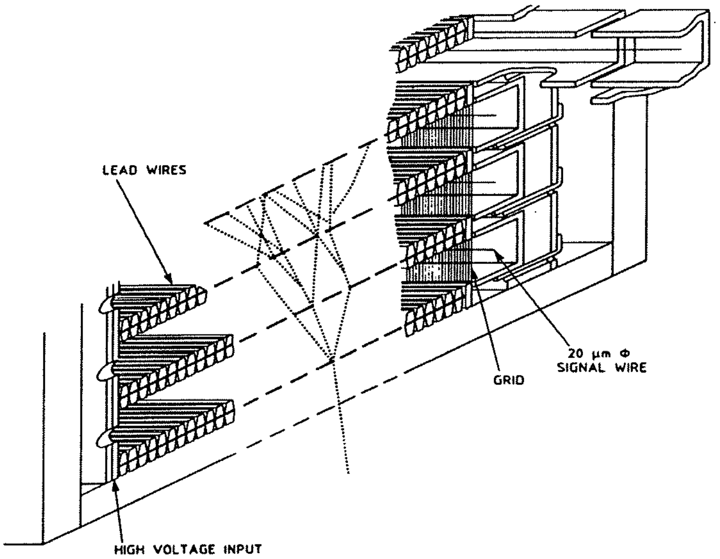

Figure 3.9: Cross section of HPC module showing the lead wire converter walls, drift channels and readout proportional tubes at one end of the channel. An illustrative $e^{\pm}$ or photon shower is shown.

charges of the lead converter produce photons which in turn undergo pair production or Compton scattering generating tertiary particles. In this manner charged particles or photons cause electromagnetic showers to build up, usually across several layers. The electrons produced by the showering process in the gas gaps between the converter layers are then drifted towards a proportional chamber with pad readout at the end of each module, by a uniform electric field aligned with the DELPHI magnetic field direction. As well as acting as the converter the lead wires are connected to a voltage divider to shape the drift electric field.

The radial and azimuthal coordinates of the charge distribution are obtained from the pad readout of the proportional chambers, shown in 3.10, and the z coordinate is obtained from the drift time. A granularity of 4 mm in z, 1° in azimuth and nine-fold radial sampling over 18 radiation lengths is achieved. The shower energy resolution obtained is $\sigma_{\mathrm{E}}/E = (23/\sqrt{E} + 1.1)\%$, E in GeV, with operational range designed to allow for showers of energy up to 50 GeV while maintaining full sensitivity for minimum ionizing particles (MIPs)[11]. For fast triggering purposes,

---

[11] After run 22094 in 1991, the HPC drift voltage was lowered by 100 V to reduce ageing of the calorimeter modules causing a significant drop in the efficiency for the detection of MIPs from 85% to 25%.

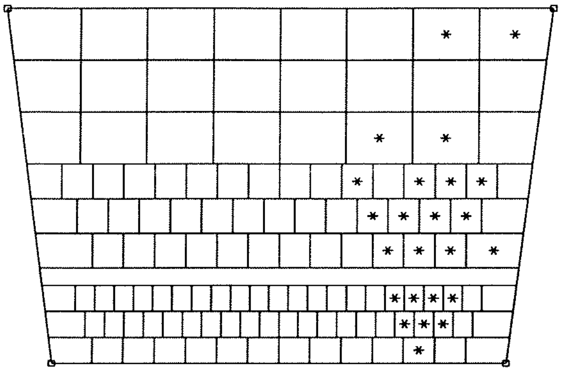

Figure 3.10: Pad layout of the readout chamber of one module, providing nine samples in R; the gap after 3 layers is where the trigger scintillator layer is located. The asterisks represent a possible set of pads hit due to an electron or photon.

a plane of scintillators is inserted into one of the HPC sampling gaps close to the shower maximum at a position after 4.5 radiation lengths.

3.7.4 Forward ElectroMagnetic Calorimeter (FEMC)

The FEMC consists of two 5 m diameter discs, one in each end-cap, covering polar angles $10^\circ<\theta<35.5^\circ$ and $143.5^\circ<\theta<170^\circ$. Each disc contains 4532 lead glass blocks in the form of truncated pyramids, arranged to point towards the interaction point. The thickness of the lead glass blocks corresponds to $20\,X_0$ on each side, the blocks have approximate dimensions $5\times 5\,\mathrm{cm}^2$, $\sim 1^\circ \times 1^\circ$. They are read out with vacuum phototriodes, giving an average gain of 12. The shower energy resolution obtained, without including the effects of the material encountered prior to the calorimeter, is $\sigma_\mathrm{E}/\mathrm{E} = \left[(0.35+5/\sqrt{\mathrm{E}})^2+(6/\mathrm{E})^2\right]^{1/2}\%$, E in GeV.

3.7.5 Hadron CALorimeter (HCAL)

Hadronic calorimeters are based upon the inelastic, as well as elastic, collisions between an impinging high energy hadron and the nucleons in a block of matter. In general several secondary hadrons are produced such as pions, kaons, protons or neutrons with sufficient energy to undergo further inelastic collisions. In this manner a hadronic 'shower' is formed, that stops only when the hadron energies are sufficiently small for the particles to be stopped by ionization energy loss or absorbed in a nuclear process. Due to the large angle scattering in nuclear processes compared to the small angle nature of electromagnetic processes the hadronic showers are comparatively broader. The longitudinal development scales with the nuclear absorption (or interaction) length $\lambda = \mathrm{A}/\mathrm{N_A}\sigma_{\mathrm{abs}}$, where A is the atomic mass, σ_{abs} is the absorption cross section ($\propto A^{0.7}$ [43]) and $\mathrm{N_A}$ is Avogadro's number. For hadrons of up to 45 GeV almost all the shower energy is contained within the first 5 interaction lengths.

The HCAL uses the iron of the superconducting coil return yoke to act as its converter; it is a sampling gas detector consisting of limited streamer mode detectors inserted into the 2 cm slots between the 5 cm iron plates of the return yoke. The $\sim$ 19032 multicell wire chamber detectors vary in length from 40 to 410 cm in order to facilitate a projective geometry pointing to the intersection point. HCAL construction in the barrel and the endcaps is similar, with 20 sampling layers in the barrel and 19 in the endcaps; arranged in 24 azimuthal sectors. A particle traversing the calorimeter sees a minimum of 110 cm of iron, corresponding to 6 interaction lengths.

3.8 Muon Chambers

The DELPHI muon chamber system is designed to identify muons by recording the tracks of charged particles that penetrate the $\sim$18-20 radiation lengths of the electromagnetic calorimeters and the $\sim$6 nuclear interaction lengths of the hadron calorimeter.

3.8.1 Barrel MUon chambers (MUB)

The MUB covers the polar region $52° < \theta < 128°$, it consists of three concentric layers of muon chamber modules wrapped around the DELPHI barrel; the modules are termed the inner, outer and peripheral chambers. The inner modules are embedded in the iron of the HCAL, they consist of 14 drift chambers arranged in 3 staggered layers (the outer of which is regarded as spare); the outer and peripheral modules both have 7 chambers arranged in 2 overlapping layers. The layout of modules and of chambers within modules for one of the 24 azimuthal sectors is shown in figure 3.11. Two such sets of modules at +ve and -ve z positions, each with typical active length 365 cm, for each 15° sector make up the barrel muon chambers.

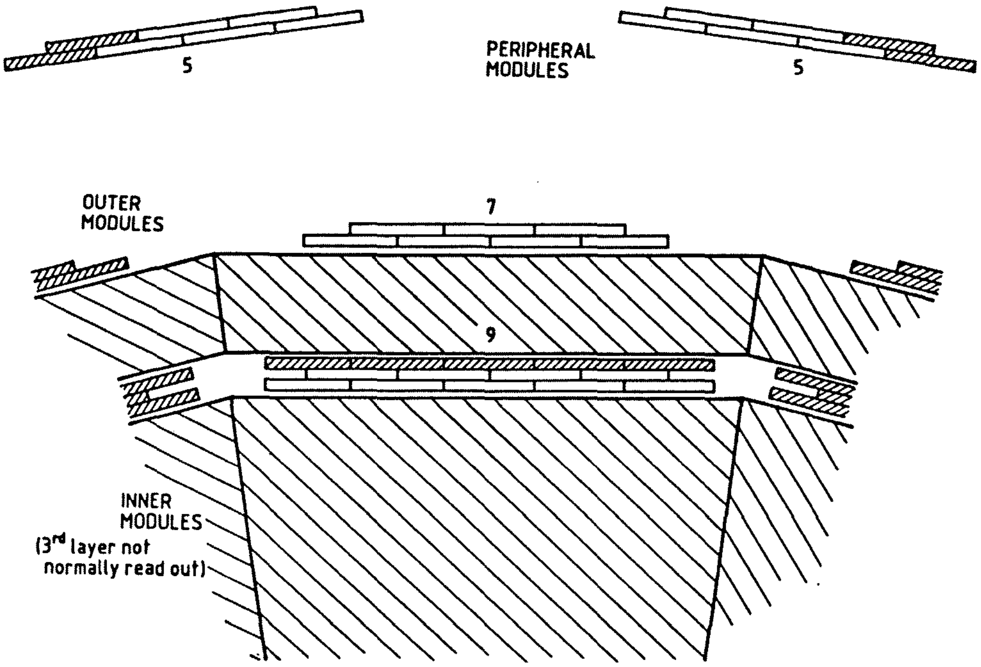

Figure 3.11: A sector of the barrel muon chambers

In total the MUB system is composed of 1372 drift chambers operated in proportional mode. Each chamber has a central 50 μm anode wire maintained at $\sim$ 6150 V positioned parallel to the z axis; with signal propagation speed of ~20 cm/ns. The cathode consists of 13 long thin copper grading strips along the top and bottom inner surfaces of the chamber, which are held at linearly varying voltages from 0 V at the edges of the chamber to +4000 V at the centre, adjacent to the anode wire. In this way a uniform drift electric field is established. A central strip of width 1.5 cm, wound with insulated copper wire, functions as a delay line with signal propagation speed ~0.5 cm/ns.

The principal of operation of drift chambers is as follows. Passage of energetic charged particle through the drift volume causes a number of ionizations, liberating electron-ion pairs. Under the influence of a constant electric field these are drifted away from each other, gaining energy from the field between collisions with gas molecules. On the macroscopic level the net motion of electrons is at a constant velocity ($v_d = (e/2m_e)E\tau$; τ is the mean time between collisions) in the direction opposite to the electric field. Thus the electrons are drifted towards the central anode wire of the drift chamber, where they encounter the rapidly increasing $\sim 1/r$

radial potential; r is the radial distance from the wire centre. Once the mean energy gained by the electrons exceeds the ionization potential of the gas a chain reaction or *avalanche* is set up, in which many more electron-ion pairs are produced. The electrons are rapidly collected by the anode while the less mobile +ve ions drift away from the anode, inducing pulses on the anode and on the cathode.

In the MUB drift chambers the three signal times from the anode and from the near and far ends of the cathode delay line are read out. Knowledge of the chamber drift velocity and delay line signal propagation speed allows the track position to be calculated from the 3 signal times. The delay line times provide the z position of the track and the anode time gives the Rϕ coordinate; with an ambiguity as to which side of the anode the track passed, which is resolved by combining the information from staggered layers of chambers. The resolutions attained are approximately 1 mm in Rϕ and 1 cm in z.

3.8.2 Forward MUon chambers (MUF)

The MUF is the endcap equivalent of the MUB, it is composed of two planes of chambers at z=±463 & 500 cm, each plane consisting of two orthogonal layers of limited streamer mode drift chambers. The resolutions attained in both the x and y directions are $\sim$ 3 mm.

3.9 Luminosity Measurement

Cross sections are determined via the relation:

$$\sigma = \frac{\mathrm{N_{sel}} - \mathrm{N_{bkg}}}{\epsilon \int \mathcal{L}\,\mathrm{dt}}, \tag{3.5}$$

where $\mathrm{N_{sel}}$ is the number of events passing the selection cuts and $\mathrm{N_{bkg}}$ is the number of background events in the selected sample. $\int \mathcal{L}\,\mathrm{dt}$ denotes the integrated luminosity and ϵ is a correction factor accounting for the trigger efficiency, geometrical acceptance and efficiency of selection.

The luminosity is obtained from the ratio of the number of events measured in small angle Bhabha scattering and the theoretical prediction for the cross section of this process within the acceptance of the luminosity monitor. Small angle Bhabha scattering is a process which is almost entirely dominated by well understood QED effects, with a small $\sim$ 1% electroweak correction. The total Bhabha scattering cross section within an acceptance defined by angles $\theta_{\rm min}$ and $\theta_{\rm max}$ is given ,in the Born approximation to lowest order, by [13]:

$$\sigma_{\rm T} \approx \frac{16\pi\alpha^2}{s}\left(\frac{1}{\theta^2_{\rm min}} - \frac{1}{\theta^2_{\rm max}}\right). \tag{3.6}$$

This demonstrates the importance of a precise knowledge of the acceptance of the luminosity monitor.

A detailed description of the luminosity analysis indicating how results from SAT and VSAT were combined to achieve the minimum uncertainties can be found in the DELPHI electroweak papers, referenced from the caption to table 3.1.

3.9.1 Small Angle Tagger (SAT)

The SAT is the principal detector used for the measurement of the absolute luminosity in DELPHI [12]. It is a calorimeter composed of cylinders of lead sheet and plastic scintillating fibres concentric with the LEP beam, covering polar angles from 43 to 135 mrad. The inner edge of the fiducial region is accurately defined by a precisely machined lead[13] mask $12\,X_0$ deep covering the inner region of one arm of the calorimeter, as shown in figure 3.12. The position of the conical outer surface of the mask is determined by the region where the energy deposition observed is very much reduced (usually by $\sim$85%), establishing the acceptance radius to $<100\,\mu$m.

3.9.2 Very Small Angle Tagger (VSAT)

Each arm of the VSAT is mounted 7.7 m from the interaction point, beyond the superconducting quadrupole magnets, covering polar angles from 5 to 7 mrad. The detector in each arm is composed of two rectangular tungsten-silicon calorimeter stacks, $24\,X_0$ deep covering azimuthal angles ±45° around the horizontal axis. The VSAT is used for fast monitoring of relative luminosity and machine operation.

Within the very low angle region of the VSAT acceptance the cross section is $\sim$ 400 nb, leading to an event rate 10 times the Z^0 rate at the pole. The measurement of the absolute luminosity is limited by uncertainties in the geometry and in the

---

[12] The SAT was replaced by a new calorimeter called the STIC for the beginning of the 1994 running period.

[13] The lead mask was replaced by a tungsten mask towards the end of the 1992 running period.

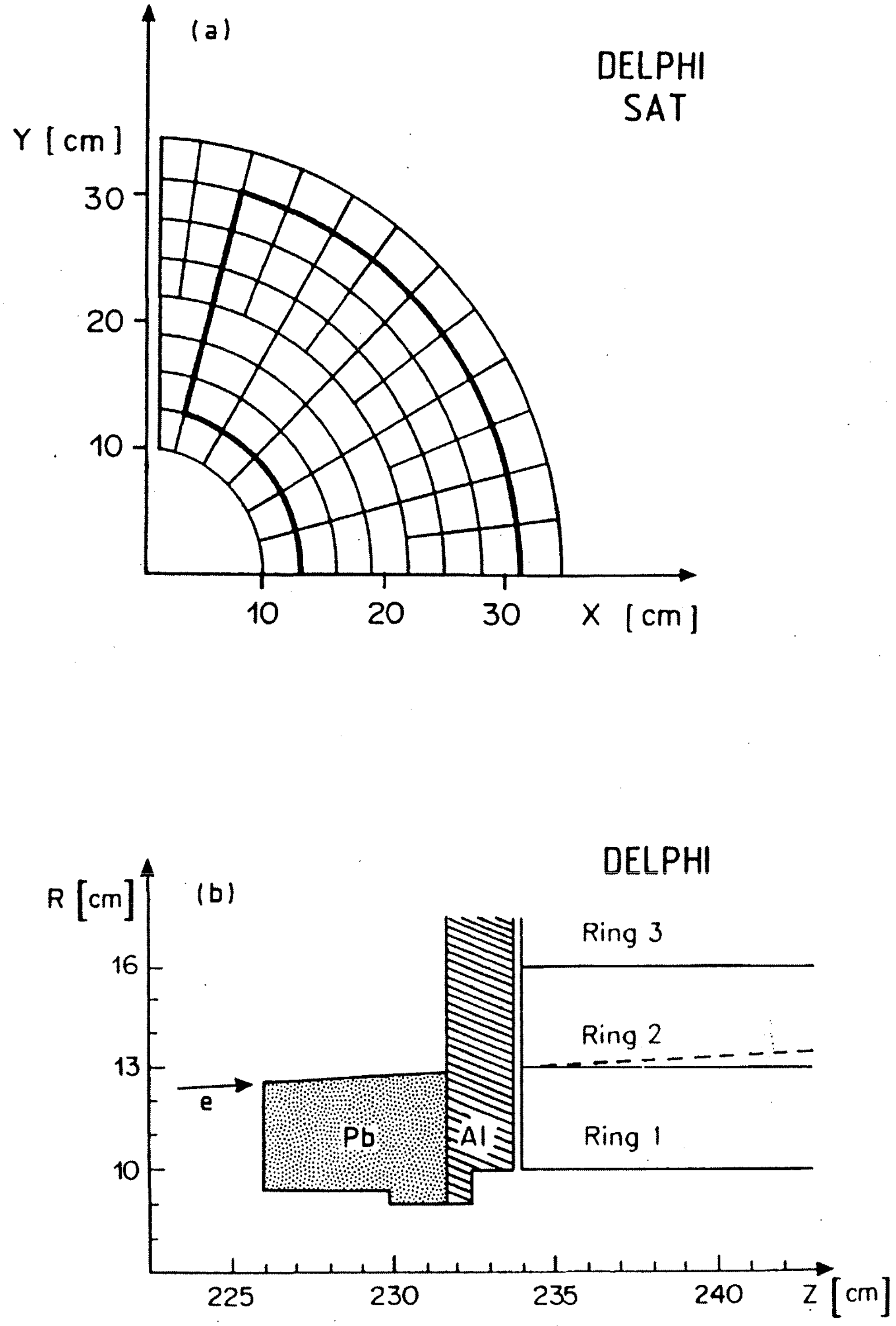

Figure 3.12: Small angle tagger (SAT): (a) Segmentation of readout. (b) Lead mask used on one arm.

theory, but the high statistics available makes the relative luminosity measurements from the VSAT useful. An important factor in the acceptance uncertainty is the bending of the particle paths in the magnetic field of the superconducting quadrupole magnets. After normalisation to the SAT measurement at the peak energy point, the VSAT off-peak measurements achieve smaller uncertainties than the statistics limited SAT measurements.

3.10 Data Acquisition System (DAS) and Trigger

The DAS aims to read out data from the the individual sub-detectors at each beam cross over (BCO), store this data in memory while a trigger decision as to whether to keep the event is made. In the case of detectors with long drift times, the 'memory' is in the form of the electrons drifting through the gas volume. It is the short time between BCO's of $22\,\mu s$ (45 kHz)[14] compared to the time to free the detector's front end buffers of $350\,\mu s$ that makes it impossible to read out every BCO.

The trigger system is organised in 4 levels[15] to cope with high luminosities and backgrounds, the 1st and 2nd level are hardware triggers operating synchronously with BCO i.e. for every BCO, both decisions have to be completed before information from another BCO can be taken. 1st and 2nd level trigger decisions (T1 and T2) are made 3 μs and 40 μs after BCO. The first level T1 trigger acts as a pre-trigger using only minimal information such as energy or transverse momentum thresholds satisfying multiplicity requirements. Information used at the T2 level is more refined with correlations between data from different detectors being made, also data from detectors with long drift times are now taken into account. The many components of the trigger are loosely grouped into classes which trigger on tracks, muon signals, electromagnetic energy deposits, hadronic energy deposits and Bhabha events.

Each sub-detector has its own front end electronics modules and one or more FASTBUS Intersegment Processors (FIPs) which include local crate event buffers (CEBs) and a crate processor (CP). After a positive T2 the CPs control the readout from the front end electronics into the CEBs. Local T3 processing is performed by

---

[14] These numbers refer to 4-bunch operation of LEP; during 8-bunch running the rate is twice this.

[15] T3 was enabled from the running period of 1992 and T4 from 1993.

the CPs, repeating the T2 logic with higher granularity and with access to more information.

T3 and T4 are software filters, working asynchronously with BCO, i.e. there is no holdup in data taking given sufficient processing speed (typically 300 ms) and memory to hold several events. T4 acts to reject events regarded as "empty". The contents of the CEBs from each of the sub-detectors are grouped together in the Global Event Buffers (GEBs) and written to disk and then to IBM 3480 cartridges after a positive T4 decision; these are the raw data tapes.

3.11 DELPHI Off-line Processing

The DELPHI data passes through three stages before physics analysis; they are outlined below.

- **Raw Data.** The data readout from the DELPHI experiment and written to tape in the DELPHI control room, consisting of signals, times and pulse heights.

- **TANAGRA Data.** The DELANA (DELphi ANAlysis) [44] program, described below, processes the Raw Data performing a detailed reconstruction to produce the TANAGRA[16] data structure. The large volume of this TANAGRA data makes a further reduction to Data Summary Tapes (DSTs) necessary before physics analysis can be performed on the large data sets collected.

- **DST Data.** A package called PXDST copies data from TANAGRA into the DST [46] structure. The DST data is organised in track banks, with blocklets attached containing information such as fitted track parameters, associated calorimeter deposits and RICH particle identification information.

3.11.1 Event reconstruction

The DELANA processing can be divided into the following stages:

---

[16] TANAGRA [45] stands for Track ANalysis and GRAphics package; it is a data format as well as a suite of routines for accessing the data.

- **Local reconstruction.** The data from each detector are analysed separately to produce Detector data (TDs) such as: space points, energy deposits and times. Track elements (TEs) for tracking detectors are formed by fitting a track through a combination of space points within a sub-detector. For calorimeters TEs are formed from a clustering of energy deposits.

- **Track fit.** TEs from tracking detectors are grouped together to form candidate tracks or Track Strings (TSs). These 1st stage tracks are extrapolated throughout the detector and track parameters at the entry points to the detector elements are computed, for use at the 2nd stage. The 2nd stage full track fit resolves ambiguities and reconsiders unused TEs; new extrapolations are performed providing full track (TK) parameters. Energy depositions in the calorimeters are linked to the extrapolations.

- **Particle identification.** RICH, dE/dx and muon chamber information are linked to the tracks.

- **Neutral reconstruction.** Neutral tracks are made from unassociated energy deposits, not attached to the reconstructed charged tracks.

3.11.2 Detector simulation

The DELPHI simulation package (DELSIM [47]) follows generated **truth** particles through the detector, modelling detector response: accounting for the effects of the material encountered with secondary particle production and conversions (in the case of photons). Four-vectors of particles from the primary interaction are produced by such programs as DYMU3 [48] and KORALZ [49], which encapsulate Standard Model expectations of the characteristics of the possible processes. The fragmentation of quarks into jets of particles is controlled by the LUND [50] or EURODEC [51] packages.

The aim of DELSIM is to produce raw data output that closely matches the real data, indicating that detector effects arising from interactions of particles as they travel through DELPHI are well understood. Raw data from DELSIM is passed through the same processing chain as the real data, producing DST tapes for subsequent analysis. Additional information banks containing the **truth tracks**, giving the generated event history, are also provided.

3.11.3 Event tagging

In the writing of the DST tapes by the PXDST package separate output streams for triggers classified as hadronic, leptonic, unknown etc. are provided. It is important that a loose leptonic tag is used, including all events that could possibly be e^+e^-, $\mu^+\mu^-$ or $\tau^+\tau^-$; as re-processings improve data quality due to better alignment and calibration, leading to previously 'poor' leptonics becoming good leptonic candidates.

The starting points for the DELANA tagging are the three criteria [52]:

- **Track trigger (TT):** uses tracks with impact parameter in $R\phi$, r_{imp}, and closest approach in z, z_{imp}, satisfying: $r_{imp} < 8$ cm & $z_{imp} < 50$ cm. The TT makes a loose selection of the number of such tracks and their momenta.
- **Vertex Track trigger (VTT):** is defined in the same way as the TT but with tighter impact parameter requirements: $r_{imp} < 6$ cm & $z_{imp} < 10$ cm.
- **Calorimeter trigger (CT):** requires that the sum of the energy deposits in the HPC, $\Sigma\, E_{HPC\text{-}TE} > 5$ GeV **OR** that there is ≥ 1 TE in the EMF with E > 4.0 GeV.

The DELANA tagging logic is shown in figure 3.13; the right-hand branch ensures that e^+e^- with no reconstructed tracks are saved and the left-hand branch makes the division into hadronic and leptonic tagged events.

Further tagging code provided by DELPHI's physics Teams [53] aims to save events that do not pass DELANA tagging. The $\mu^+\mu^-$ analysis team tagging code includes a simple track multiplicity, N_c, tag:

$$(1 \leq N_c \leq 6) \cdot \text{and} \cdot (N_c[p > 5\,\text{GeV} \cdot \text{and} \cdot r_{imp} < 8\,\text{cm} \cdot \text{and} \cdot z_{imp} < 10\,\text{cm}] \geq 1), \quad (3.7)$$

in addition to code designed to detect $\mu^+\mu^-$ tracks in the dead regions between the end plate sectors of the TPC and in the forward region where track reconstruction efficiency can be low. Tracks in the six TPC ϕ cracks are identified by looking for aligned hits in back-to-back OD planks behind the cracks. Recovery of un-reconstructed forward muon tracks are attempted by combination of data from forward tracking, calorimeter and muon detectors. An alignment of muon signatures from some combinations of EMF, HAC and MUF is taken as a candidate 'muon'.

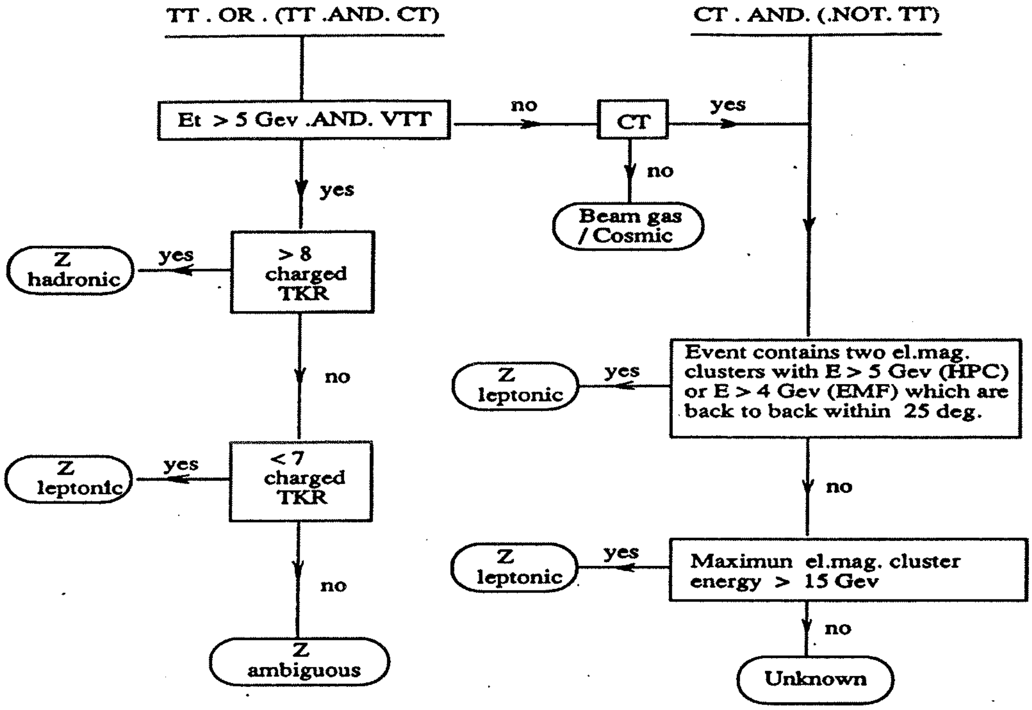

Figure 3.13: Classification of events tagged by DELANA.

Any TK or TE in FCA, FCB and TPC is taken as a candidate 'track'. Events are saved if there is a back-to-back combination of either 'muon' or 'track' signals.

The DST leptonic data for the years 1990,1991 and 1992 constitutes some 72 IBM cassettes stored in the central data division vaults at CERN.

3.12 Leptonic microdst production

As a further step in the data reduction chain, in order to minimize processing time, a greatly reduced microdst was produced; comprising some 5 IBM cassettes. The microdst provides a concise (on average 300 data words per event) summary of event characteristics essential for this analysis. Microdst content and structure are shown in Appendix C.

The microdst is written for events from the DST leptonic data set with the additional requirement that events have a charged multiplicity, N_c, such that: $1 \leq N_c \leq 8$. This includes all events that could pass $\mu^+\mu^-$ identification cuts.

Chapter 4

Muon-pair events with detected photons

This chapter aims to compare the characteristics of radiative muon-pair events[1] with theoretical predictions, as represented by the DYMU3 generator. The selection of $e^+e^- \to \mu^+\mu^-$ final state events, without bias against radiative events, is described. Backgrounds and efficiencies of the muon-pair selection are briefly described. This is followed by a discussion of photon detection and the correction factors necessary in order to compare observations, in the form of energy and angular spectra of produced photons, with the DYMU3 predictions.

The aim of this analysis is not to obtain high precision muon-pair cross sections and asymmetries at the LEP energy points, but rather to investigate radiative muon-pair events. As a result, a precise determination of year-by-year efficiencies and backgrounds within the $\mu^+\mu^-$ sample for use as correction factors, is of lesser importance in this analysis than in muon-pair cross section and asymmetry measurements. It is, however, important to check for (and correct for) any large differences in the efficiencies determined from data and from simulation. This is of particular importance with regard to the cross section determination of chapter 5, which relies upon an accurate simulation of detector performance.

In this chapter, the determination of photon detection efficiencies and handling of the calorimetric photon energy reconstruction are the dominant issues, leading to the largest systematic uncertainties in the measurements of photon energy and angular spectra. From simulation, only some 7% of generated muon-pairs passing

---

[1] Muon-pair events with photons of significant energy are termed radiative muon-pair events.

the event selection of table 4.1 have a total photon energy of greater than 5 GeV. Thus the number of events available to radiative muon-pair studies is very much reduced compared to muon-pair studies, particularly when the energy and angular spectra are studied.

4.1 Muon-pair selection overview

4.1.1 Data sample and run selection

The analysed sample comes from all data taken by DELPHI in the LEP running periods of 1990 to 1992, corresponding to an integrated luminosity of 40.5 pb^{-1} or $\sim 1.1 \cdot 10^6$ Z^0 decays into hadrons and charged leptons.

The status of the detector components of DELPHI are recorded on a run-by-run basis, indicating operating performance as a percentage of nominal efficiency. Only runs where the operation of the HPC and EMF calorimeters is in excess of 90% are used.

4.1.2 Characteristics of $\mu^+\mu^-$ events

The energy spectrum of radiative photons produced in $\mu^+\mu^-$ events is strongly peaked at low energies with the low energy photons generally produced at small angles to the muons. It is impossible to make a selection of muon-pairs that excludes photons in the initial or final states; although clearly requiring muon momenta close to the beam energy and a very small acolinearity enables the photons to be removed to a large degree. The acolinearity angle θ_{acol} of two particles with 3-momenta at closest approach to the beamspot position (approximating to the momenta at the interaction point), $\vec{p}_1$ and $\vec{p}_2$, is defined as:

$$\theta_{acol} = \cos^{-1}\left[\frac{\vec{p}_1 \cdot (-\vec{p}_2)}{|\vec{p}_1||\vec{p}_2|}\right] \tag{4.1}$$

Muon-pair events, with low energy photons only, are expected to have two oppositely charged and almost back-to-back tracks, each of energy close to the beam energy, $E_b \sim 45$ GeV. The radius of curvature ρ of such charged tracks in DELPHI's 1.2 T magnetic field is given by: $\rho[\mathrm{m}] = \mathrm{p}\,[\mathrm{GeV}] \sin\theta / 0.3\mathrm{B}\,[\mathrm{T}]$, leading to $\rho \approx 125$ m for polar angle $\theta = 90°$. These high momentum muons are minimum ionizing and thus highly penetrating, travelling throughout the detector with only small angle scattering. Typical energy deposits in the HPC and FEMC are 0.2 GeV and 0.6 GeV respectively.

4.1.3 Sources of background

Possible sources of background events within a $\mu^+\mu^-$ sample are:

$e^+e^- \to \tau^+\tau^-$: In tau-pair events the tau leptons decay[2] into one (86%) or three (14%) charged particles (mostly $\pi^\pm$, with $\mu^\pm$ & $e^\pm$), a tau neutrino and possibly one or more other neutral particles [12]. The similarity of topology to $\mu^+\mu^-$ events and the fact that pions can be mis-identified as muons make this one of the largest backgrounds. Cutting on the momentum of the charged particles provides the principal control over this background, as charged particles in $\tau^+\tau^-$ events generally have a lower momentum that those in $\mu^+\mu^-$ events due to the energy taken by the neutral particle products. This is demonstrated by the momentum distribution plots of figure 4.1. In addition the muon identification cuts on energy deposits and layers hit in the HCAL are chosen to reject pions from $\tau^+\tau^-$ events.

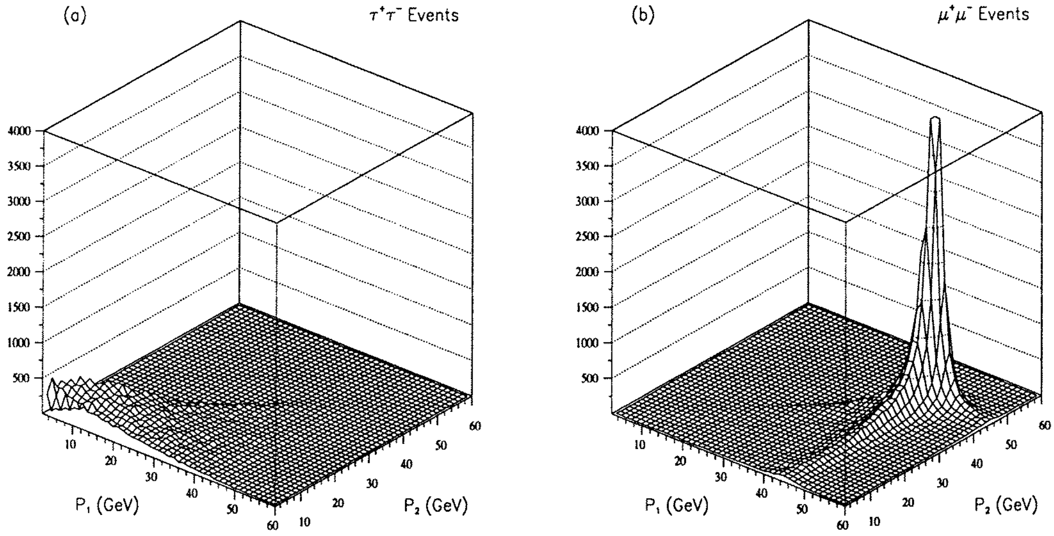

Figure 4.1: 2d-momentum distributions (p1,p2) of the two highest momentum charged tracks (p1>p2) for roughly equal numbers of simulated (a) tau-pair and (b) muon-pair events.

$e^+e^- \to e^+e^-$: These Bhabha events have the same topology as $\mu^+\mu^-$ events, in general the produced electron and positron are stopped in the electromagnetic calorimeter depositing ~ 45 GeV. If there is an identification failure in the

---

[2] The τ lifetime is ~ 300 fs [54], corresponding to a decay length for 45 GeV τ's of order 2 mm.

electromagnetic calorimeters (perhaps due to a gap or dead region) these events may mimic $\mu^+\mu^-$ events.

Cosmic ray muons: Primary cosmic rays (mainly protons) incident from all directions, give rise to secondaries in nuclear interactions in the upper atmosphere. The cosmic ray muon secondaries are penetrating enough to reach ground level, and indeed to penetrate 100m below ground to travel through the DELPHI detector. If a cosmic ray muon passes close to the interaction region at a time within the active trigger gate, close to the beam crossover time (BCO), then it can mimic a $\mu^+\mu^-$ event.

2-photon reactions: $e^+e^- \to e^+e^-f\bar{f}$, $f = e, \tau$; are non-resonant processes arising from the interaction of virtual photons accompanying the electron and positron beams to give a four-fermion final state, as illustrated in figure 4.2. In general the primary e$^+$e$^-$ are lost down the beampipe leading to an observable final state of a low momentum fermion pair. The low momentum is due to the nature of the bremsstrahlung spectrum ($\sim$ 1/E$_\gamma$) of the radiated photons resulting in little available energy for the $f\bar{f}$.

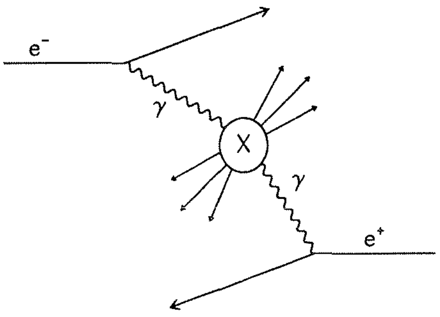

Figure 4.2: Two-photon process forming the final state X, a $f\bar{f}$ pair.

Beam-gas & beam-wall interactions Such 'machine' backgrounds lead to low energy tracks and energy deposits not consistent with particles from the interaction region.

4.2 Selection criteria

The selection briefly described here is based on that of [55], in which a full discussion of the choice of cuts is given. Events were classified as 'standard' muon-pairs if they satisfied the selection criteria outlined in Table 4.1.

C1	The number of charged particles N_c satisfies $2 \leq N_c \leq 5$.
C2	The two highest momentum charged particles must have $p > 20$ GeV
C3	for the two highest momentum charged particles, the projection of the impact parameters in the plane transverse to the beam direction, r_{imp}, should be smaller than 1.5 cm, the longitudinal distances, $z_{imp}{}^{(1)}$ and $z_{imp}{}^{(2)}$ between the points of closest approach and the beamspot should be smaller than 4.5 cm, and $\left|z_{imp}{}^{(1)} - z_{imp}{}^{(2)}\right| < 4.0$ cm. For particles where the microvertex detector participated in the track fit the r_{imp} impact parameter cut is reduced to 0.4 cm.
C4	the two highest momentum charged particles are required to be in the polar angle range $20° < \theta < 160°$.
MU	the two highest momentum charged particles are required to be identified as muons using either the muon chambers, the hadron calorimeter, or the electromagnetic calorimeters, as described in section 4.3.

Table 4.1: Track cuts for the $\mu^+\mu^-$ analysis. **C1-C4** and **MU** are the cuts used to select $\mu^+\mu^-$ events, in the 'standard' selection.

The motivation for the choice of cuts **C1-4** is given below.

C1 More than two charged tracks arise in $\mu^+\mu^-$ events due to the conversion of radiated photons to low momentum e^+e^- pairs. Requiring ≤ 5 avoids excessive contamination by $\tau^+\tau^-$ and hadronic events. Simulation studies show that the loss of $\mu^+\mu^-$ events resulting from this cut is $0.112 \pm 0.009\%$ within this 'standard' muon selection and $0.117 \pm 0.009\%$ within the 'soft' muon selection (defined below). No reclaim of events where only one muon is reconstructed is attempted.

C2 This momentum cut reduces backgrounds from all sources listed above.

C3 Cosmic ray muon 'event' backgrounds are greatly reduced by this vertex constraining cut. Justification for the tighter cut applied when the VD participates in the track fit can be seen in figure 4.3. This shows the dramatic improvement in impact parameter resolution when VD hits are used in the track fit.

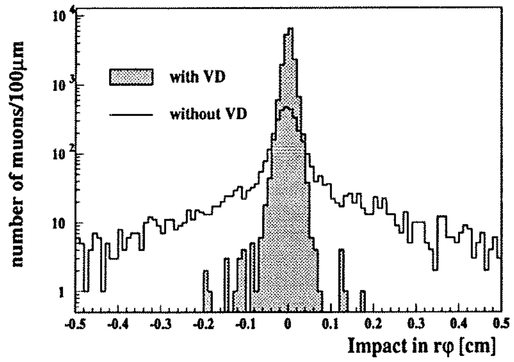

Figure 4.3: Impact parameter distributions with and without participation of the VD in the track fit, for $\mu^+\mu^-$ events.

C4 This polar angle range excludes the very forward region where the track reconstruction efficiency is low and the momentum resolution is poor.

The 'standard' set of cuts **C1-C4** and **MU** is modified to 'hard' and 'soft' variations by changing the momentum cut **C2** to **C2H** and **C2S** respectively, as defined in table 4.2.

C2H	The two highest momentum charged particles must have p > 40 GeV, and have acolinearity angle $\theta_{acol}<1°$.
C2S	The two highest momentum charged particles must have momenta $p_1 > 12$ and $p_2 > 7$ GeV

Table 4.2: Variations to the 'standard' cut **C2** that form the 'hard' and 'soft' selections.

4.3 Muon identification

A high energy muon is expected to pass through the electromagnetic and hadron calorimeters with small angle scattering only, leaving small energy deposits consistent with ionization energy loss, and to produce hits in the muon chambers.

The muon identification cut **MU** demands that the two highest momentum charged tracks are both identified as muons, by satisfying at least one of the following criteria:

MU1: Energy associated with the track in the HPC or FEMC, E_{em} is in the range, $0.01 < E_{em} < 1$ GeV.

MU2: Number of muon chamber hits $N_{mux} \geq 1$.

MU3: HCAL identification criteria are given in terms of the HCAL energy associated to the track E_h and the polar angle θ. The θ dependence of E_h is accounted for by dealing with a corrected energy $E_h \sin^2\theta$ in the angular region ($50° < \theta < 130°$).

- $0.01 < E_h \sin^2\theta < 15$ GeV {10 GeV in 1990} ($50° < \theta < 130°$)
- $0.01 < E_h < 20$ GeV {15 GeV in 1990} ($\theta < 50°$, $\theta > 130°$)

In addition the 4-bit hit pattern word, where bits 0-3 are set when layers 1-4 are hit, is required to be ≥ 4, thus requiring that at least one of the outer two layers are hit.

The event displayed in figure 4.4 is a radiative muon-pair in which both muons are identified by all 3 criteria: **MU1-3**. A brief summary of the techniques and findings that lead to this choice of cuts is given below; for further details see pages 76-79 of [55]. These cut choices are based on studies of detector response to samples selected by use of data from other detectors. For example, the HCAL and HPC/FEMC response to muons was obtained for a sample of 'good' muons selected by hard momentum and acolinearity cuts and 1 or more hits in the muon chambers. Muons leave on average 5 GeV in the HCAL and less than 1 GeV in HPC/FEMC and one or more hits in the muon chambers. Electrons from $e^+e^- \rightarrow e^+e^-$ events generally deposit more than 40 GeV in the electromagnetic calorimeters, with no deposits in HCAL or hits in the muon chambers.

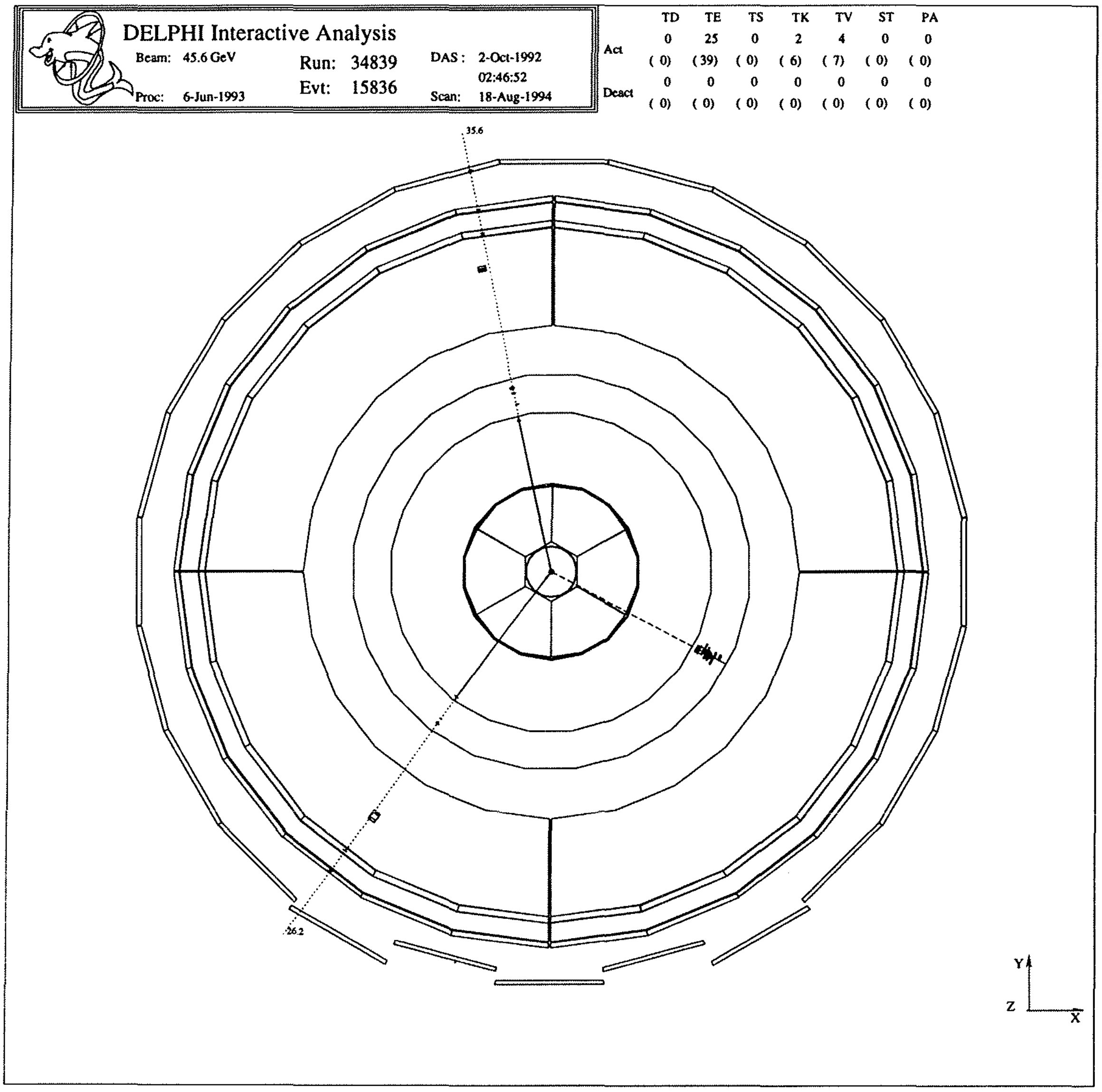

Figure 4.4: Display of a $\mu^+\mu^-\gamma$ event in the x-y plane, where the photon is reconstructed in the HPC, E_γ(meas)= 31.1 GeV. The 1-photon kinematic fit using muon track information alone, predicts a photon energy of 30.4 GeV with a momentum vector at an angle of 1.3° to the seen photon vector.

The HCAL data cut, **MU3**, attempts to reject pions while not loosing too many muons. A sample of events containing isolated pions was obtained from $\tau^+\tau^-$ 1-prong versus 3-prong decays (the 1-prong is a pion, muon or electron in proportions 58:21:21 respectively [12]). Requiring the 1-prong to fail cuts **MU1** & **MU2** yields a sample of events where the track with the largest isolation angle is predominantly a pion. Comparison of the HCAL response to pions and muons led to the choice of cut **MU3**.

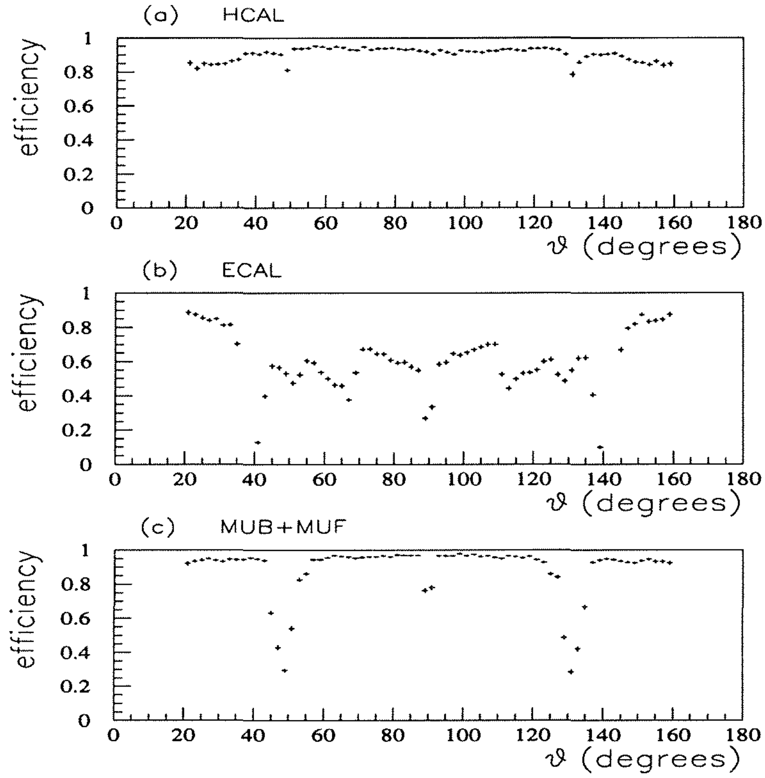

Figure 4.5: Muon identification efficiency of selections **MU1-3** from data sample of 'standard' $\mu^+\mu^-$ from 1990,1991 and 1992; using (a) HCAL, (b) ECAL and (c) MUB & MUF data.

Muon identification efficiencies of the selections **MUi** were obtained from the fraction of events selected by **MUj** or **MUk** that also fulfil **MUi** (where the indices i,j,k are any permutation of 1,2,3). The efficiencies are given in figure 4.5. The structure in the efficiency in the ECAL shows the segmentation in z of the HPC modules, with increased MIP efficiency as the track length increases from the $\theta = 90°$ minimum. These efficiencies combine the data from years 1990 to 1992; prior to the HPC voltage decrease in 1991, the ECAL muon identification efficiency was significantly higher at ~ 80% for the full θ range, excluding the $\theta \sim 90^\circ$ region. Combining these lone detector muon selection efficiencies (see figure 4.6) to give the

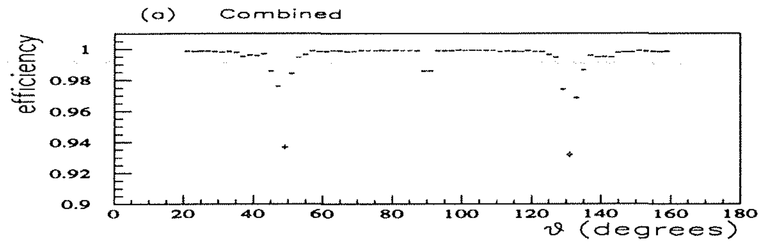

Figure 4.6: Combined single arm muon identification efficiency ϵ_{comb}, obtained from the years 1990,1991 and 1992.

efficiency of an 'OR' of any of them, gives the combined single arm muon efficiency ϵ_{comb} as:

$$1 - \epsilon_{\text{comb}} = (1 - \epsilon_{\text{hcal}})(1 - \epsilon_{\text{ecal}})(1 - \epsilon_{\text{mux}}). \tag{4.2}$$

The same efficiency determination technique was applied to simulation. Excellent agreement was found between the combined muon identification efficiencies from data and from simulation over most of the polar angle range, with single arm muon identification efficiencies in excess of 99.8%. The discrepancies in the regions of poorer coverage, at $\theta \sim 90^\circ$ and in the regions between the MUB and MUF, were all less than 1%.

4.4 Backgrounds

Cosmic background evaluation from data

This background was estimated from the data, by using a sample selected using all cuts apart from the vertex cut **C3**. Looking at the distribution of r_{imp}vs.z_{imp} of the two muon candidates, shows a highly populated central interaction region, with a uniform population away from the interaction region arising due to cosmics mimicking $\mu^+\mu^-$; as seen in figure 4.7. Counting the number of events with both tracks contained within the chosen (uniformly populated) area in the $r_{\text{imp}}z_{\text{imp}}$ plane, excluding the interaction region, enables the cosmic background per unit area of

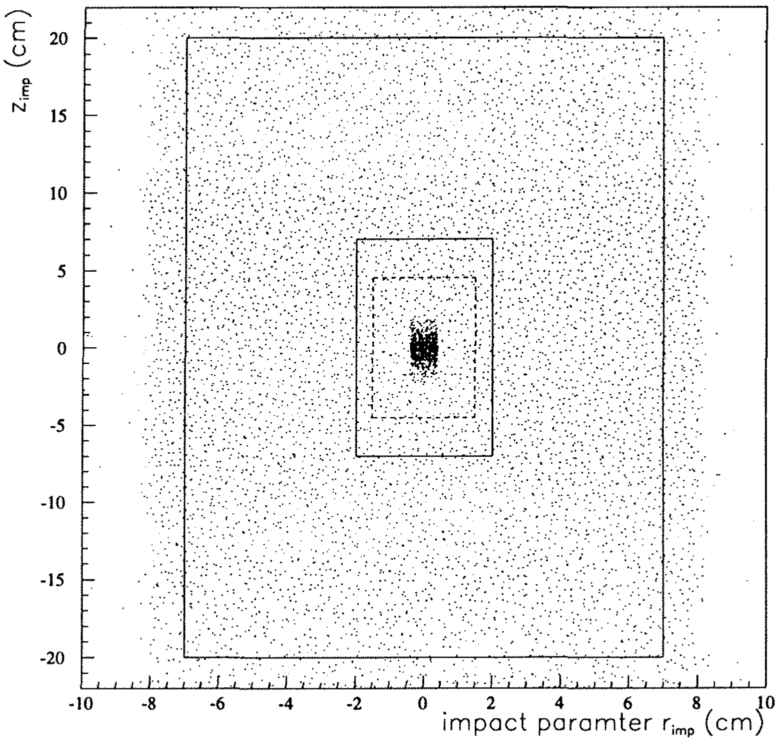

Figure 4.7: Impact parameter distribution for events selected from the year 1992, by the 'standard' muon pair selection excluding the vertex cut **C2**. The region between the solid boxes is used to evaluate the cosmic background. The inner dashed box represents the looser vertex cut, used when VD hits or beamspot are not available.

vertex selection cut, $\mathrm{D^{cosm}}$, to be evaluated. Thus the number of cosmic ray muon events in the muon sample, $\mathrm{N^{cosm}}$, is determined by:

$$\mathrm{N^{cosm}} = (\mathrm{f_{VD}A_{VD}} + \mathrm{f_{\overline{VD}}A_{\overline{VD}}})\,\mathrm{D^{cosm}}, \tag{4.3}$$

where $\mathrm{A_{VD}} = 4 \cdot 0.5 \cdot 4.5\ \mathrm{cm^2}$, $\mathrm{A_{\overline{VD}}} = 4 \cdot 1.5 \cdot 4.5\ \mathrm{cm^2}$ and $\mathrm{f_{VD}}$ & $\mathrm{f_{\overline{VD}}}$ are the fractions of selected events for which the tighter and looser impact parameter cuts are applied. The tighter cut is used when VD hits participated in the track fit and a reliable beamspot position is available (overall this is the case for 68% of events in the 'standard' selection). Results obtained are given in table 4.3, the dramatic difference between backgrounds in 1990 and those in 1991&1992 reflects the improvement in impact parameter resolution with the microvertex detector upgrade of 1991.

Year	Cosmic background in $\mu^+\mu^-$ samples 'standard' (%)	 'soft' (%)
1990	2.58 ± 0.23	4.05 ± 0.27
1991	0.54 ± 0.07	0.85 ± 0.09
1992	0.61 ± 0.04	0.98 ± 0.05
'90-'92	0.75 ± 0.04	1.18 ± 0.05

Table 4.3: Percentage of the 'standard' and 'soft' muon pair samples estimated to be cosmic muon 'events'.

Other backgrounds from simulation studies

The principal technique used to determine the composition of the muon-pair samples is the application of the same selections to simulated data of $\tau^+\tau^-$,e^+e^- and 2-photon interaction final states. Table 4.4 summarizes the results of such studies[3]. As the cosmic background is obtained from the data sample (containing all the other backgrounds), the number of cosmics N_o^{cosm}, within the nominal sample presented in the table, is obtained from the total numbers of non-cosmics, $\overline{N}_o^{cosm}$, by the relation:

$$N_o^{cosm} = \overline{N}_o^{cosm} \left(\frac{f^{cosm}}{1 - f^{cosm}} \right), \tag{4.4}$$

where f^{cosm} is the cosmic fraction given in table 4.3.

4.5 Efficiencies

Failure to reconstruct tracks is the main cause of loss of muon-pair events. This occurs primarily at the TPC sector boundaries, where the readout pads are segmented (see figure 3.6), and at the TPC z=0 centre plane.

TPC sector boundaries, ϕ 'cracks'

The sector boundaries are centred at ϕ values where $\mathrm{mod}(\phi, 60°) = 30°$. Thus folded ϕ distributions are used to illustrate the losses. Figure 4.8 compares the losses due to the ϕ cracks from data and simulation. The ϕ of the two muon candidates

---

[3] The intention of this section is to provide an indication of the performance of the selections rather than to obtain year by year correction factors to apply to the observed numbers of events. Thus Monte Carlo simulations from various years are used in the table.

		Numbers of events		
Interaction	Luminosity (pb^{-1})	generated	'soft' $\mu^+\mu^-$	'standard' $\mu^+\mu^-$
$\mu^+\mu^-$('91)	29.4	43791	36943	36429
$\tau^+\tau^-$('92)	61.9	92882	4057	915
e$^+$e$^-$('92)	59.9	56361	10	7
$e^+e^-\mu^+\mu^-$	53.1	67824	206	6
$e^+e^-\tau^+\tau^-$	37.2	9984	2	0

Sample composition after scaling

	40.5			(%)		(%)
$\mu^+\mu^-$		60324.3	50890.9	93.04	50182.8	98.06
$\tau^+\tau^-$		60770.9	2654.4	4.85	598.7	1.17
e$^+$e$^-$		38107.2	6.8	0.01	4.7	0.01
$e^+e^-\mu^+\mu^-$		51730.2	157.1	0.29	4.6	0.01
$e^+e^-\tau^+\tau^-$		10869.7	2.2	0.00	0.0	0.00
Non-cosmics			53711.4		50790.8	
Cosmics			641.4	1.18	383.8	0.75
Total			54352.8		51174.6	

Table 4.4: Estimated compositions of the 'soft' and 'standard' muon pair samples. In the lower section the numbers of events are scaled to those expected for a nominal luminosity of 40.5 pb^{-1}, for ease of comparison.

in all selected events in data and Monte Carlo contribute to the plots. Prior to comparison the data were corrected for the principal backgrounds of $\tau^+\tau^-$ and cosmic ray muons. The fraction of tracks lost, $1-\epsilon_\phi$, is obtained using the folded ϕ distributions and the relation:

$$1-\epsilon_\phi = \frac{\mathrm{N}_\phi^{\mathrm{loss}}}{\mathrm{N}_\phi^{\mathrm{loss}}+\mathrm{N}^{\mathrm{tot}}}, \tag{4.5}$$

where $\mathrm{N}_\phi^{\mathrm{loss}} = \mathrm{N}_\phi^{\mathrm{pred}} - \mathrm{N}_\phi^{\mathrm{obs}}$; $\mathrm{N}_\phi^{\mathrm{pred}}(\mathrm{N}_\phi^{\mathrm{obs}})$ is the predicted(observed) number of tracks in the $\phi = 30\pm3°$ 'hole' region and $\mathrm{N}^{\mathrm{tot}}$ is the total number of tracks. The prediction is made by fitting horizontal lines to the regions outside the 'hole'.

TPC centre plane, θ 'crack'

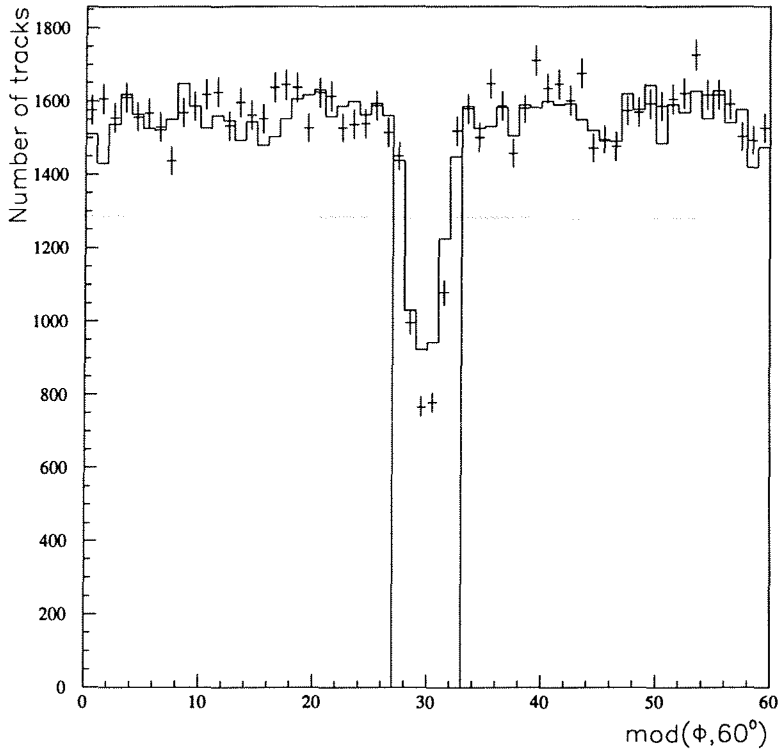

Figure 4.8: The TPC sector boundary losses are demonstrated by mod(ϕ,60°) distributions for muon candidates in selected $\mu^+\mu^-$ events from data (crosses) and Monte carlo (solid line). The vertical lines denote the $30 \pm 3°$ region treated as the 'hole'.

Losses due to the TPC centre plane, $\theta \sim 90°$, for data and simulation can be seen in figure 4.9. A similar approach to that for the ϕ cracks is used to evaluate the fraction of tracks lost, $1 - \epsilon_\theta$, with an analogous relation to equation 4.5. As $|\cos\theta|$ is used, it is valid to obtain $\mathrm{N}_\theta^{\mathrm{pred}}$ in the 'hole' region by extrapolation of a $\kappa(1 + \cos^2\theta)$ function. Assuming the distribution follows this functional form allows the number of events in a range of $\cos\theta(= \mathrm{x})$, $\mathrm{N}_{\mathrm{x_0x_1}}$, to be obtained by integration:

$$\mathrm{N}_{\mathrm{x_0x_1}} = \frac{\kappa}{\Delta\mathrm{x}} \int_{\mathrm{x_0}}^{\mathrm{x_1}} (1 + \mathrm{x}^2)\,\mathrm{dx}, \tag{4.6}$$

where Δx is the bin width used and κ is a constant obtained by fitting in a 'good' region of θ.

The TPC ϕ and θ inefficiencies are collected in table 4.5, from both data and simulation. The '92 simulation used corresponds to the bulk of the data set. There is a $\sim 0.5\%$ difference in the ϕ inefficiencies observed from the data and from sim-

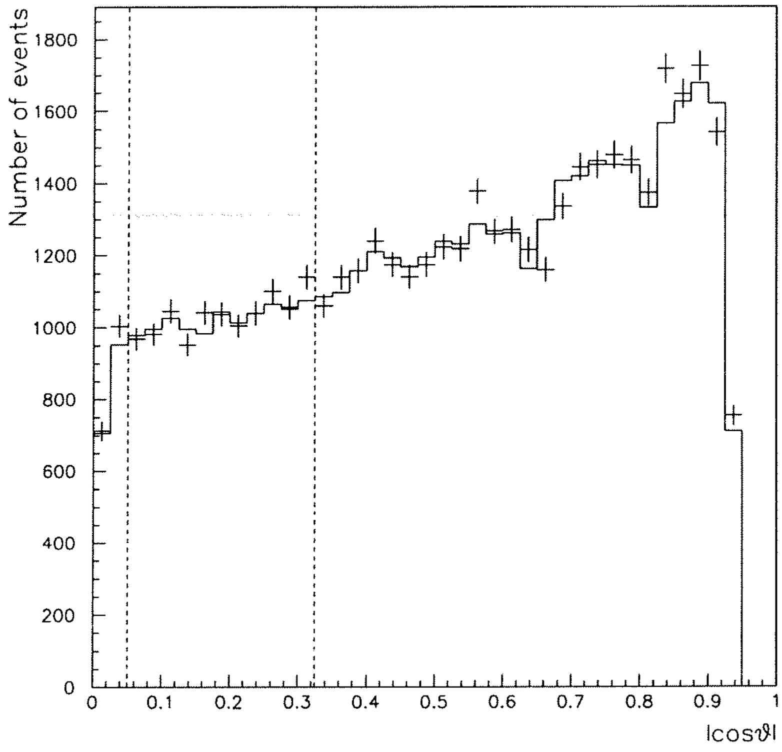

Figure 4.9: The TPC centre plane losses are demonstrated by |cosθ| distributions for muon candidates in selected $\mu^+\mu^-$ events, from data (crosses) and Monte carlo (solid line). The vertical dashed lines denote the 'fit' region.

	TPC inefficiencies	
	data '90-'92 (%)	simulation ('92) (%)
$1-\epsilon_\phi$	3.03 ± 0.06	2.49 ± 0.05
$1-\epsilon_\theta$	0.61 ± 0.04	0.61 ± 0.04

Table 4.5: TPC θ and ϕ inefficiencies from data and simulation

ulation, requiring a correction factor to be applied to simulation distributions prior to comparison with data; as discussed below.

TPC live space inefficiencies

Remaining live space inefficiencies in the TPC are obtained from the data by selecting events which include a high momentum muon candidate, and then looking for another track with acolinearity to the first of less than 10°. The event was

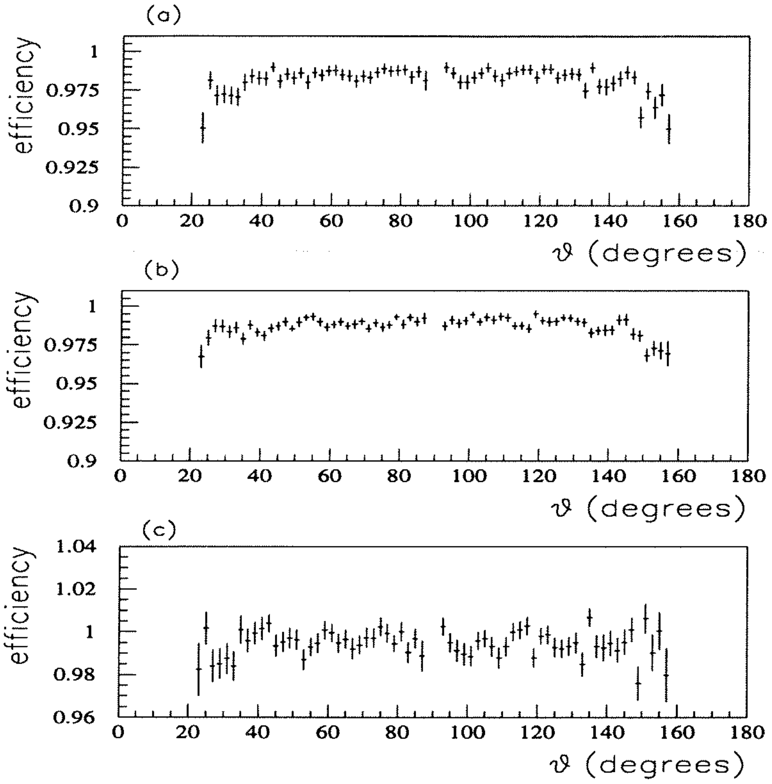

Figure 4.10: (a) raw single track reconstruction efficiency (excluding the TPC θ and ϕ cracks) from data. (b) efficiency of the method, obtained from the simulation raw efficiency divided by the 'true' reconstruction efficiency, obtained using the truth information. (c) track reconstruction efficiency, from division of (a) by (b).

required to have $1 \leq \mathrm{N_c} \leq 5$, with a track:

- $40 < \mathrm{p} < 56$ GeV/c
- $|\mathrm{mod}(\phi, 60^\circ) - 30^\circ| > 10^\circ$, removing effects due to the TPC sector boundaries.
- $22^\circ < \theta < 87^\circ, 92^\circ < \theta < 158^\circ$, removing the $\theta \sim 90^\circ$ crack.
- track impact parameters: $\mathrm{r_{imp}} < 0.5$ cm, $|\mathrm{z_{imp}}| < 3$ cm
- Muon selection, an 'OR' of **MU1-3**, as specified in section 4.3.

The fraction of events with such tracks which also have a second track close to the expected back-to-back position (with θ_{acol}<10°) provides a 'raw' efficiency estimate. The second track is required to have:

- $\mathrm{p} > 5$ GeV/c,

- $r_{imp} < 1.5$ cm, $|z_{imp}| < 4.5$ cm.

This 'raw' efficiency is given in figure 4.10(a). The 'raw' efficiencies are viewed to factorise as follows, for data (DA) and simulation (MC):

$$\begin{aligned} \epsilon_{raw}^{MC} &= \epsilon_{true}^{MC} \cdot \epsilon_{meth}^{MC} \\ \epsilon_{raw}^{DA} &= \epsilon_{true}^{DA} \cdot \epsilon_{meth}^{DA}, \end{aligned} \tag{4.7}$$

where the ϵ_{meth} accounts for the effects of the momentum and acolinearity requirements. Figure 4.10(b) is ϵ_{meth}^{MC}, obtained from ϵ_{raw}^{MC} and the close to unity ϵ_{true}^{MC}; which was obtained from the fraction of simulated truth tracks which are reconstructed. Figure 4.10(c) from the division of (a) by (b) provides ϵ_{true}^{DA}, assuming that $\epsilon_{meth}^{MC} = \epsilon_{meth}^{DA}$.

Trigger efficiency

Year	$\mu^+\mu^-$ Trigger efficiency (%)	reference
1990	98.1 ± 0.3 (96.5 ± 0.3)	[27]
1991	99.90 ± 0.10	[28]
1992	99.87 ± 0.08	[29]

Table 4.6: $\mu^+\mu^-$ trigger efficiencies. The 1991 and 1992 numbers are for the polar angle range 20-160°. In 1990 some variation with θ occurred; the first number is for the barrel region and the second number in brackets is the average over the 20-160°range.

The trigger decision is made on the basis of many components loosely grouped into classes which trigger on tracks, muon signals, electromagnetic energy deposits and hadronic energy deposits. The trigger is designed to have high redundancy over the full θ range, to enable accurate determination of trigger efficiencies. At the simplest level, a comparison of the response of independent triggers to a sample of muon-pair events enables the independent efficiencies to be determined and then combined to give an efficiency of the trigger system (the muon identification efficiency determination in section 4.3, provides a simple example of the same principals).

In practice the trigger decision function is complex and correlations between the trigger components need to be taken into account [56]. The results of such studies are given in table 4.6.

Data and simulation comparison

The above efficiency determinations have shown good agreement between data and simulation, the largest discrepancy occurring in the modelling of the TPC ϕ cracks. Thus in order to make a comparison of data and simulation within the 'standard' muon-pair selection it is necessary to correct the data for the backgrounds summarized in table 4.4, the trigger efficiency and the TPC ϕ discrepancy. Within the 'standard' muon-pair selection, loss of a high momentum track ($p > 20$ GeV) will result in loss of the event. Thus the ratio of ϕ efficiencies from data and simulation: $\epsilon_\phi^{\mathrm{data}}/\epsilon_\phi^{\mathrm{simulation}} = 0.994 \pm 0.001$ is used to correct simulation distributions before comparison with data.

4.6 Photon detection

The electromagnetic calorimeters are described in 3.7. Photons are expected to lose all their energy as an electromagnetic shower within the 18(20) X_0 of the HPC(EMF). Complications arise in photon reconstruction due to the considerable amount of material in front of the calorimeters and due to calorimeter noise. Complicated pattern recognition algorithms are used [57], that require energy deposits in several layers to form energy clusters. In addition to providing the energies and locations of clusters the HPC reconstruction software provides the shower direction angles, θ_{sh} and ϕ_{sh}.

In this section the simple techniques used to remove noise and to cluster energy deposits are described.

4.6.1 Calorimeter noise removal

Figure 4.11 shows the positions of reconstructed showers in the EMF and HPC; the modularity of the calorimeters is apparent together with indications of noisy regions. Data from these noisy regions, and others that become visible after removing the most noisy areas, were removed by application of cuts on the coordinates of the energy deposits. In addition it was required that the clusters point back to the origin: $|\theta_{\mathrm{sh}} - \theta_{\mathrm{dep}}| < 10°$, where θ_{dep} is the polar angle of the vector from the origin to the start of the shower. This was found to remove some electronic noise

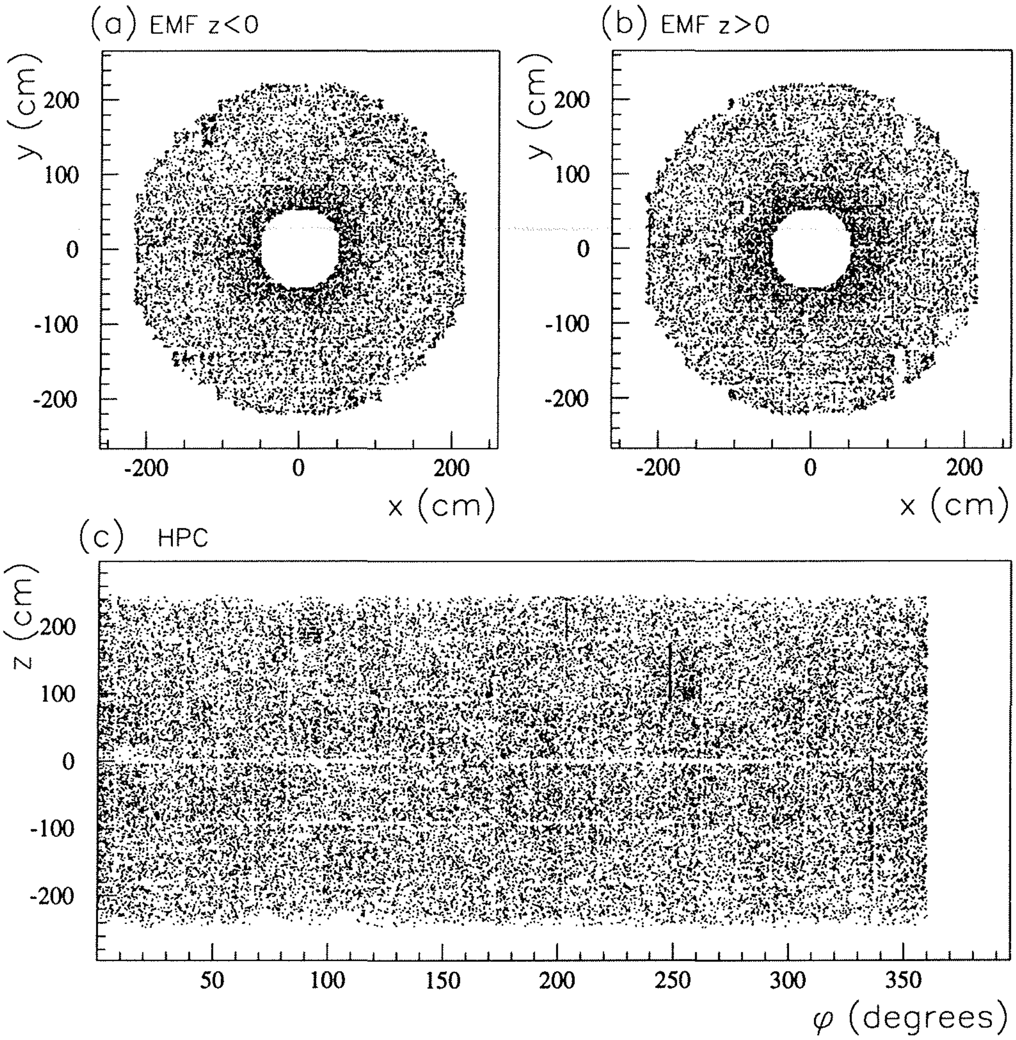

Figure 4.11: Positions of energy deposits in (a) EMF (z<0), (b) EMF (z>0) and HPC; showing detector modularity and noisy areas.

'clusters' present in a few modules, for which $\theta_{\rm sh} \sim 90°$ for all $\theta_{\rm dep}$, as seen in figure 4.12. These noise removal cuts are applied to both data and simulated Monte Carlo samples.

The randomly located noise clusters arising due to the α-particle producing radioactive decay of impurities within the lead converter material and other 'moving' noise sources, are not amenable to these removal techniques. Using the 'hard' muon-pair selection detailed in section 4.2, kinematically restricts photon production to a maximum energy of $\sim$ 8 GeV (obtained from the one photon kinematic fit, described in Appendix D), allowing any high energy noise clusters to be identified. This tech-

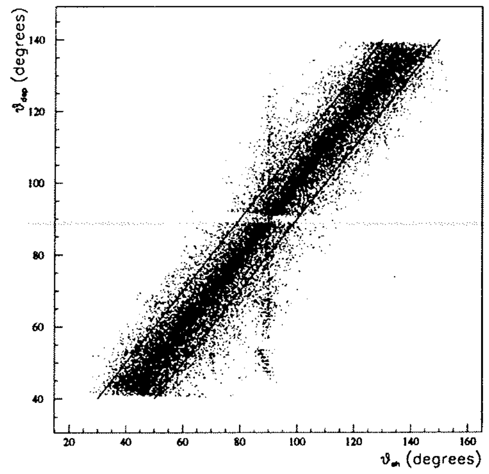

Figure 4.12: Scatter plot of the start of shower position $\theta_{\rm dep}$ and the shower direction $\theta_{\rm sh}$, for HPC clusters of energy >0.25 GeV from leptonic events. The lines indicate the cuts applied.

nique shows that high energy noise (>10 GeV) is not a significant background, at the level of $\sim$ 0.02%.

4.6.2 Clustering procedure

The material in front of the calorimeters (see section 3.7.2) results in some 40% of photons converting before they reach the calorimeters. If the conversion occurs before the TPC, the positrons and electrons produced give rise to tracks and result in further showers in the electromagnetic calorimeters. Such a conversion results in an original single photon being seen as a 'wide shower' of energy deposits in the calorimeters. The energy observed in the calorimeters is less than that of the original photon due to energy loss between the conversion point and the calorimeter.

Due to the clean nature of muon-pair events a simple clustering of energy deposits, ensuring that the MIP deposits due to the muons are not included, is adequate to reconstruct the photon energy E_γ and the smaller of the two angles between the momentum vectors of the muons and the photon, $\alpha_{\mu\gamma}$. This angle is henceforth referred to as the angle between the photon and the muon.

A simple clustering of energy deposits in the electromagnetic calorimeters is performed in which the energies are added together and the momentum of the 'photon' is obtained by adding the momentum vectors of the component deposits as seen from the interaction region. The clustering is performed if the momentum vectors are within 10° of each other. The angle between the nearest muon and the direction to the deposit is required to be greater than 2° for the energy deposit to be included in the clustering; preventing inclusion of energy due to the muons or due to photons collinear with the muons.

4.7 Characteristics of radiative events

Figure 4.13 shows the two dimensional distribution of the E_γ against $\alpha_{\mu\gamma}$, in muon-pair events selected as described in table 4.1. Figure 4.13(a) is of the observed angles and energies, after clustering. For comparison Figure 4.13(b) shows the results of a kinematic fit based on the muon parameters alone. The fit returns photon parameters assuming that only one significant photon is produced (as described in Appendix D). The upper allowable energy of the photon, $E_\gamma^{max} = f_1(\alpha_{\mu\gamma})$, occurs when one of the muon momenta is at the cut value $p_1 = p_c$. The minimum allowed energy, in the angular range 90-180°, $E_\gamma^{min} = f_2(\alpha_{\mu\gamma})$, corresponds to when the muon momenta are equal, $p_1 = p_2$. The functions f_1 & f_2 are derived in Appendix E.

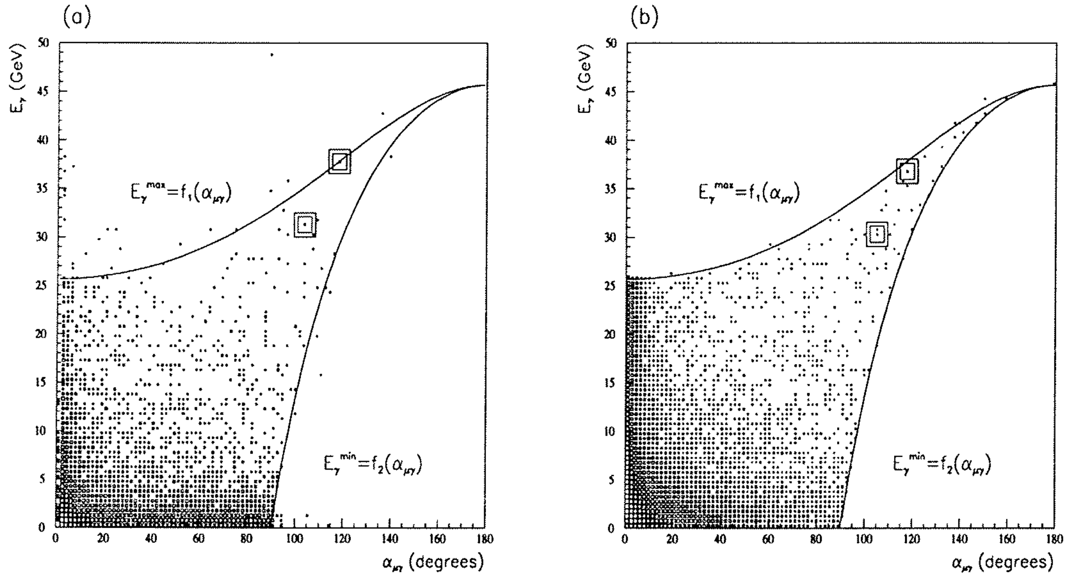

Figure 4.13: Scatter plots of E_γ-$\alpha_{\mu\gamma}$ for muon-pair events from (a) observed quantities and (b) from a one photon kinematic fit using the muon parameters only. The solid lines marked indicate the allowed ranges of E_γ as a function of $\alpha_{\mu\gamma}$, assuming 3-body kinematics.

It is notable that for angles $\alpha_{\mu\gamma}$>90° the available photon energy range is very much reduced leading to a distinct downward 'kink' in the angular spectra at 90°.

The smaller population of figure 4.13(a) compared to (b) at low $\alpha_{\mu\gamma}$ arises due to the requirement that the initial energy deposits must have $\alpha_{\mu\gamma}>2^\circ$ in order to be included in the clusters. Indeed, the requirement that an isolated photon is seen in the calorimeters results in a factor of almost five less events in figure 4.13(a) than in (b). The few events with energies and angles not within the kinematically allowed range are due to invalidity of the one photon assumption and poor energy measurement in the calorimeters.

The two double boxes mark high energy photon events for which 'event displays' are given in figure 4.4 and figure 4.14. Both figures demonstrate muon identification and photon detection as well as providing examples of the kinematic photon reconstruction fit in operation.

4.8 Correcting observed E_γ and $\alpha_{\mu\gamma}$ distributions

Definitions

In order to avoid backgrounds from MIP deposits from the muons and any remaining low energy noise the following energy and isolation requirements are used throughout, defining an *isolated photon cluster*:

- clustered photon energy, $E_\gamma > 2$ GeV,

- angle to nearest muon, $\alpha_{\mu\gamma} > 5^\circ$.

Also to ensure good calorimeter performance, the following definition of a photon being within the *active acceptance* of the calorimeters is used:

- θ_γ in acceptance of HPC or FEMC (see table 3.3)

- Within the HPC acceptance: $|\mathrm{mod}(\phi_\gamma, 15^\circ) - 7.5^\circ| > 1.5^\circ$ and $|\theta_\gamma - 90^\circ| > 2^\circ$, avoiding HPC sector boundaries and z=0 gap.

In the subsequent uses of the above definitions, the cuts are applied to the 'true' (E_γ^{true},$\alpha_{\mu\gamma}^{\mathrm{true}}$,$\theta_\gamma^{\mathrm{true}}$,$\phi_\gamma^{\mathrm{true}}$) or reconstructed ($E_\gamma^{\mathrm{rec}}$,$\alpha_{\mu\gamma}^{\mathrm{rec}}$,$\theta_\gamma^{\mathrm{rec}}$,$\phi_\gamma^{\mathrm{rec}}$) quantities as appropriate.

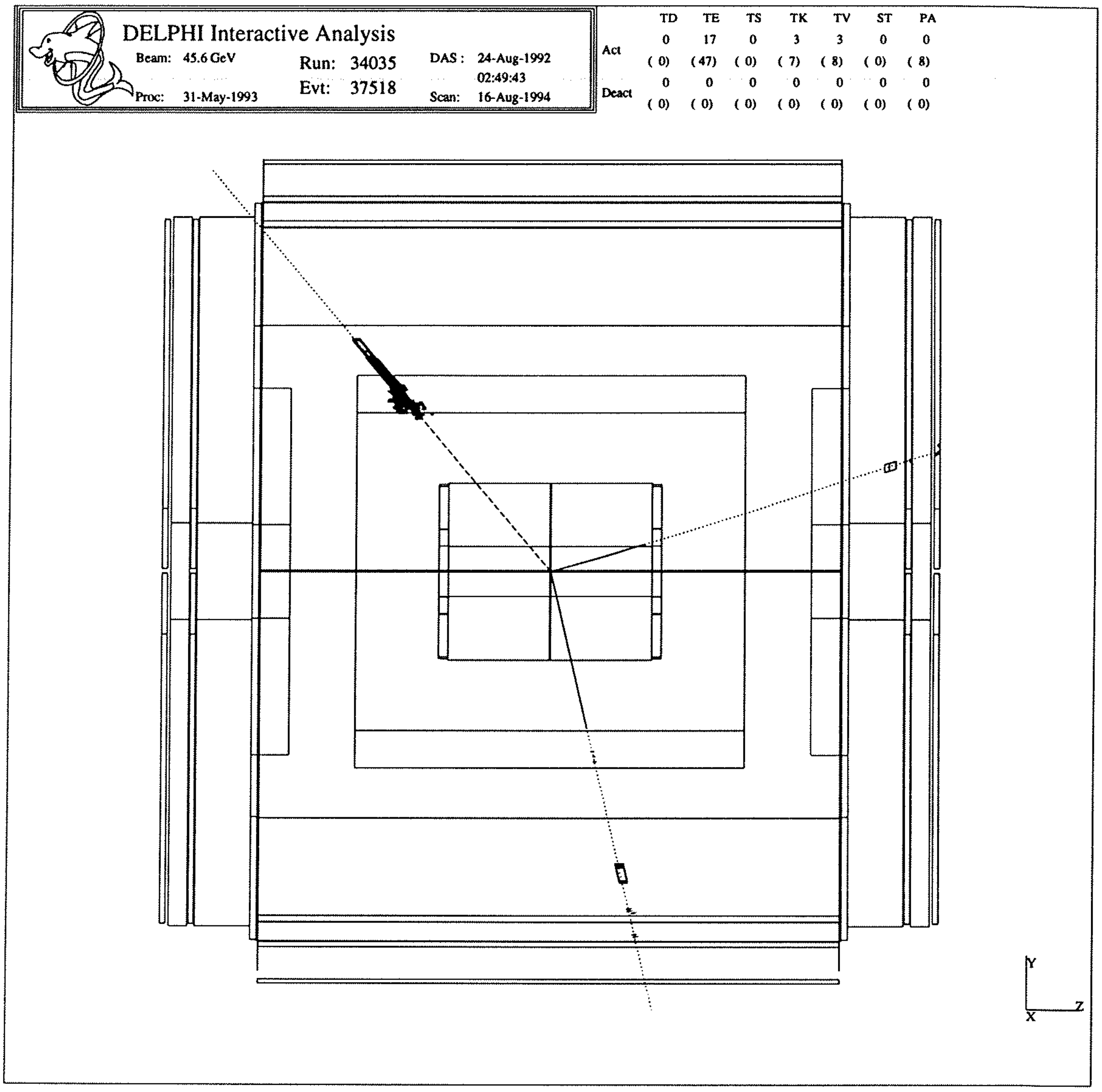

Figure 4.14: Display of a $\mu^+\mu^-\gamma$ event in the y-z plane, where the photon is reconstructed in the HPC, E_γ(meas)= 37.7 GeV. The muons (momenta 21.1 and 30.9 GeV) are reconstructed in the TPC, they both leave a trail in the HCAL consistent with a minimum ionizing particle. One is detected in the HPC and MUB and the other is detected in the MUF. The 1-photon kinematic fit using muon track information alone, predicts a photon energy of 36.8 GeV with a momentum vector at an angle of 1.3° to the seen photon vector.

Backgrounds

Simulation investigations of the tau-pair background as a function of E_γ, within the selection of muon-pair events with isolated photons in the active acceptance, indicate that this background is at the level of $1.9 \pm 0.3\%$ in the lowest energy bins ($2-8$ GeV) becoming negligible at higher energies, <0.3% for $E_\gamma > 10$ GeV. As a function of $\alpha_{\mu\gamma}$ the background is $0.7 \pm 0.1\%$ for angles above 10°, with low angle values of up to $3 \pm 1\%$. The E_γ and $\alpha_{\mu\gamma}$ data distributions used below, were bin-by-bin corrected to account for this background. Other backgrounds within the selection of muon-pair events with isolated photons, from bhabha events and cosmic 'events', were found to be negligible.

Overview of detector effects

Distortions of the true physics distributions due to detector effects were considered to be split into efficiency and purity components with additional energy smearing effects in the E_γ case. Simulated $\mu^+\mu^-$ events generated using DYMU3 [48] and the full DELPHI simulation package were used to determine these quantities as functions of photon energy E_γ and the angle $\alpha_{\mu\gamma}$ between the momentum vectors of the photon and the nearer muon. A technique of obtaining a photon detection efficiency entirely from the data was developed and was applied both to the data and to the simulation events; this was used as a cross-check of the efficiency from the detector simulation.

4.8.1 Energy smearing, efficiency and purity

Figure 4.15 demonstrates both efficiency and energy smearing effects, from simulation. The reconstructed and true photon energies of a sample of radiative muon-pairs, selected as 'standard' muon-pairs with a 'true' isolated photon cluster in the calorimeter active acceptance are shown.

The entries at negative energy represent events in which no photon is reconstructed, constituting part of the inefficiency. The smearing of the sharp E_γ^{true} cut-off at 2 GeV is apparent with considerable population of the 0–2 GeV region in E_γ^{rec}. One bin, $20 < E_\gamma^{\mathrm{true}} < 21$ GeV, (cross hatched area) in singled out with the corresponding E_γ^{rec} (horizontally shaded area), showing a large energy spread and

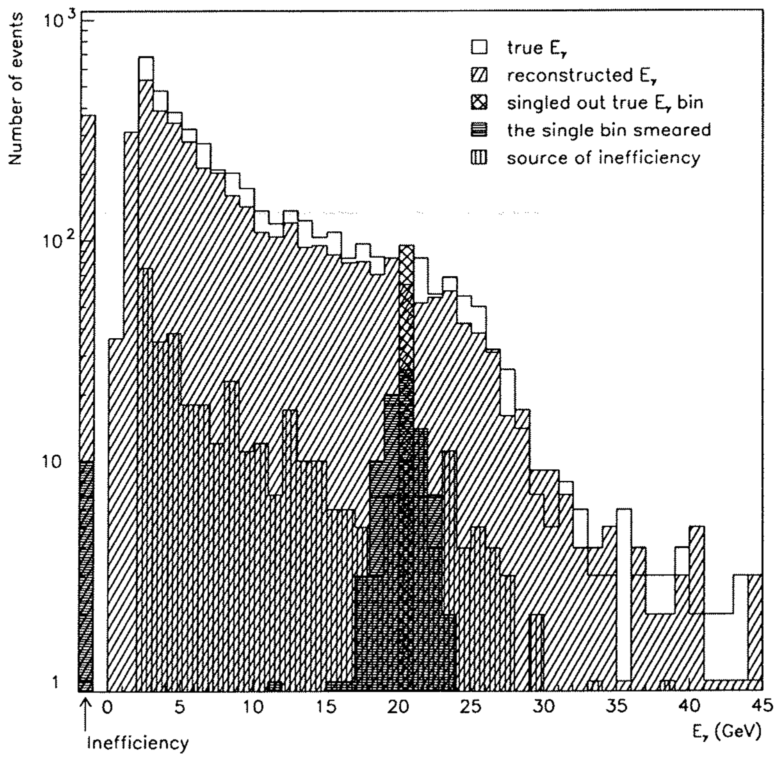

Figure 4.15: True and reconstructed photon energies (E_γ^{true} & E_γ^{rec}) in fully simulated $\mu^+\mu^-\gamma$ events.

including some events in which the photon is not reconstructed. The E_γ^{true} of the events that make up the inefficiency peak are shown as the vertically shaded area; there is a greater loss of events with E_γ^{true} at lower than at higher energies, this is further demonstrated in the efficiency section below.

4.8.2 Energy smearing

While it is impossible to remove the smearing on the energy reconstructed in the calorimeters (see section 3.7.2) and obtain the original true energy from the initial physics process on an event-by-event basis, it is possible to improve upon the the reconstructed E_γ^{rec} by use of a simple correction function E_γ^{cor}. This function represents the energy shifts and fractional energy changes modelled by the DELPHI simulation package. In this section a form of this correction function is obtained.

Selecting events where an isolated photon is observed (isolation defined above), which is in the active acceptance of the calorimeters and where the directions of the observed cluster and the generated photon are within 1°, ensuring that the same photon is under consideration, enables energy reconstruction effects to be separated from the inefficiency effects. Within such a selection, deviations between $\mathrm{E}_\gamma^{\mathrm{true}}$ and a corrected energy $\mathrm{E}_\gamma^{\mathrm{cor}}$ can be quantified by:

$$\mathcal{D}_{\mathrm{E}} = \frac{1}{\mathrm{N}_{\mathrm{ev}}} \sum \left(\frac{\mathrm{E}_\gamma^{\mathrm{cor}} - \mathrm{E}_\gamma^{\mathrm{true}}}{\mathrm{E}_\gamma^{\mathrm{true}}} \right)^2 , \tag{4.8}$$

where the summation is over the, N_{ev}, simulated events in the selection.

Using the following form for the corrected energy, which is designed to be a continuous linear relationship with a 'kink' at $\mathrm{E}_\gamma^{\mathrm{rec}} = \mathrm{a}_4$:

$$\mathrm{E}_\gamma^{\mathrm{cor}} = \mathrm{a}_1\, \mathrm{E}_\gamma^{\mathrm{rec}} + \mathrm{a}_2 \qquad (\text{for } \mathrm{E}_\gamma^{\mathrm{rec}} < \mathrm{a}_4 \text{ GeV}), \tag{4.9}$$

$$\mathrm{E}_\gamma^{\mathrm{cor}} = \mathrm{a}_3\, (\mathrm{E}_\gamma^{\mathrm{rec}} - \mathrm{a}_4) + \mathrm{a}_1 \cdot \mathrm{a}_4 + \mathrm{a}_2 \qquad (\text{for } \mathrm{E}_\gamma^{\mathrm{rec}} > \mathrm{a}_4 \text{ GeV}), \tag{4.10}$$

and varying the parameters a_1 to a_4 to minimize the quantity $\mathcal{D}_{\mathrm{E}}$ provides an algorithm for $\mathrm{E}_\gamma^{\mathrm{cor}}$ that more closely represents the true energy $\mathrm{E}_\gamma^{\mathrm{true}}$ than the cluster energy $\mathrm{E}_\gamma^{\mathrm{cor}}$. The results of such a (by hand) minimization are given in table 4.7; the starting position corresponds to the case, $\mathrm{E}_\gamma^{\mathrm{cor}} = \mathrm{E}_\gamma^{\mathrm{rec}}$. This functional form with a 'kink', at a_4 = 7.5 GeV, was used to prevent the high statistics at low energies from causing a poor treatment of events with high energy photons. The correction results are shown in figure 4.16, with the photon energy $\mathrm{E}_\gamma^{\mathrm{cor}}$ being more centered on the true energy $\mathrm{E}_\gamma^{\mathrm{true}}$; no resolution improvement occurs.

	$\mathrm{E}_\gamma^{\mathrm{cor}}$ parameters				
	a_1	a_2	a_3	a_4	$\mathcal{D}_{\mathrm{E}}$ (%)
Start position:	1.00	0.00	1.00	-	7.28
Minimum:	1.09	0.36	0.93	7.5	5.14

Table 4.7: Energy correction parameters and corresponding $\mathcal{D}_{\mathrm{E}}$.

4.8.3 Efficiency & Impurity from simulation

In obtaining the efficiency and purity as functions of photon energy E_γ, the energy correction was initially applied to the observed photon energy distribution in order to obtain the efficiency and purity with the energy shift effect removed. No such correction was required for $\alpha_{\mu\gamma}$ as the true generated angle (prior to detector effects) and the observed angle were found to be almost identical.

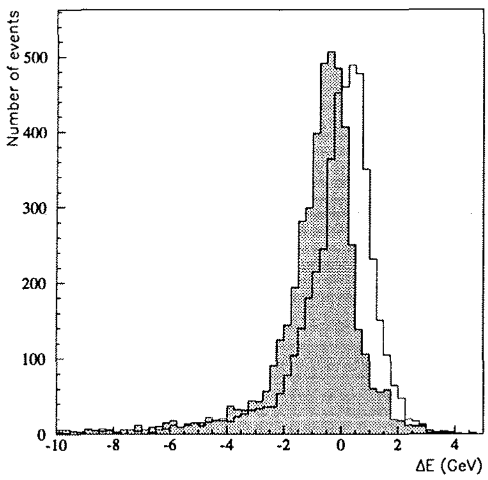

Figure 4.16: $E_\gamma^{cor} - E_\gamma^{true}$ compared to $E_\gamma^{rec} - E_\gamma^{true}$ (shaded area) in fully simulated $\mu^+\mu^-\gamma$ events.

- **Efficiency:** The photon detection efficiency from the simulation, ϵ_s, is defined as the fraction of events with a true isolated photon, within the active acceptance of the calorimeters, in which an isolated photon cluster is reconstructed.
- **Impurity:** The impurity, ι_s, is defined as the fraction of events with observed isolated photon clusters that do not correspond to true isolated photons within the active acceptance.

As shown in figure 4.17, $\epsilon_s(E_\gamma)$ is consistent with being constant for energies above 10 GeV; in the energy range 10–45 GeV the efficiency is 86 ± 1 %. The $\iota_s(E_\gamma)$ is also shown; some 90% of impurity events are in the energy range 2–6 GeV. The impurity is caused by the imperfect reconstruction of photon parameters leading to observed isolated photons, when the true photons are not within the acceptance (47% of the impurity events) or not satisfying the energy (30%) or isolation (23%) requirements.

As a function of $\alpha_{\mu\gamma}$, ϵ_s was found to be constant at $78 \pm 1\%$ in the range 15–100°, rising to $85 \pm 4\%$ in the range 100-120°. The rise at high angles is due to the kinematically restricted E_γ range for $\alpha_{\mu\gamma} > 90°$ (as demonstrated in section 4.7); that excludes low energy photons.

The difference in the efficiencies as a function of $\alpha_{\mu\gamma}$ and of E_γ is not surprising on consideration of figure 4.13(a) and observation of the stronger dependence of the

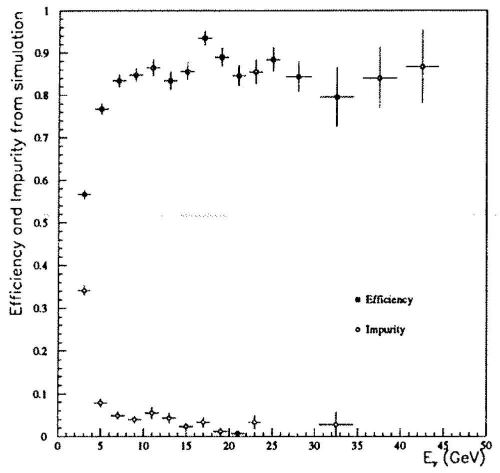

Figure 4.17: Efficiency and impurity determined from simulation.

efficiency on the energy E_γ than the angle $\alpha_{\mu\gamma}$. The lower efficiency in the $\alpha_{\mu\gamma}$ range 15-100°, than in the energy range $E_\gamma > 10$ GeV, occurs due to significant numbers of events with low energy photons ($E_\gamma < 10$ GeV) within the $\alpha_{\mu\gamma}$ range. At higher angles, $\alpha_{\mu\gamma} > 100°$, the kinematics forces E_γ above 10 GeV and results in consistent efficiencies as a function of energy $\epsilon_s(E_\gamma)$ and of angle $\epsilon_s(\alpha_{\mu\gamma})$.

4.8.4 Data efficiency by kinematic reconstruction

The photon detection efficiency from the data, ϵ_r, was determined using the kinematically predicted photon direction and energy obtained by assuming the final state topology $\mu^+\mu^-\gamma$ (the reconstruction technique is described in Appendix D).

- **Data technique efficiency,** ϵ_r: is defined as the fraction of events predicted to have a high energy isolated photon ($\alpha_{\mu\gamma}^{\rm pred} > 5°$, $E_\gamma^{\rm pred} > 10$ GeV) within the active acceptance of the calorimeters that are found to have an isolated photon cluster close to the expected position.

The criterion for a successful prediction is that the angle between the predicted and measured photon directions is less than 15°. For photons of energy above 10 GeV the fraction of events satisfying this criterion was 93%.

To attain a detection efficiency that can sensibly be compared to the efficiency from simulation it was first necessary to correct this efficiency to account for the

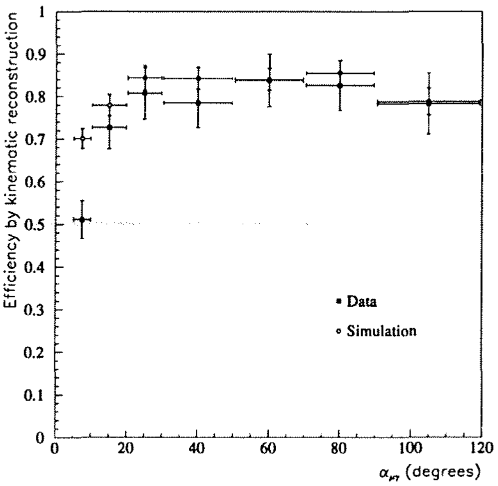

Figure 4.18: Efficiency by kinematic reconstruction, from data and simulation, as a function of the kinematically predicted angle, $\alpha_{\mu\gamma}^{\mathrm{pred}}$, after correction for the effectiveness of the kinematic reconstruction.

effectiveness of the reconstruction. This reconstruction correction factor, obtained both from the data and simulation, was defined as the fraction of events with observed high energy isolated clusters ($\alpha_{\mu\gamma}^{\mathrm{rec}} > 5°$, $E_\gamma^{\mathrm{rec}} > 10$ GeV) for which there is a successful prediction of photon position. The reconstruction correction factors as a function of $\alpha_{\mu\gamma}^{\mathrm{rec}}$ were found to be approximately constant for $\alpha_{\mu\gamma}^{\mathrm{rec}} > 5°$ at 0.91 ± 0.02 from the data and 0.98 ± 0.01 from simulation. Similar behaviour was observed as a function of E_γ^{rec} with constant values of 0.84 ± 0.02 from data and 0.98 ± 0.01 from simulation for $E_\gamma^{\mathrm{rec}} > 15$ GeV.

Applying these reconstruction effectiveness correction factors to the data technique efficiency ϵ_r (defined above) yields $\epsilon_r^{\mathrm{corr}}(data)$ and $\epsilon_r^{\mathrm{corr}}(sim)$ from data and simulation as a function of E_γ and $\alpha_{\mu\gamma}$. They all exhibit similar behaviour, rising from values as low as 50% in the lowest energy (2–4 GeV) and angle (5–10°) bins up to a plateau value for $E_\gamma > 12$ GeV and for $\alpha_{\mu\gamma} > 30°$. The efficiencies $\epsilon_r^{\mathrm{corr}}(\alpha_{\mu\gamma}^{\mathrm{pred}})$ as a function of predicted angle $\alpha_{\mu\gamma}^{\mathrm{pred}}$, from data and from simulation, are shown in figure 4.18.

The plateau value for $\epsilon_r^{\mathrm{corr}}(\alpha_{\mu\gamma})$ was $81 \pm 3\%$ from data and $83 \pm 1\%$ from simulation, compared to the value from the simulation technique, $\epsilon_s(\alpha_{\mu\gamma})$, of $78 \pm 1\%$. As a function of E_γ, $\epsilon_r^{\mathrm{corr}}(E_\gamma)$ had the plateau values $80 \pm 2\%$ from data and $83 \pm 1\%$ from simulation, compared to the simulation technique value, $\epsilon_s(E_\gamma)$, of $86 \pm 1\%$.

4.8.5 Application of the corrections

The various plateau efficiencies described in above sections, as a function of E_γ and $\alpha_{\mu\gamma}$, are collected in table 4.8.

	Plateau efficiency	
	E_γ	$\alpha_{\mu\gamma}$
ϵ_s	86 ± 1	78 ± 1
$\epsilon_r^{\mathrm{corr}}(sim)$	83 ± 1	83 ± 1
$\epsilon_r^{\mathrm{corr}}(data)$	80 ± 2	81 ± 3
ϵ	83 ± 2	76 ± 3

Table 4.8: Compilation of plateau photon detection efficiencies (%) as functions of E_γ and $\alpha_{\mu\gamma}$, obtained by various methods.

The significant differences in the efficiencies obtained from the simulation and data techniques are taken to indicate a deficiency in simulation performance. To account for this, the simulation efficiencies ϵ_s were corrected by the ratio of data technique efficiencies $\epsilon_r^{\mathrm{corr}}$ from data and from simulation, yielding the corrected plateau efficiencies, ϵ, of table 4.8.

An overall systematic error of 8% was assigned to the efficiencies, based on the results of the above studies. The statistical errors on these efficiencies are significantly smaller than the estimated systematic error.

The data used encompass two significantly different high voltage settings for the HPC. No significant effect on the detection efficiency of isolated photons was observed due to this change.

4.9 Results on radiative $\mu^+\mu^-$ events

The total number of $\mu^+\mu^-$ events selected is 46561($N_{\mu^+\mu^-(\gamma)}$), of which 1682 have isolated photons within the calorimeter active acceptance. The energy and angular spectra of these isolated photons are given in figure 4.19, the corrected data distributions are compared to the true distributions from simulation; the normalisation is to the number of $\mu^+\mu^-$ events. The ratio of the number of events with isolated photons to the total for data and simulation is given in Table 4.9.

There are no significant deviations between the energy and angular spectra obtained and the predictions of the DYMU3 simulation, at the present level of statistics

$N_{\mu^+\mu^-(\gamma)}$	46561
$N_{\mu^+\mu^-(n\gamma);n\geq1}$ isolated photons	1682
$N_{\mu^+\mu^-(n\gamma);n\geq1}$ / $N_{\mu^+\mu^-(\gamma)}$ (Data)	$3.61 \pm 0.09\%$
$N_{\mu^+\mu^-(n\gamma);n\geq1}$ / $N_{\mu^+\mu^-(\gamma)}$ (Monte Carlo)	$3.74 \pm 0.06\%$

Table 4.9: The numbers of 'standard' muon-pairs and the number of these with 'isolated photons' (as defined in section 4.8). The ratio of these numbers is compared with the DYMU3 simulation prediction after the full detector simulation (statistical errors only).

and understanding of the systematics. The small deviation in the energy range 18–30 GeV is not considered to be significant. The results are in agreement with an analysis of radiative lepton events by the OPAL collaboration [58]; the results here are based on 6 times higher statistics.

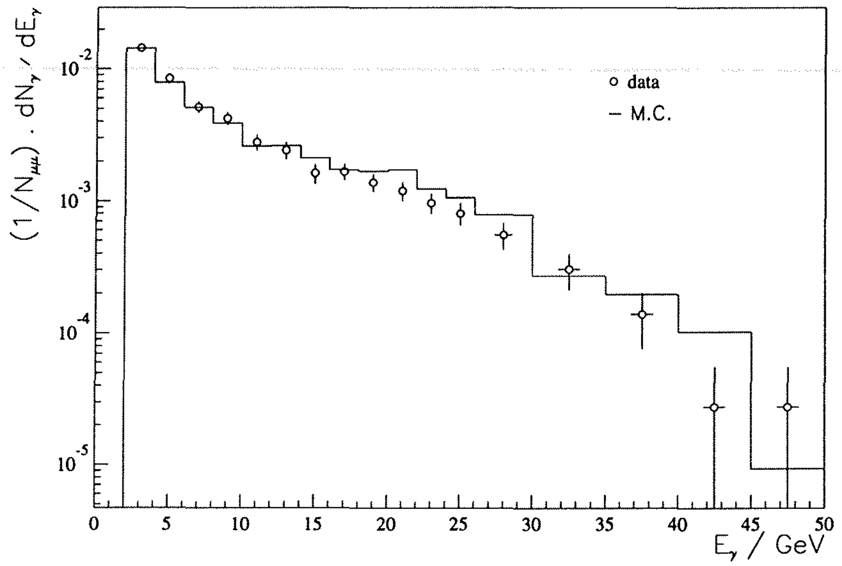

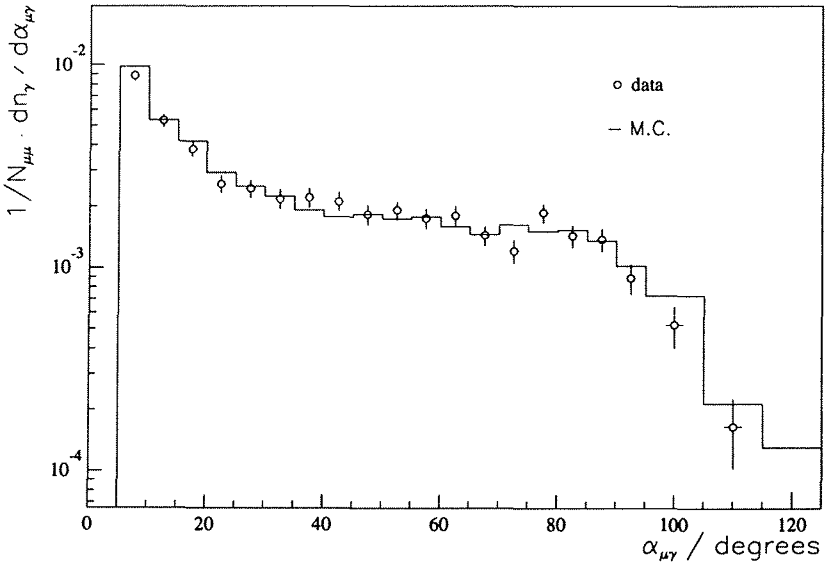

Figure 4.19: Corrected distributions for isolated photons of energy E_γ and angle $\alpha_{\mu\gamma}$ to the nearer muon. The errors shown are statistical only. The solid line shows the DYMU3 prediction with a factor of two higher statistics.

Chapter 5

The reaction $e^+e^- \to \mu^+\mu^-$ with $\mathrm{M}_{\mu\mu} < \mathrm{M}_\mathrm{Z}$

In this chapter, after briefly introducing and motivating the study, two techniques (**A** and **B**) of selecting events with predominantly initial state photons are presented. With these event samples and a measurement of the reduced effective interaction energy, the cross section and asymmetry values are then obtained at energies below that of the Z^0.

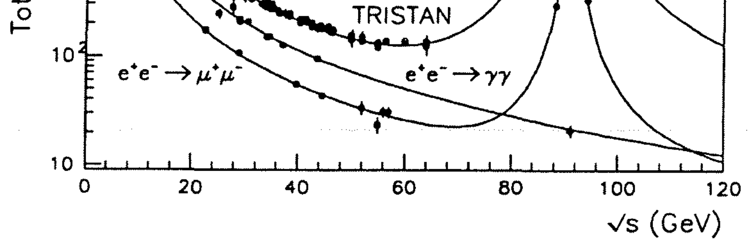

Figure 5.1: Measurements of $\sigma(e^+e^- \to f\bar{f})$ over a range of centre-of-mass energies.

5.1 Introduction

The largest corrections applied to the Born-level muon-pair cross section σ and asymmetry A_{FB}, to obtain the measured quantities, are due to initial state photon radiation[1], as discussed in section 1.5.1. Events with initial state photons, of energy E_γ, can be considered to have an effective interaction energy $\sqrt{s'}$ below that of the Z^0 peak $\sqrt{s}(= 2E_b)$, where:

$$\sqrt{s'} = \sqrt{s}\left(1 - \frac{E_\gamma}{E_b}\right)^{1/2}, \tag{5.1}$$

as derived in Appendix E. Thus an identification of muon-pair events with predominantly initial state radiation and determination of the energy of the initial state photons allows these effects to be isolated. This enables the underlying Born cross section and asymmetry to be measured at reduced effective centre-of-mass energies $\sqrt{s'}$ or $M_{\mu\mu}$. As apparent from figure 5.1, this energy region between TRISTAN ($\sqrt{s} \sim 60$ GeV) and LEP energies has not been explored previously, encouraging the low precision radiative measurements presented in this chapter.

Events with predominantly final state photons will also lead to a reduction in the muon-pair invariant mass, despite the interaction energy for these events being $\sqrt{s} \sim M_Z$. The reduced effective interaction energy $\sqrt{s'}$ (as defined above) can only be identified with the muon-pair invariant mass $M_{\mu\mu}$ when the event contains predominantly initial state photons.

5.2 Distinguishing initial & final state photons

It is possible to make a distinction between events with predominantly initial state photons or predominantly final state photons due to the very different angular distributions of the produced photons in these processes, as shown in figure 5.2. Note the importance of the polar angle cuts applied to the muons in dictating the form of the final state photon angular distribution.

Initial state photons are mainly produced at small angles to the beam direction whereas final state photons are produced close to the direction of the muons, as

---

[1] The distinction between initial and final state photons is, of course, not strictly valid in a quantum mechanical interpretation. However, this distinction is made in the DYMU3 generator and allows a simplified discussion.

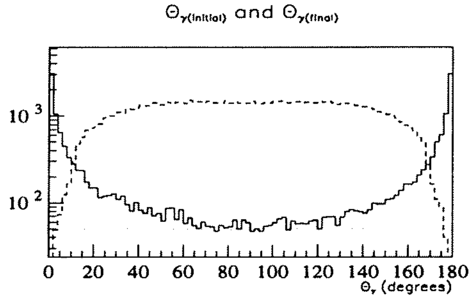

Figure 5.2: The DYMU3 generator level polar angle, θ_γ, of the highest energy photon in $\mu^+\mu^-\gamma$ events classed as "true" ISR (solid line) and "true" FSR (dashed line), as defined in text; obtained from a total of $\sim 0.7 \cdot 10^6$ generated muon-pair events.

shown in section 4.9. Initial state photons will, in most cases, not be seen in the calorimeters of the detector, but go down the beam-pipe.

For ease of discussion, events with predominantly initial/final state radiation are termed ISR/FSR events; with definitions in terms of photon energies:

$$\textbf{ISR events:} \quad \sum \mathrm{E}_{\gamma(\mathrm{i})} \geq 1 \text{ GeV} \quad \text{and} \quad \sum \mathrm{E}_{\gamma(\mathrm{f})} \leq 1 \text{ GeV},$$
$$\textbf{FSR events:} \quad \sum \mathrm{E}_{\gamma(\mathrm{f})} \geq 1 \text{ GeV},$$

where $\mathrm{E}_{\gamma(\mathrm{i})}$ and $\mathrm{E}_{\gamma(\mathrm{f})}$ are the energies of initial and final state photons. At the DYMU3 generator level, prior to any detector simulation, the photon parameters and initial or final state nature of the photons are explicitly available allowing the "true" ISR or FSR character of an event to be determined. Generated events classified as ISR/FSR using this information are termed "true" ISR/FSR events.

The dominance of FSR events over ISR events, in the low mass region, is illustrated in table 5.1, where the distribution of ISR and FSR events in intervals of $\mathrm{M}_{\mu\mu}$ is shown, for simulated events. The events are selected by the angular **C4** and momentum **C2S** requirements of section 4.2. This FSR dominance adds to the difficulty of making a relatively pure selection of ISR events. High statistics are necessary for this study, due to the steeply falling energy spectra of initial state radiation ($\sim 1/E_\gamma$) and also due to the very small relative cross section in this energy region.

$M_{\mu\mu}$ [GeV]	31-38	38-45	45-52	52-59	59-66	66-73	73-80
N_{FSR}	325	994	1216	1828	4469	7052	11862
N_{ISR}	144	129	115	127	138	197	398

Table 5.1: Numbers of "true" ISR/FSR events obtained from $\sim 0.7 \cdot 10^6$ DYMU3 generated muon-pairs, in bins of $M_{\mu\mu}$.

5.3 Characteristics of ISR events

Events with high energy initial state photons and low energy final state photons, are expected to have a small acoplanarity angle[2] θ_{acop} due to the small momentum component of the photon(s) in the transverse plane. In addition the acolinearity angle θ_{acol} is expected to be large due to the sizable Lorentz boost of the muon centre-of-mass system. This behaviour is demonstrated by the x-y and z-y event displays of figures 5.3 and 5.4. The figures also demonstrate muon identification and the reconstructed unseen photon direction obtained by the kinematic fit.

5.4 Overview of ISR event selection

Two approaches are taken to implement this selection:

A Cuts are applied to quantities affected by the presence of the photon, such as the acolinearity and acoplanarity of the event; in addition events with significant energy detected in the calorimeters are rejected.

B The photon parameters are reconstructed from the measured muon parameters by means of a kinematic fit (using the constraints from energy-momentum conservation) assuming only one photon is produced; then cuts are applied to the photon parameters.

Approach **A** limits the kinematically allowed directions and energies of produced photons and thus its consequences are similar to approach **B**. The advantage of technique **B** is that it makes use of all available information allowing the effective centre-of-mass energy to be obtained with greater accuracy, as well as being the most direct technique once the photon parameters have been obtained. Technique

---

[2] The acoplanarity is defined as the angle between the muon momentum vectors projected into the x-y plane.

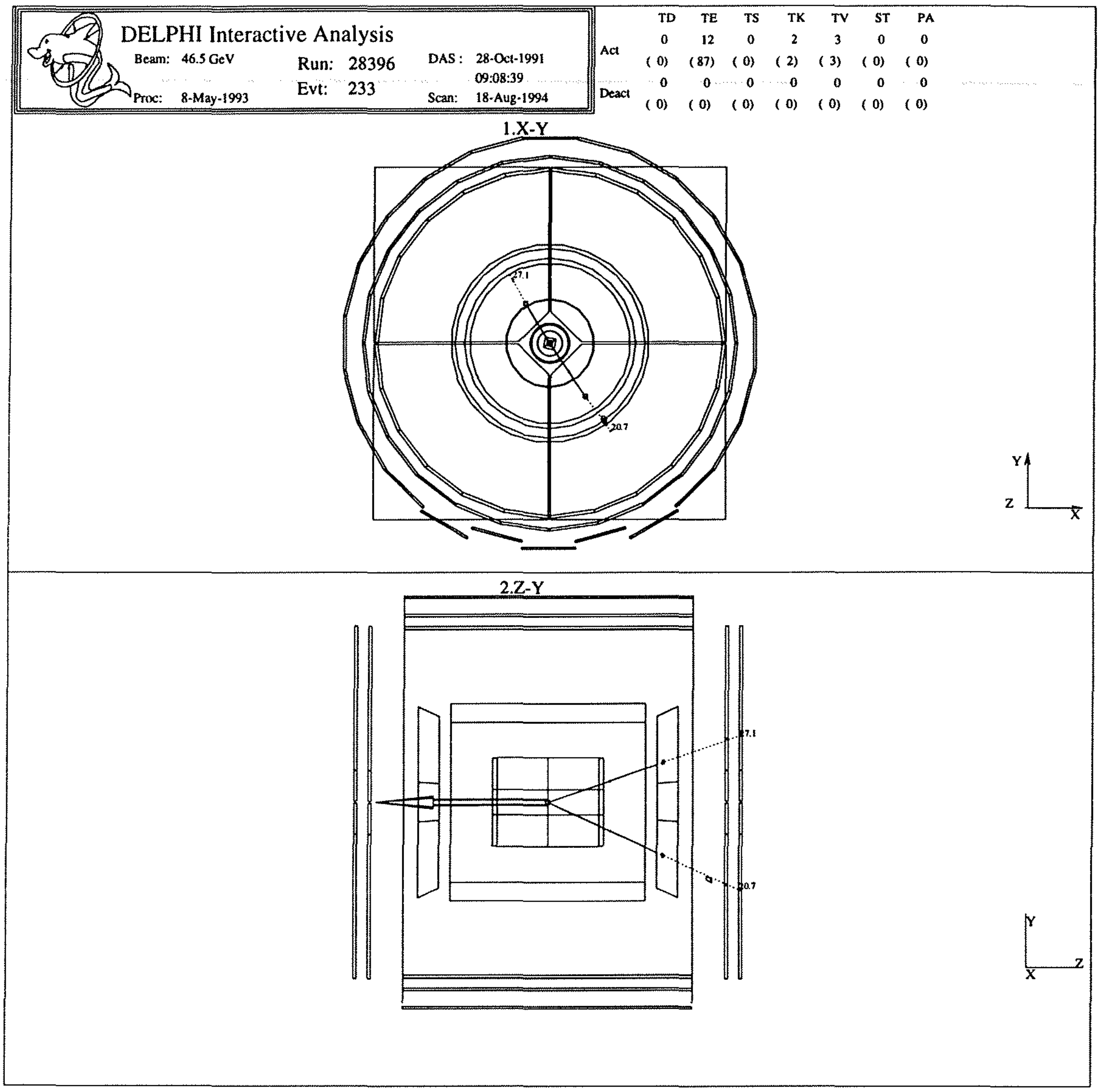

Figure 5.3: Display of a $\mu^+\mu^-\gamma$ event in the x-y and z-y planes, where no significant photon is reconstructed in the calorimeters. Both muons leave FEMC energy deposits consistent with a MIP and have hits in the MUF; one also leaves a trail in the forward HCAL. The 1-photon kinematic fit predicts a photon of energy 44.1 GeV at a polar angle 179.7°, as represented by the arrow. This high energy photon is considered to be an initial state photon, radiated from the initial positron. The reduced effective interaction energy is 20.8 GeV in this case.

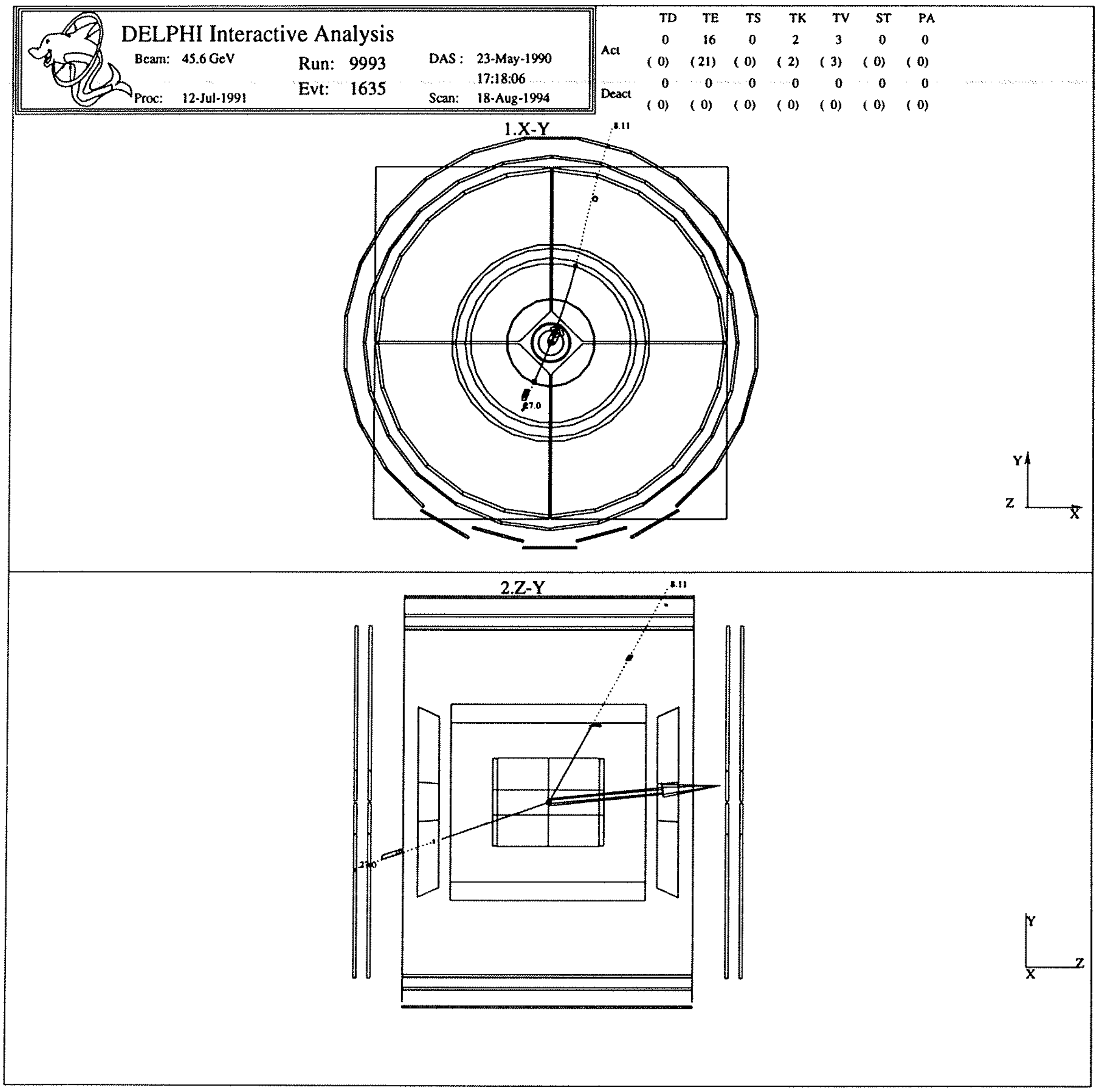

Figure 5.4: Display of a $\mu^+\mu^-\gamma$ event in the x-y and z-y planes, where no significant photon is reconstructed in the calorimeters. Both muons are identified in three sub-detectors in the endcap region and in the barrel region. The 1-photon kinematic fit predicts a photon of energy 38.2 GeV at a polar angle 12.7°, as represented by the arrow, corresponding to an effective interaction energy of 35.3 GeV. As shown subsequently, typical errors on the reconstructed photon direction are 2-3°. This high energy photon is considered to be an initial state photon.

A has the advantage of simplicity and for high energy photons (of energy greater than 10 GeV) equivalent results are expected. Both approaches have been pursued, allowing cross-checks to be made.

5.5 Selection of $e^+e^- \to \mu^+\mu^-(\gamma)$ events

The 'soft' muon-pair selection, described in section 4.2, is used to select muon-pair events with as little bias as possible. This results in greatly increased backgrounds at this intermediate stage from, in particular, tau-pairs and 2-photon reactions: $e^+e^- \to e^+e^-\mu^+\mu^-$, $e^+e^- \to e^+e^-\tau^+\tau^-$. However, as investigated in section 5.9, the subsequent cuts to select ISR events result in very small tau-pair and 2-photon physics backgrounds.

5.6 Selection A: acolinearity & acoplanarity cuts

The expected behaviour of the acolinearity and acoplanarity angles for ISR events is exploited by this selection technique.

As the principal criteria of this selection are based on the angular cuts, the first step is an estimation of the quality of acolinearity/acoplanarity reconstruction. Studies of the differences between reconstructed and generated acolinearity/acoplanarity show that typical errors are 0.05°. This good angular resolution allows the angular cuts to be studied using the DYMU3 generated events not passed through the full detector simulation, thus allowing high statistics studies to be made.

5.6.1 Generator level study of angular cuts

A total of $3.8 \cdot 10^5$ generated events were used (corresponding to approximately ten times higher statistics than the real $\mu^+\mu^-$ events). As indicators of the effectiveness of the selection, an efficiency and background contamination are defined by:

$$S_i = \frac{N_i^{cut}}{N_i}, \qquad S_f = \frac{N_f^{cut}}{N_f^{cut} + N_i^{cut}},$$

where $N_i\,(N_f)$ is the total number of $\mu^+\mu^-$ selected events where the highest energy photon is initial(final) state and $N_i^{cut}\,(N_f^{cut})$ are the numbers of $\mu^+\mu^-$ selected events after applying the acolinearity/acoplanarity cuts. S_i is the efficiency for selection of

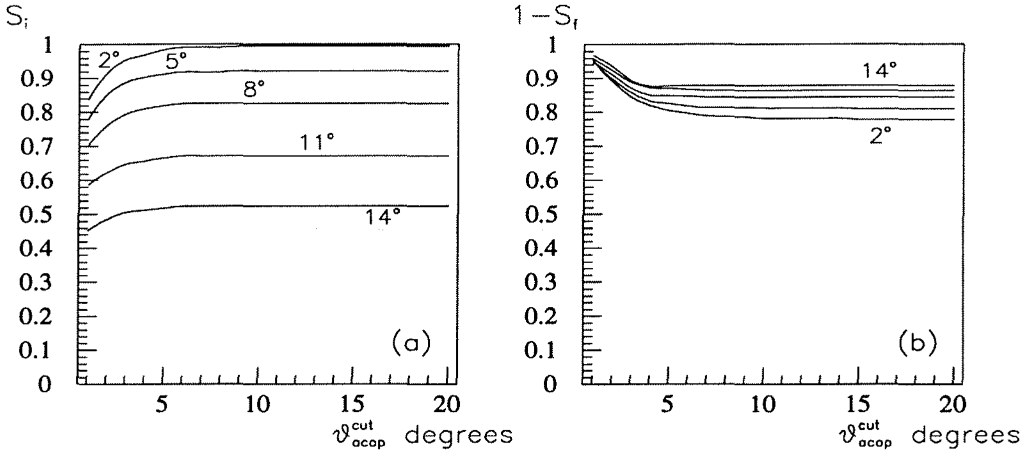

Figure 5.5: Generator level study of selection **A**: (a) efficiency S$_i$ and (b) purity 1−S$_f$, for the mass interval $73 < M_{\mu\mu} < 80$ GeV with angular cuts $\theta_{acop} < \theta^{cut}_{acop}$ and $\theta_{acol} > \theta^{cut}_{acol}$, as a function of θ^{cut}_{acop} for $\theta^{cut}_{acol} = 2, 5, 8, 11, 14°$, with an additional cut excluding photons of energy greater than 3 GeV within the acceptance of the electromagnetic calorimeters.

events with predominantly initial state photons and S_f shows the contamination of final state photon events in the sample of initial state photon events.

Studies of the behaviour of S_i and S_f in various $M_{\mu\mu}$ intervals for different angular cuts have been made; figure 5.5 shows the behaviour for the mass interval $73 < M_{\mu\mu} < 80$ GeV. The curves show S_i and $1 - S_f$ (the purity) as a function of θ^{cut}_{acop}, where $\theta_{acop} < \theta^{cut}_{acop}$, for $\theta_{acol} > 2$, 5, 8, 11, 14 degrees, with an additional cut requiring the absence of photons with energy greater than 3 GeV in the acceptance of the electromagnetic calorimeters. The values of S_i and $1 - S_f$ shown here are higher than can be achieved in practice, due to the effects of momentum smearing and photon detection inefficiency. The general behaviour of S_i and S_f is found to be the same in all the mass intervals.

The angular cuts in the mass intervals are chosen so as to optimize S_i, S_f and keep the τ background negligibly small; large θ^{cut}_{acol} and θ^{cut}_{acop} result in S_i, S_f close to their asymptotic values. The cuts chosen in the various mass intervals are presented in table 5.2.

$M_{\mu\mu}$ in GeV	17 - 38	38 - 45	45 - 52	52 - 59	59 - 66	66 - 73	73 - 80
$\theta_{acol} >$	15	15	15	15	15	12	7
$\theta_{acop} <$	15	10	9	9	6	4	4

Table 5.2: Acolinearity and acoplanarity cut values used (degrees) for the selection of ISR events; the acolinearity is required to be greater that the value shown and the acoplanarity is required to be less than the value shown.

5.6.2 Studies using fully simulated events

A sample of $5.6 \cdot 10^4$ fully simulated muon-pair events with high energy photons was produced by performing the simulation for events with muon-pair invariant mass, at the generator level, of less than 84 GeV. Within this limited mass range the sample allows distributions equivalent to those obtainable from $0.89 \cdot 10^6$ fully simulated muon-pair events.

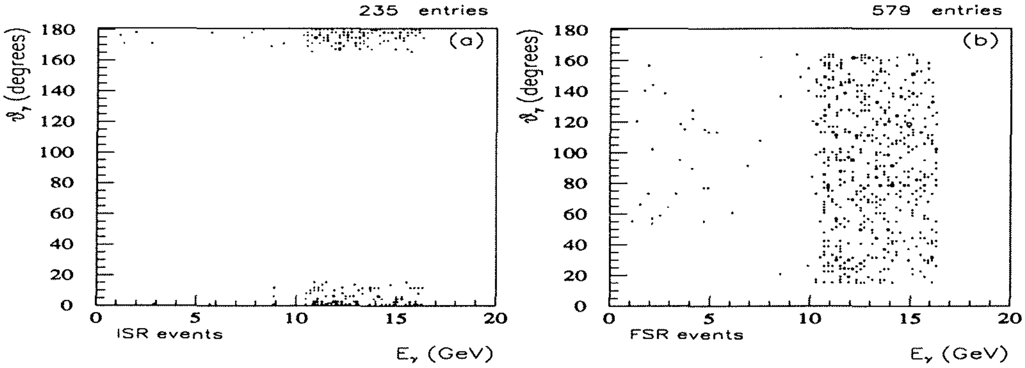

Figure 5.6: The θ_γ vs E_γ distributions from the $0.89 \cdot 10^6$ fully simulated muon-pair event sample, discussed in the text, (for the mass interval $73 < M_{\mu\mu} < 80$ GeV and requiring $\theta_{acol} > 7°$, $\theta_{acop} < 4°$) are presented. They are divided into (a) ISR and (b) FSR events by using the truth information on the produced photons.

The angular and energy distributions of the radiated photon, after angular cuts have been applied, are presented in figure 5.6 for initial and final state photon events, selected using the truth information on the produced photons. It can be seen that the FSR classed events have θ_γ in the approximate range 20–160°. This arises due to the 20° cut on the polar angle of the muons together with the small angles between the muon and final state photon directions. The structure in E_γ arises from the restricted mass interval of figure 5.6 imposing an allowed range in photon energy of

10–16 GeV; the few events with E_γ outside this band arise due to the presence of more than one significant photon in the event.

The FSR event dominance after the angular cuts demonstrates the necessity of a veto against events in which a hard photon is seen in the calorimeters for this selection. Details of photon detection techniques and efficiencies have been discussed in section 4.6.

5.6.3 Selection A criteria

The selection requires:

- The invariant mass of the muon-pair $M_{\mu\mu} < 80$ GeV.
- The acolinearity angle $> \theta^{cut}_{acol}$ depending on the mass interval, as shown in table 5.2.
- The acoplanarity angle $< \theta^{cut}_{acop}$ depending on the mass interval.
- No clusters in HPC and FEMC with energy greater than 3 GeV.

Within this selection the fraction of "true" ISR events, defined in section 5.2, is at the level of 70%. The "true" FSR contamination $\sim$ 15% for $E_\gamma < 15$ GeV and is $\lesssim 3\%$ for more energetic photons.

5.7 Selection B : reconstructed unseen photon

The first step is to reconstruct the unseen photon parameters from the muon momentum vectors and then devise a selection scheme based on these parameters. The angle of the photon to the beam direction is the principal quantity of use for the selection of events dominated by initial state photons.

5.7.1 Technique for reconstruction of unseen photons

The assumption of three-body kinematics allows an unseen photon to be reconstructed by performing a one constraint kinematic fit using the parameters and full error matrices of the muons. The basic hypothesis is that only one photon is radiated in the event. Neglecting the small energy spread in the energies of the incident particles prior to radiating, there are 9 variables: 6 muon parameters $1/p_1,\theta_1,\phi_1,1/p_2,\theta_2,\phi_2$ and 3 for the photon $E_\gamma,\theta_\gamma,\phi_\gamma$. The method used is fully described in Appendix D.

5.7.2 Performance of the reconstruction

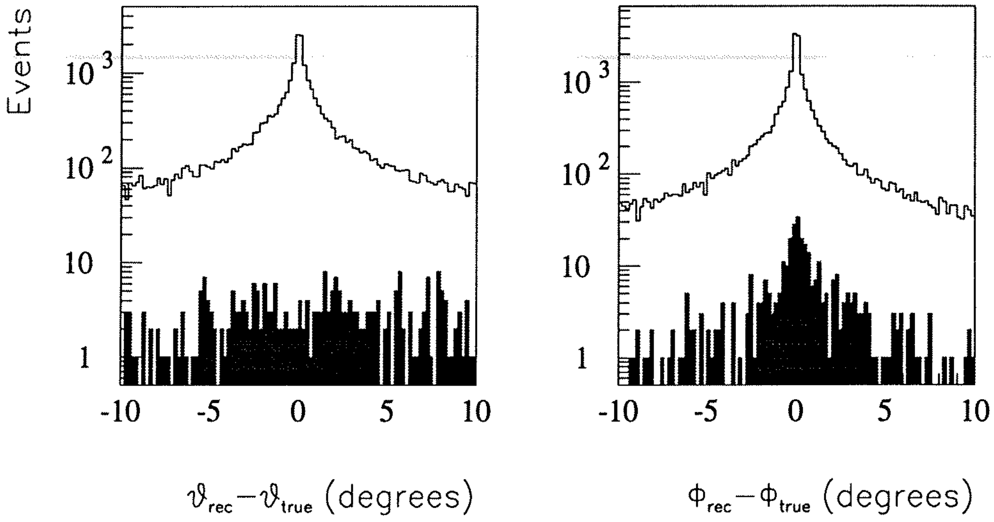

Figure 5.7: The reconstruction performance is demonstrated by comparison of the reconstructed and true photon angles, for a total of $0.15 \cdot 10^6$ simulated muon-pair events. For events with more than one photon, the comparison is made with the most energetic photon. The shaded histogram indicates events with two photons, each of energy greater than 1 GeV.

The performance of the reconstruction of the photon angles can be seen from figure 5.7. The comparatively small number of events with two photons, each of energy greater than 1 GeV, shown in the shaded portion of figure 5.7, indicates that the primary cause of poor photon reconstruction is the finite muon momentum resolution rather than events with two hard photons. Due to this there is a photon energy below which it is impossible to distinguish an event as having a photon or not. In order to remove soft photon events without imposing too severe an acolinearity cut (or equivalently a photon energy cut) that would limit the range of $\sqrt{s'}$ under study, the χ^2 probability P(0γ) is used. This probability indicates how consistent an event is with the hypothesis that no hard photons were produced.

Figure 5.8 shows the consistency of the real data events with the two hypotheses of either 1 photon produced or no photons. The small population in the region of high $P(0\gamma)$ and low $P(1\gamma)$ is because events with a low probability in the one photon fit cannot have a high probability in the more constrained zero photon fit.

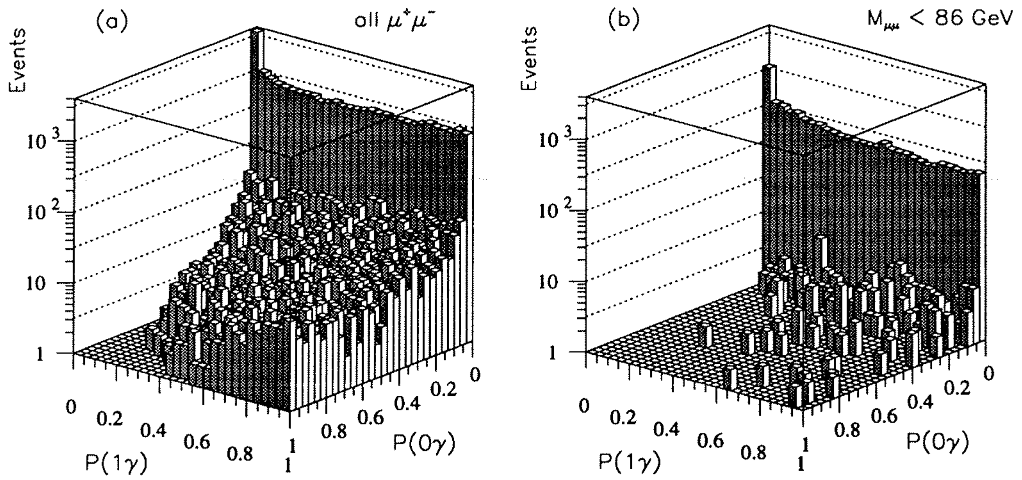

Figure 5.8: $P(1\gamma)$ and $P(0\gamma)$ are the χ^2 probabilities from fits assuming respectively that only 1 photon is produced and that no photons are produced. Plot (a) is obtained from the full data sample of $\mu^+\mu^-$ events and plot (b) from events in the invariant mass range $M_{\mu\mu} < 86$ GeV.

The zero photon fit is, after all, a special case of the one photon fit with very low energy photons.

The "wall" of events at low $P(0\gamma)$ contains the events of interest. Events with high energy photons in the mass range $M_{\mu\mu} < 86$ GeV are selected by requiring $P(0\gamma) \leq 10^{-2}$ and $P(1\gamma) \geq 10^{-2}$, thus ensuring accurate reconstruction of the unseen photon parameters. The ISR/FSR distinction is made by requiring that the reconstructed photon has an angle to the beam direction θ_γ of less than 20° and an angle to the nearer muon, $\alpha_{\mu\gamma}$, of greater than 10°; also it is demanded that no electromagnetic clusters with energy greater than 3 GeV are present in the HPC or FEMC.

5.7.3 Obtaining the effective centre-of-mass energy

The performance of the reconstruction and selection is shown in figure 5.9, by comparison of the reconstructed and true photon energies. In 71% of the selected events the photon energy is reconstructed to within 1 GeV. However there is a tendency for events with a low energy photon or with no photon to have too high a

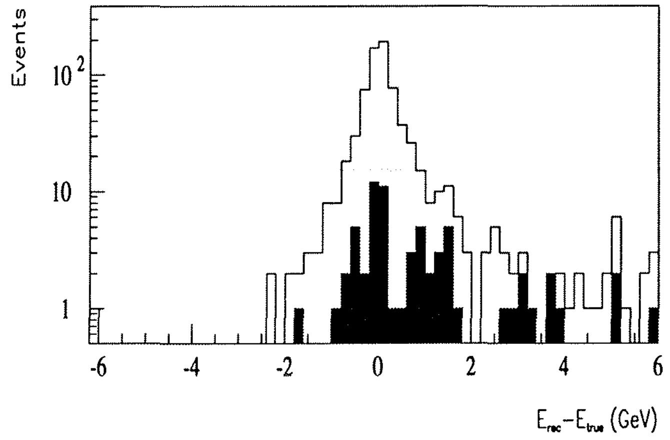

Figure 5.9: The reconstruction of the unseen photon, in simulated events selected as ISR by method B and with invariant mass $M_{\mu\mu} < 86$ GeV, is demonstrated by comparison of the photon energy E_γ reconstructed by the kinematic fit with the true energy. In events with more than one photon the comparison is made with the most energetic photon. The shaded histogram indicates those events with two photons, each of energy greater than 1 GeV.

reconstructed energy. The events with two hard photons, shaded in the figure, can be seen to constitute an overall impurity of $\sim 6\%$ within the selection.

As a cross-check of the energy reconstruction, the effective energy was calculated using the additional assumption that the photon direction is along the beam direction. This allows the photon energy to be calculated using energy-momentum conservation and assuming zero mass for the muons:

$$E_\gamma = \frac{|\sin(\theta_1 + \theta_2)|}{|\sin(\theta_1 + \theta_2)| + \sin\theta_1 + \sin\theta_2}\sqrt{s},$$

leading directly to the effective centre-of-mass energy or, equivalently, the muon-pair invariant mass $\sqrt{s'}$ (see equation 5.1). Simulation studies indicate that this $\sqrt{s'}$ is somewhat closer to the true effective centre-of-mass energy than the $\sqrt{s'}$ obtained from the fit, once the selection of ISR events has been made. Equivalent behaviour was obtained from a fit (mentioned in Appendix D) assuming that the single photon was travelling in the beam direction, as expected. This occurs due to the polar angle distribution being very peaked in the beam direction, for the highest energy photons in ISR events, as shown in figure 5.2.

5.7.4 Selection B criteria

Using the χ^2 probabilities of the fits assuming $\mu^+\mu^-$, $P(0\gamma)$, and assuming $\mu\mu\gamma$, $P(1\gamma)$ and the reconstructed photon parameters, the selection is made as follows:

- Event should not be consistent with $\mu^+\mu^-$, thus requiring $P(0\gamma) \leq 10^{-2}$
- For the $\mu\mu\gamma$ fit, require $P(1\gamma) \geq 10^{-2}$
- Angle between photon and beam direction $\theta_\gamma \leq 20°$
- Angle between photon and nearer muon $\alpha_{\mu\gamma} \geq 10°$
- No clusters in HPC and FEMC with energy greater than 3 GeV

The last cut results in a gain in the purity of ~ 4% in the mass region above 85 GeV, over a selection using the first four cuts alone.

5.8 Comparison of the two selections.

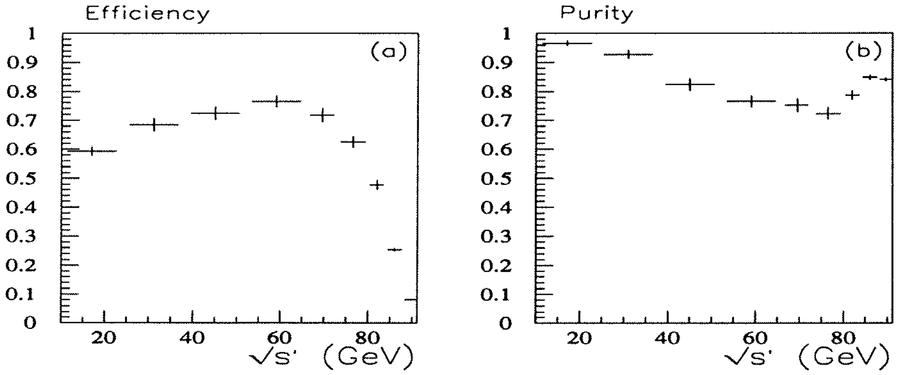

Figure 5.10: (a) ISR efficiency and (b) purity, as a function of effective energy $\sqrt{s'}$, from simulation, as defined in the text, for selection **B**

High statistics generator studies have been used to test the effectiveness of the selections. To match the data, the DYMU3 generated muon parameters are smeared with θ dependent errors on $\delta(1/p)$, and angular errors $\delta\theta$, $\delta\phi = 1$ mrad. In performing the generator level studies the initial or final state character of the photons is known, allowing purities and efficiencies of the selections to be obtained; in addition high statistics can be used.

The efficiency and purity are defined as follows:

- Efficiency: the fraction of the "true" ISR events that are selected,
- Purity: the fraction of the selected events that are "true" ISR events,

where "true" ISR events are defined in section 5.2.

Figure 5.10 shows the purity and efficiency as a function of the effective energy $\sqrt{s'}$ for selection **B**. Selection **B** has a higher efficiency than selection **A**. The purities are within 5% of each other, with selection **B** performing better at low $M_{\mu\mu}$, and also at high mass where technique **A** cannot be applied.

5.9 Backgrounds from $\tau^+\tau^-$ and γ-γ interactions

Due to the requirement of selecting muon-pair events without biasing against radiative events, the 'soft' muon-pair selection (as defined in section 4.2) is used; the resulting $\tau\tau$ background within this selection is 4.8%, as evaluated in section 4.4. However, on subsequently applying either of the initial state event selections **A** and **B**, this background is almost entirely removed. Simulation studies using $\sim$ 93000 generated tau-pairs and $\sim 1.3 \cdot 10^5$ generated muon-pairs, passed through the full detector simulation, lead to tau backgrounds of 0.32% in selection **A** and 0.64% in selection **B**, corresponding to less than one tau-pair event in each of the samples. The cosmic background evaluation technique, described in section 4.4, was applied to the ISR selections **A** and **B**. Indicating that no cosmic 'events' were within the selections, as would be expected from the predominantly back-to-back nature of cosmic 'events'.

Possible backgrounds from γ-γ interactions, have been investigated using $\sim$ 68000 generated $e^+e^- \rightarrow e^+e^-\mu^+\mu^-$ events and $\sim$ 10000 $e^+e^- \rightarrow e^+e^-\tau^+\tau^-$ events, passed through the full detector simulation. The predicted $e^+e^- \rightarrow e^+e^-\mu^+\mu^-$ backgrounds in selections **A**(**B**) were found to be $\sim$ 3(2) events respectively, whereas less than 1 $e^+e^- \rightarrow e^+e^-\tau^+\tau^-$ event was expected in the samples. The γ-γ background events were found to occur predominantly at low effective energies $\sqrt{s'} < 40$ GeV. No correction was applied to account for these small backgrounds.

5.10 Obtaining $\sigma(e^+e^- \to \mu^+\mu^-)$

As the number of ISR events is, to a good approximation, proportional to the cross section. An indirect measurement of the Born cross section at $\sqrt{s'}$ is obtained by scaling the SM expectation of the mean Born cross section in the energy range by the ratio of the number of events observed to the number expected from simulation. The normalization was performed by comparing the number of $e^+e^- \to \mu^+\mu^-$ events as selected in section 4.2 in data and simulation.

The adequate performance of the detector simulation, required by this cross section determination technique, was demonstrated in section 4.5. The expected final state radiation background in the $M_{\mu\mu}$ bins (obtained from a simulation study) cannot be corrected for in the determination of the cross section without independent knowledge of the impurity in the data sample. It is because of the difficulty of correcting for this background that it is important that a high purity selection is used. The measured cross sections are presented in figure 5.11 and table 5.3.

Selection **A**

$M_{\mu\mu}$ [GeV]	17-24	24-31	31-38	38-45	45-52	52-59	59-66	66-73	73-80
N(obs)	2	5	7	4	6	6	5	12	29
N(mc)	2.3	4.0	5.2	6.0	5.1	7.0	9.3	13.2	24.5
N(fsr)	0.0	0.1	0.2	0.4	0.4	0.8	1.5	1.0	3.9
σ [pb]	206.	165.	113.	39.	51.	28.	15.0	22.4	34.0
δ_σ [pb]	145.	74.	43.	19.	21.	12.	6.7	6.5	6.3
σ_{Born} [pb]	238.4	130.8	82.8	57.3	42.3	33.0	27.4	25.1	29.1

Selection **B**

$M_{\mu\mu}$ [GeV]	17-24	24-31	31-38	38-45	45-52	52-59	59-66	66-73	73-80	80-84	84-86
N(obs)	4	5	6	8	7	4	8	14	34	45	40
N(mc)	1.7	5.2	3.5	6.6	5.7	6.1	10.5	16.6	30.1	37.1	37.1
N(fsr)	0.0	0.4	0.0	0.0	0.0	0.4	0.9	0.4	2.6	2.6	3.9
σ [pb]	545.9	124.8	142.2	70.0	52.2	21.6	20.9	21.2	32.8	58.3	94.1
δ_σ [pb]	386.0	66.4	76.8	30.6	24.5	12.2	8.5	6.6	6.9	10.7	18.0
σ_{Born} [pb]	238.4	130.8	82.8	57.3	42.3	33.0	27.4	25.1	29.1	48.1	87.3

Table 5.3: Observed and expected numbers of events for different $M_{\mu\mu}$ intervals from data N(obs) and from the full simulation N(mc), and the calculated cross sections with statistical errors, δ_σ, using selections **A** and **B**. The mean Born level cross section within the energy ranges, σ_{Born}, and also the prediction from simulation of the final state radiation background in the data sample N(fsr) are provided.

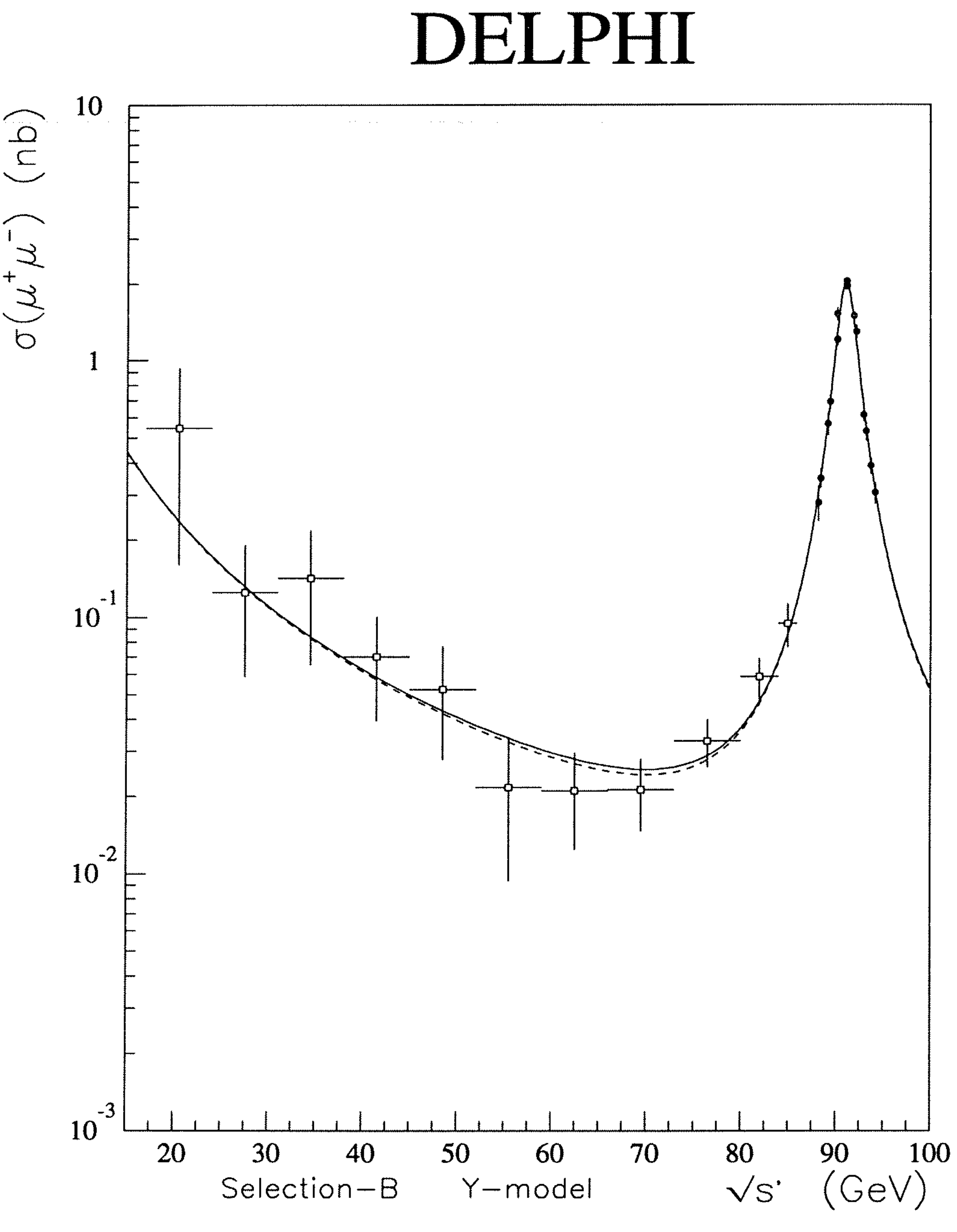

Figure 5.11: Cross section for $e^+e^- \to \mu^+\mu^-$ with selection **B**. The solid curve is the Born cross section in the SM and the dashed one is the cross section with the fitted values of $M_{Z'}$ and $\lambda_{Z'}$, using model Y. The solid dots are the on peak cross section measurements and the open dots are the below peak measurements. All the measurements are corrected to IBA values, using ZFITTER.

5.11 Obtaining $A_{FB}(e^+e^- \to \mu^+\mu^-)$

In calculating the forward-backward asymmetry (defined in section 1.4.2) for events which are far from being back-to-back, it is appropriate to deal with the angle made by the μ^+ or μ^- to the beam direction in the $\mu^+\mu^-$ rest frame, θ^* [59]. This is given by:

$$\cos\theta^* = \frac{\sin\frac{1}{2}(\theta_2 - \theta_1)}{\sin\frac{1}{2}(\theta_2 + \theta_1)} \tag{5.2}$$

where θ_1 and θ_2 are the measured polar angles of μ^+ and μ^- in the laboratory frame. The asymmetry $\mathrm{A_{FB}}(\sqrt{s'})$ is obtained by the counting method, using the number of events with $\cos\theta^* > 0$ and < 0, in bins of $\sqrt{s'}$, to provide $\mathrm{N_F}(\sqrt{s'})$ and $\mathrm{N_B}(\sqrt{s'})$. Thus using the asymmetry definition:

$$\mathrm{A_{FB}}(\sqrt{s'}) = \frac{\mathrm{N_F}(\sqrt{s'}) - \mathrm{N_B}(\sqrt{s'})}{\mathrm{N_F}(\sqrt{s'}) + \mathrm{N_B}(\sqrt{s'})}, \tag{5.3}$$

leading to the uncorrected asymmetry directly from the data, without recourse to comparisons between data and simulation.

5.11.1 Impurity correction

As the impurity events (final state photon or no hard photon events) have an effective energy on the peak (where the asymmetry is close to zero), their effect on the asymmetry is to make it less negative. Expressing the observed asymmetry, $\mathrm{A_{FB}}^{\mathrm{obs}}$, in terms of numbers of "true" ISR events and contamination ($\overline{\mathrm{ISR}}$) events in the forward and backward directions:

$$\mathrm{A_{FB}}^{\mathrm{obs}} = \frac{(\mathrm{N_F}^{\mathrm{ISR}} + \mathrm{N_F}^{\overline{\mathrm{ISR}}}) - (\mathrm{N_B}^{\mathrm{ISR}} + \mathrm{N_B}^{\overline{\mathrm{ISR}}})}{(\mathrm{N_F}^{\mathrm{ISR}} + \mathrm{N_F}^{\overline{\mathrm{ISR}}}) + (\mathrm{N_B}^{\mathrm{ISR}} + \mathrm{N_B}^{\overline{\mathrm{ISR}}})}, \tag{5.4}$$

leads to:

$$\mathrm{A_{FB}}^{\mathrm{obs}} = \mathrm{p}\mathrm{A_{FB}}^{\mathrm{ISR}} + (1-\mathrm{p})\mathrm{A_{FB}}^{\overline{\mathrm{ISR}}}, \tag{5.5}$$

where the purity, p, is as defined in section 5.8:

$$\mathrm{p} = \frac{\mathrm{N_F}^{\mathrm{ISR}} + \mathrm{N_B}^{\mathrm{ISR}}}{\mathrm{N_F}^{\mathrm{ISR}} + \mathrm{N_B}^{\mathrm{ISR}} + \mathrm{N_F}^{\overline{\mathrm{ISR}}} + \mathrm{N_B}^{\overline{\mathrm{ISR}}}}. \tag{5.6}$$

In the simple case of the background having an asymmetry of zero, the correction to obtain the $\mathrm{A_{FB}}^{\mathrm{ISR}}$ reduces to a division of the observed asymmetry by the purity. High statistics samples of smeared generator level events provide the asymmetry

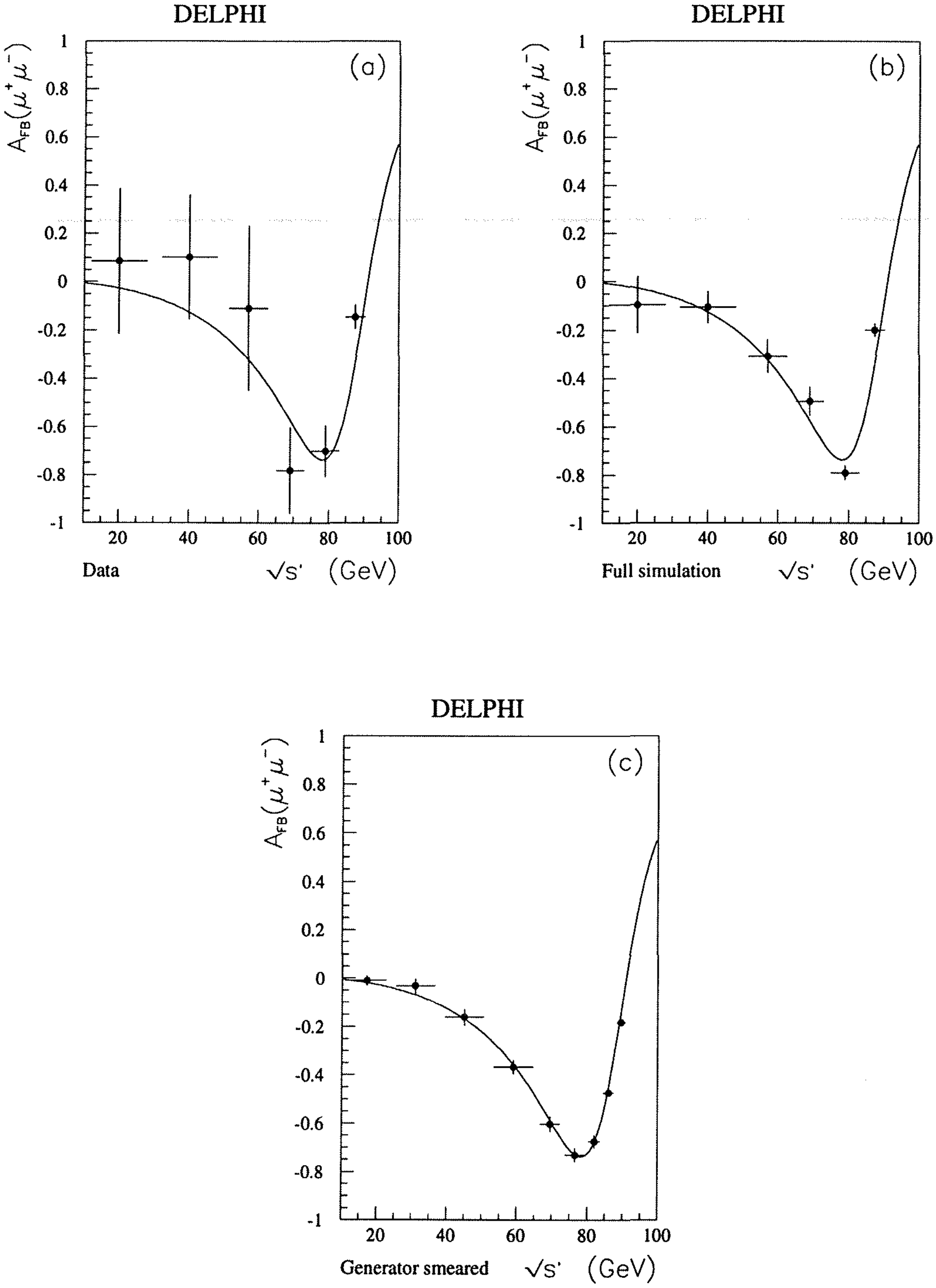

Figure 5.12: Asymmetry for $e^+e^- \to \mu^+\mu^-$ in bins of effective energy using selection **B**, after application of purity and acceptance corrections; for (a) data, (b) full simulation and (c) DYMU3 generated events after momentum smearing. The solid curve is the Born approximation asymmetry, which the measurements are expected to conform to.

of the contamination events within the sample in bins of $\sqrt{s'}$, in addition to the purity of the sample (as shown in figure 5.10(b)). The largest absolute value of the

(a) Data

$M_{\mu\mu}$ [GeV]		10-30	30-50	50-64	64-74	74-84	84-91
Measured	A_{FB}	0.09	0.07	-0.11	-0.62	-0.56	-0.13
	δA_{FB}	0.30	0.26	0.33	0.17	0.10	0.05
Background	A_{FB}	0.09	0.10	-0.11	-0.75	-0.68	-0.14
corrected	δA_{FB}	0.30	0.26	0.33	0.17	0.10	0.05
Fully	A_{FB}	0.09	0.10	-0.11	-0.78	-0.70	-0.15
corrected	δA_{FB}	0.30	0.26	0.34	0.18	0.11	0.05

(b) Simulation

$M_{\mu\mu}$ [GeV]		10-30	30-50	50-64	64-74	74-84	84-91
Measured	A_{FB}	-0.08	-0.11	-0.26	-0.41	-0.63	-0.17
	δA_{FB}	0.12	0.06	0.07	0.05	0.03	0.02
Background	A_{FB}	-0.10	-0.11	-0.30	-0.48	-0.76	-0.19
corrected	δA_{FB}	0.12	0.07	0.07	0.06	0.03	0.03
Fully	A_{FB}	-0.10	-0.11	-0.31	-0.49	-0.79	-0.20
corrected	δA_{FB}	0.12	0.07	0.07	0.06	0.03	0.03

(c) Smeared DYMU3 generated events

$M_{\mu\mu}$ [GeV]		10-24	24-38	38-52	52-66	66-73	73-80	80-84	84-88	88-91
Measured	A_{FB}	-0.01	-0.04	-0.15	-0.30	-0.49	-0.55	-0.57	-0.40	-0.15
	δA_{FB}	0.02	0.03	0.03	0.02	0.02	0.02	0.02	0.01	0.01
Background	A_{FB}	-0.01	-0.03	-0.16	-0.36	-0.58	-0.71	-0.65	-0.46	-0.18
corrected	δA_{FB}	0.02	0.03	0.04	0.03	0.03	0.03	0.03	0.01	0.01
Fully	A_{FB}	-0.01	-0.03	-0.16	-0.37	-0.60	-0.73	-0.68	-0.47	-0.18
corrected	δA_{FB}	0.02	0.03	0.04	0.03	0.03	0.03	0.03	0.01	0.01

Table 5.4: Selection **B** measured asymmetries, together with background corrected values and fully corrected values, in bins of effective energy; for (a) data, (b) full simulation and (c) smeared DYMU3 generated events.

contamination asymmetry of ~ -0.2 occurs in the energy range 73-84 GeV. Using the contamination asymmetry and the purity allows the observed asymmetry to be bin-by-bin corrected, to yield the "true" ISR asymmetry within the acceptance and momentum cut requirements.

5.11.2 Acceptance and momentum cut correction

The polar angle range imposed on the muon tracks ($20° < \theta < 160°$) results in a decrease in the observed asymmetry[3]. To obtain correction factors for this analysis,

---

[3] In a standard muon-pair analysis, with predominantly back-to-back tracks, a correction to

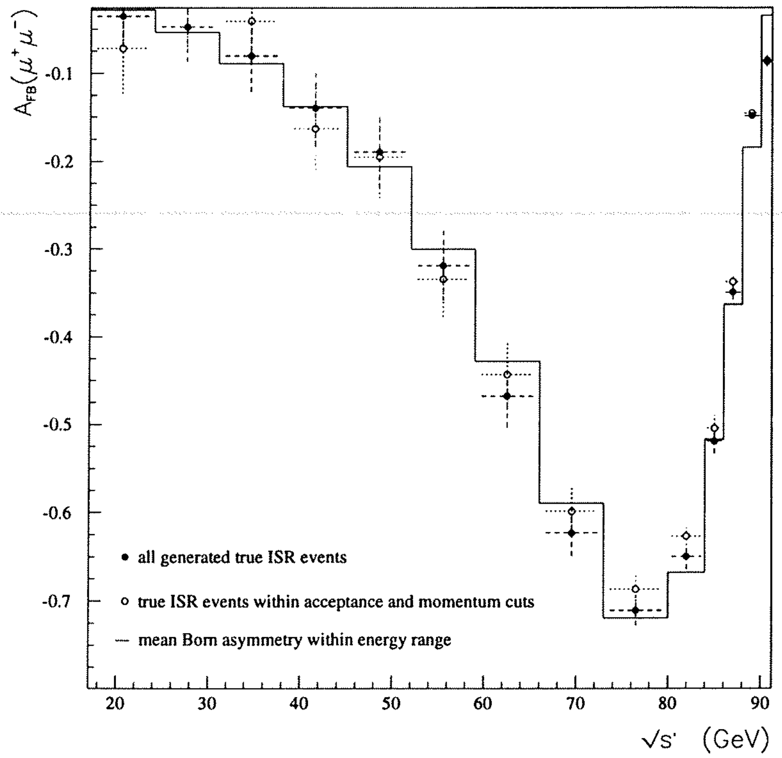

Figure 5.13: $e^+e^- \to \mu^+\mu^-$ asymmetry as a function of the muon-pair invariant mass, obtained from $2.96 \cdot 10^6$ DYMU3 generated events within two selections. The selections are "true" initial state (as defined in the text), with and without acceptance and momentum cuts. The solid line indicates the mean Born level asymmetry within the muon-pair invariant mass bin.

with predominantly far from back-to-back tracks, high statistics DYMU3 generator studies were performed.

Figure 5.13 shows the mean Born level asymmetry (solid line) together with the two asymmetries obtained from $2.96 \cdot 10^6$ DYMU3 generated events for the samples:

(i) all generated "true" ISR events,

(ii) "true" ISR events with both muons within $20° < \theta < 160°$ and the muon momenta (p_1, p_2) satisfying $p_1 > 12$ GeV, $p_2 > 7$ GeV.

The closeness of the two asymmetry values to the Born level cross section and to each other demonstrates the small size of this correction compared to the statistical measurement uncertainties. Dividing the asymmetry obtained from sample (i) by

---

compensate for the limited polar angle acceptance (between $\cos\theta$ values x and -x) is found to have the form: $A_{FB}(4\pi) = A_{FB}(x) \cdot (\frac{3+x^2}{4x}) = A_{FB} \cdot 1.0331$.

that from sample (ii), provides the correction factor to account for application of these cuts[4]. In the energy region $M_{\mu\mu} > 60$ GeV, the correction factor is found to be almost constant with value 1.034 ± 0.001.

5.11.3 Asymmetry results

The measured values together with the purity corrected and fully corrected values, using selection **B**, are presented in table 5.4. Values are given from the data, from fully simulated Monte Carlo events and from $5.3 \cdot 10^6$ DYMU3 smeared generated events, prepared as described in section 5.8. The fully corrected measurements are presented in figure 5.12

The high statistics sample of smeared generated events and the simulated event sample are useful in testing the method used to obtain and correct the asymmetries; by comparison of the asymmetries obtained with the theoretical expectations, as shown in figure 5.12(b)&(c). No significant deviations are observed.

As a cross-check, the asymmetries were also computed using the forward ($\theta > 90°$) or backward ($\theta < 90°$) nature of the positively and negatively charged muons, instead of a combination of these two quantities given by the center-of-mass angle θ^*, in expression 5.2 for $\cos\theta^*$. The asymmetry measurements by these two alternative techniques agree with the method used within the errors; for the three highest energy bins the agreement was within a half of the error.

5.12 Discussion of results

Up to and including the LEP run of 1992, corresponding to 46561 selected muon-pairs, a total of 76(90) events with interaction energy between 17 GeV and 80 GeV are collected in selections **A**(**B**); 51 of these events are common to the two selections. The number of events observed in $M_{\mu\mu}$ bins for the data and simulation using selection **A**, and the calculated cross sections are presented in table 5.3.

The mass region above 80 GeV is also probed by selection **B**. The results are presented in table 5.3, and figure 5.11. Studies of the effect on the results of using three different techniques to reconstruct the effective energy were made. The techniques used were the $M_{\mu\mu}$ calculated from the measured muon parameters, the

---

[4] Due to the small nature of this correction, the data points obtained using this multiplicative correction were consistent with those obtained using an additive correction technique.

effective energy obtained from the fit assuming a $\mu\mu\gamma$ topology, and also the energy calculated assuming a single initial state photon to be travelling in the beam direction. The resulting variations in the cross section were less than 20%.

All the measured cross sections (figure 5.11 and table 5.3) and the measured asymmetries (figure 5.12 (a) and table 5.4) are compatible with the expectations of the Standard Model.

5.13 Comparison with TRISTAN measurements

5.13.1 Cross section

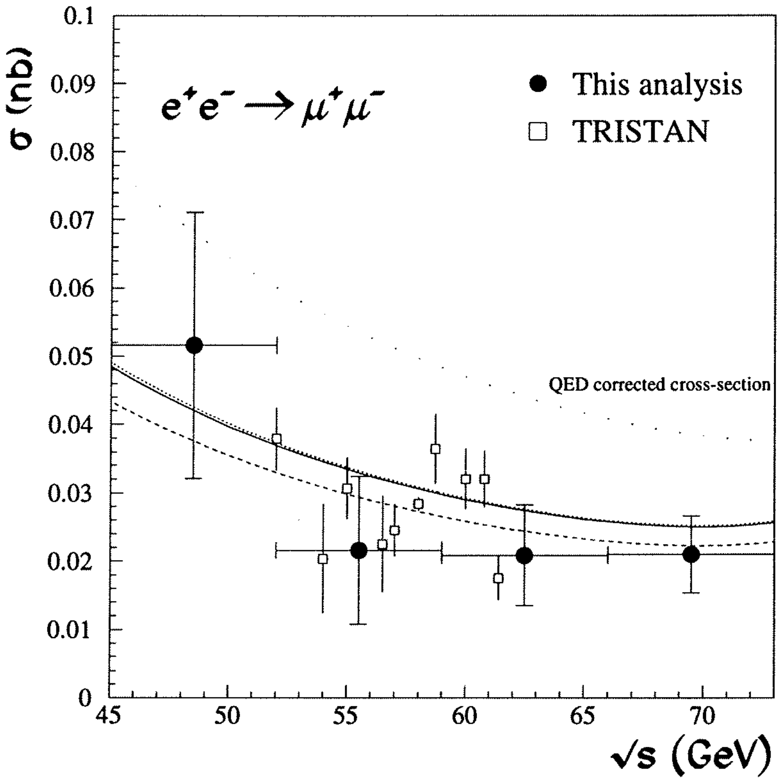

Figure 5.14: Cross section for $e^+e^- \to \mu^+\mu^-$ with selection **B** in the energy range $\sqrt{s}$=45-73 GeV, compared with measurements by TOPAZ at TRISTAN. The solid curve is the IBA cross section in the SM (from ZFITTER), which the measured points are expected to conform to. The dotted and dashed curves are obtained from the Born cross section expressions using $\alpha = 1/128.82$ and $\alpha = 1/137.036$ respectively. Also shown as a sparsely dotted line is the $\mathcal{O}(\alpha)$ QED corrected cross section, obtained from ZFITTER.

Figure 5.14 compares the cross section results with some direct measurements obtained by the TOPAZ Collaboration [60] at the TRISTAN collider. The TRISTAN measurements from [60] were presented as Born level $\alpha(0) = 1/137.036$ values. In order to compare them with the measurements obtained by this analysis they were first corrected to Born level $\alpha(M_Z{}^2) = 1/128.82$ values, by application of the correction factor: $(\alpha(M_Z{}^2)/\alpha(0))^2$. The Born level cross section expression 1.18 shows this to be the appropriate factor. The Born level $\alpha(M_Z{}^2) = 1/128.82$ curve (dotted on the figure) matches, very closely, the IBA cross section curve (solid line) provided by ZFITTER[5] and to which the measured points are expected to conform. The results are seen to be consistent with the TRISTAN measurements.

5.13.2 Asymmetry

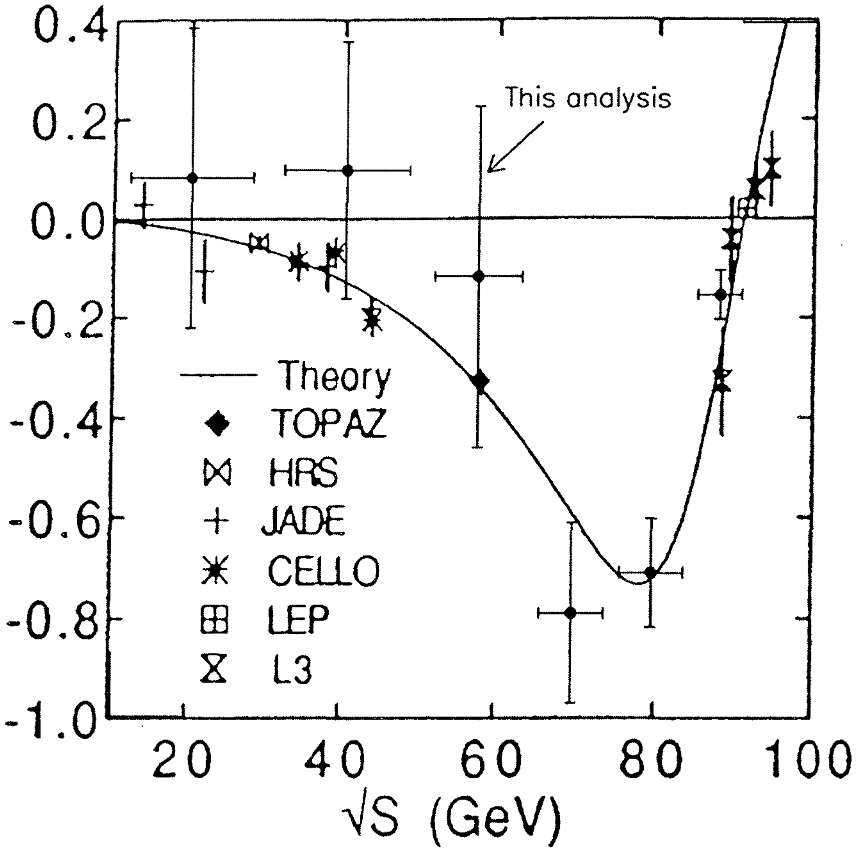

Figure 5.15: Asymmetry for $e^+e^- \to \mu^+\mu^-$ (using selection **B**) after application of purity, acceptance and momentum cut corrections, compared with other measurements. The solid curve is the Born asymmetry in the SM, which the measured points are expected to conform to.

Figure 5.15 compares the asymmetry results obtained with direct measurements from low energy experiments (from [61]), as well as some on peak measurements

---

[5] This indicates that the running of α is the dominant correction to the $\alpha(0)$ Born cross section values.

from the L3 Collaboration. The results are seen to be consistent with previous measurements and with theoretical expectations.

Chapter 6

Obtaining Z′ limits

Many possible extensions to the Standard Model predict additional neutral heavy gauge bosons Z′, of mass $M_{Z'}$ larger than M_Z. The emergence of Z′ in various models was discussed in section 2.5; figures 2.1& 2.2 demonstrate the predicted deviations, showing the largest deviations to occur in the region $\sqrt{s} \sim 70$ GeV. The cross section measurements presented in chapter 5 uniquely probe this energy region, motivating the limit determination presented in this chapter. Limits are placed on Z′ mass and mixing parameters in several models by comparing predictions of the effects of Z′ to the observations, as a function of the parameters of the models.

6.1 E_6 and L-R models

The effects of Z′ for the L-R and E_6 models on the cross sections and asymmetries were calculated using an addition to the ZFITTER (version 4.5)[14] program, called ZEFIT (version 3.1)[25] that provides radiatively corrected cross sections and asymmetries, optionally with cuts applied, for the processes $e^+e^- \to l^+l^-$ and $e^+e^- \to$ hadrons. The calculation used the input parameters: Z^0 mass M_Z, top quark mass M_t, Higgs mass M_H, and the strong coupling constant at the Z^0 pole α_S, together with additional parameters due to the Z′: $M_{Z'}$ and the mixing angle $\theta_{Z'}$.

The data used for the fits were the measurements from 1990 to 1992 of the hadronic cross section and leptonic cross sections and asymmetries for the three flavours, reported in [28], together with the $e^+e^- \to \mu^+\mu^-$ cross section measurements in the energy range 17–86 GeV from the data collected up to and including

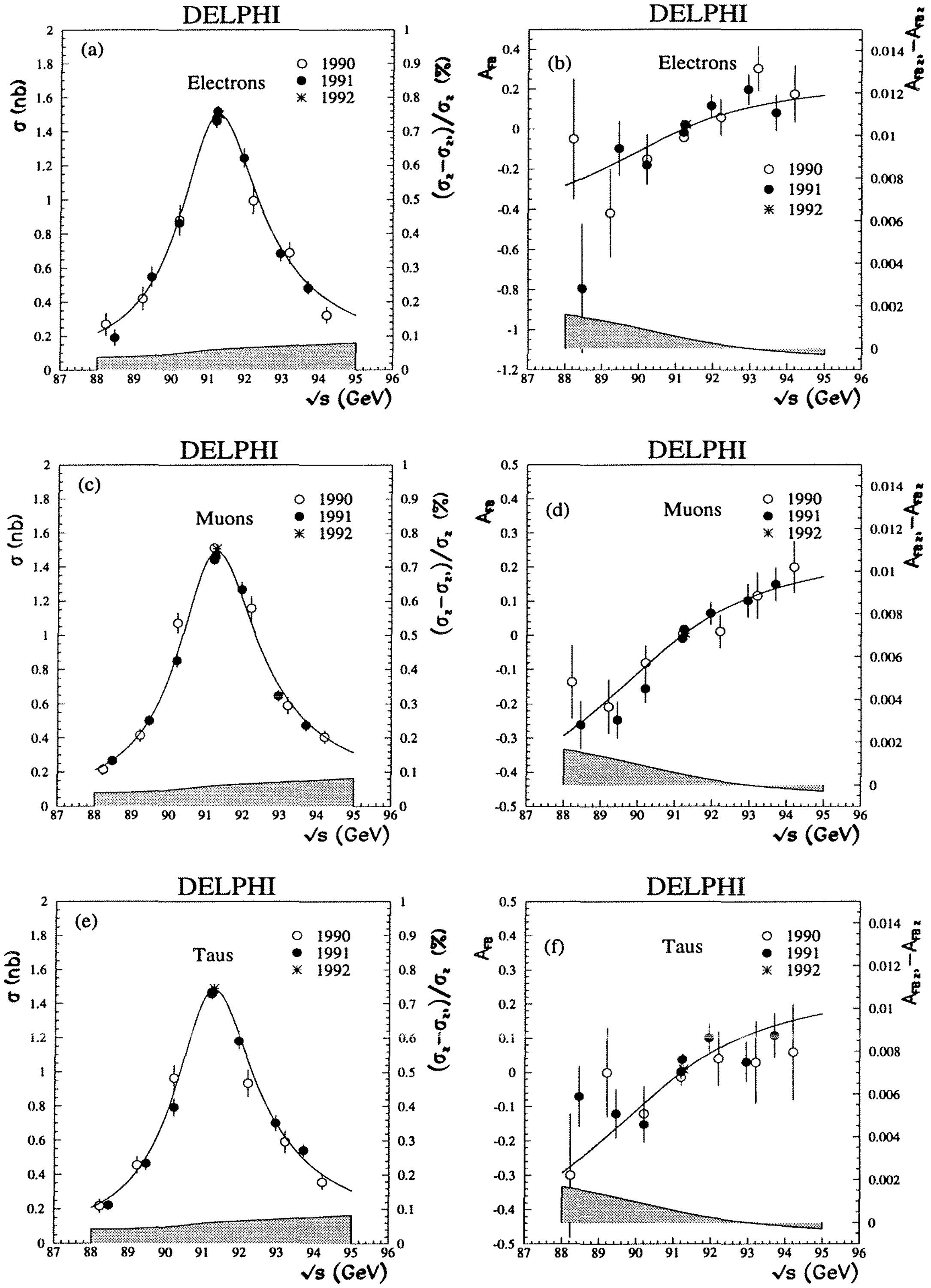

Figure 6.1: Cross sections and asymmetries for e^+e^-, $\mu^+\mu^-$ and $\tau^+\tau^-$ channels, extrapolated to 4π and corrected for the cuts applied. Only statistical errors are shown. The solid line represents the result of the $E_6(\chi)$ fit, with M_t=150 GeV and M_H=300 GeV. The shaded areas with scale to the right, show the differences between the SM fit and the $E_6(\chi)$ fit with M_t=150 GeV and M_H=300 GeV; the percentage difference, $(\sigma_{SM}-\sigma_\chi)/\sigma_{SM}$, is shown for the cross section and the difference $({A_{FB}}^{SM}-{A_{FB}}^{\chi})$ for the asymmetries.

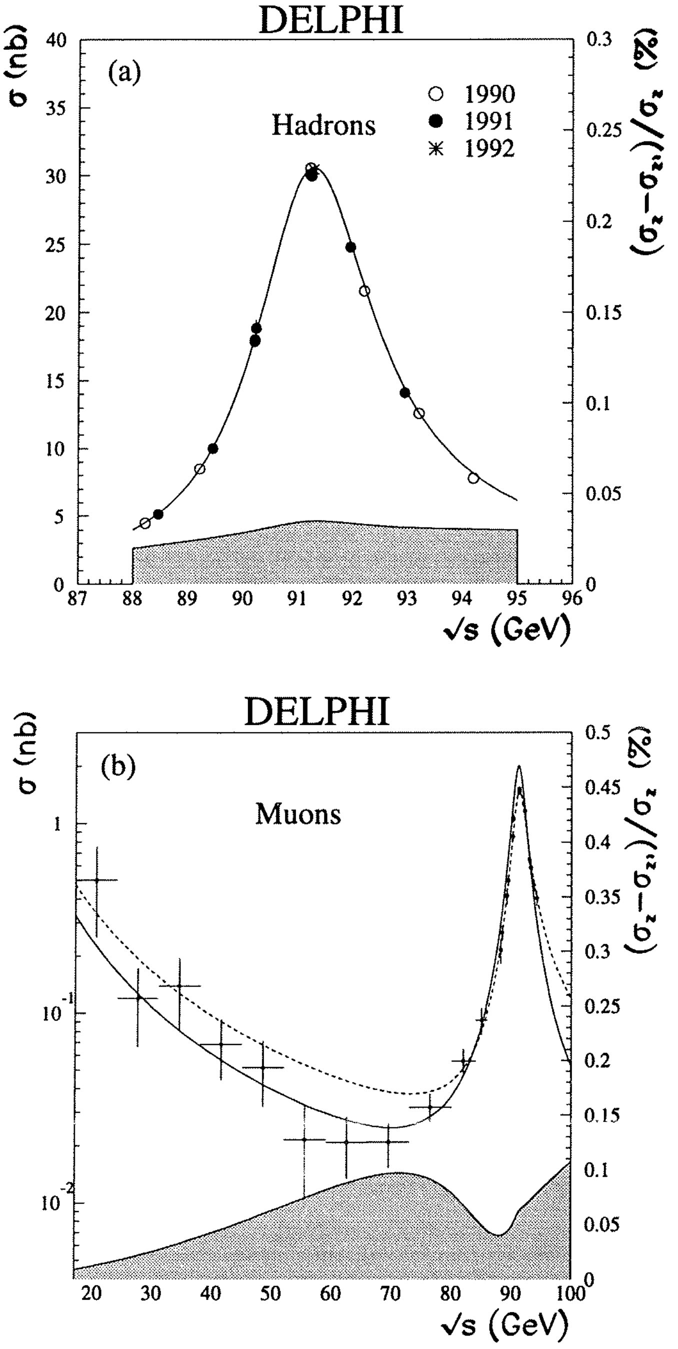

Figure 6.2: (a) Hadronic cross section measurements extrapolated to 4π and corrected for the cuts applied, (b) below peak $\mu^+\mu^-$ channel cross section measurements. For (b), the dashed curve represents the fitted $E_6(\chi)$ QED corrected curve and the solid curve represents the IBA curve (without convolution); both curves obtained from ZFITTER & ZEFIT. Only statistical errors are shown. The shaded areas with scale to the right, show the deviation between SM and $E_6(\chi)$ fit results (with M_t=150 GeV and M_H=300 GeV) as a percentage difference: $(\sigma_{SM} - \sigma_\chi)/\sigma_{SM}$.

1992, as obtained in section 5.12 using selection **B**. The below peak asymmetry measurements were not used in the fits due to the large uncertainty on these measurements compared to the expected deviations in the various models, as presented in section 2.7.

These measurements and the deviations between $E_6(\chi)$ and SM fit results (with M_t=150 GeV and M_H=300 GeV) are presented in figures 6.1 and 6.2. The $E_6(\chi)$ fit results correspond to the first column of table 6.1 and the dashed contour of figure 6.3; with χ^2/ndf = 122.1/121. Equivalent results were obtained from fits performed to data using selection **A**. It was found that the contribution of the low energy cross section measurements to the determination of the models' parameters was small for the E_6 and L-R models, the χ^2 contours only changing slightly with the addition of these data.

To reduce the number of parameters, α_S was fixed at the value determined by the DELPHI experiment [71] of $\alpha_S = 0.123$, and the fits were performed for a series of top quark and Higgs boson masses, $M_t = 100, 150, 200$ GeV and $M_H = 60, 300, 1000$ GeV.

A χ^2 was formed comparing the measured and predicted values of the cross sections and asymmetries. A full covariance matrix treatment of the errors was performed for the on-peak data, with complete account being taken of the LEP energy uncertainties and their point-to-point correlations. As the standard Z^0 mass changes due to the presence of Z', M_Z was left free in the fit, along with the mass and mixing angle of Z'.

The Z^0 mass resulting from the fits was found to deviate from the SM fit result (assuming no Z') by less than 0.004 GeV. For each fit the 95% C.L. allowed region in the $M_{Z'}$,$\theta_{Z'}$ plane was obtained as the region where $\chi^2 < \chi^2_{min} + 5.99$. The results of the fits are presented in Table 6.1 for M_t = 150 GeV and M_H = 300 GeV. The 95% C.L. allowed ranges of $\theta_{Z'}$ are given, and also the lower limits of $M_{Z'}$ for both $\theta_{Z'} = 0$, as well as for any $\theta_{Z'}$. Comparing the results shows that no discrimination between models can be made on the basis of the χ^2, all models giving an acceptable value.

The results for other values of M_t and M_H can be seen on the contour plots of Figures 6.3 and 6.4. The effect of varying the value of α_s in the range $\alpha_s = 0.118$ to 0.128 was found to be small, resulting in a shift in the 95% C.L. contours of less than 0.003 in mixing angle. These results agree with those of an analysis by the L3 collaboration [67].

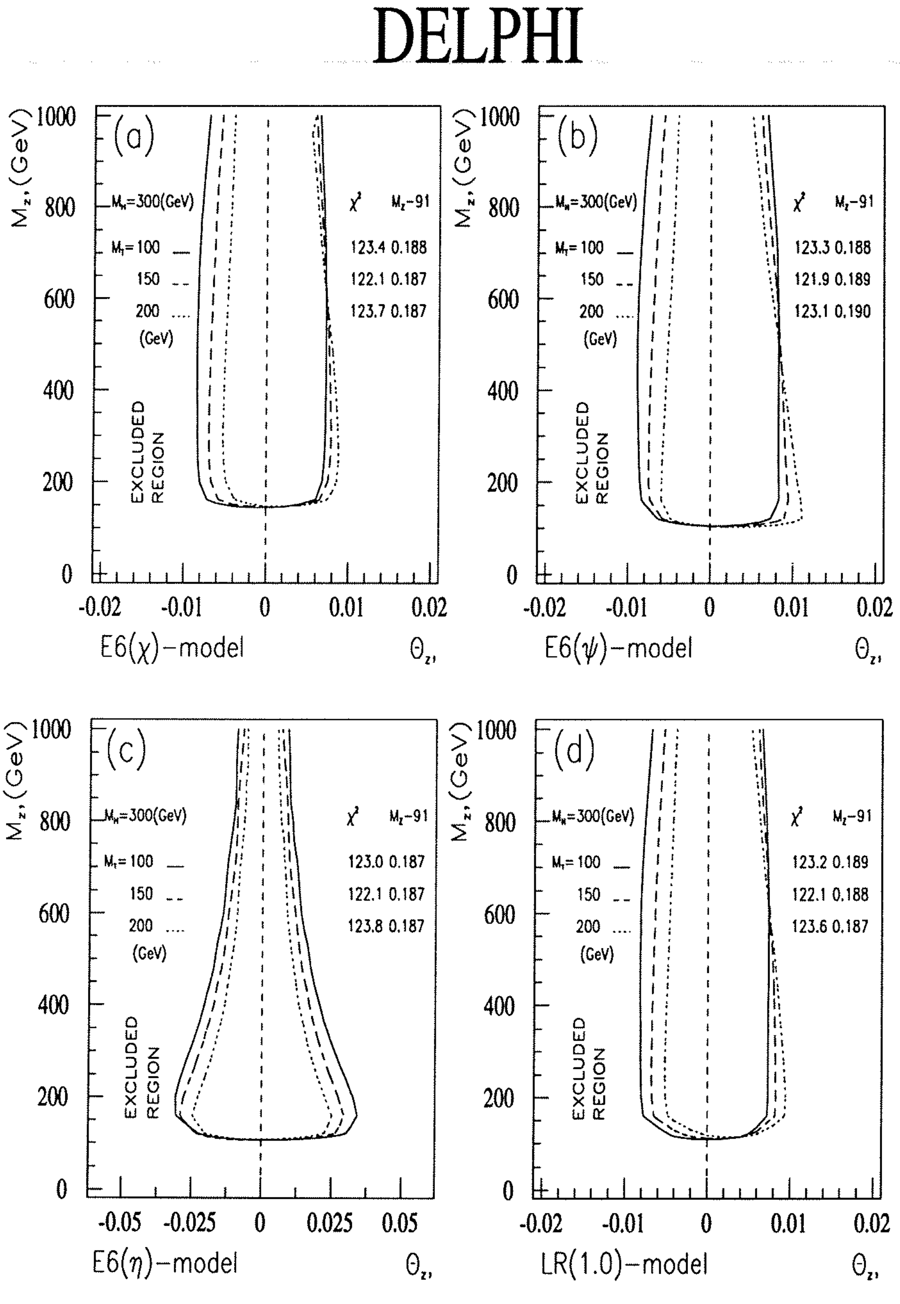

Figure 6.3: Curves corresponding to 95% confidence limits, dividing the $M_{Z'} - \theta_{Z'}$ plane into allowed and excluded regions; for $M_H = 300$ GeV and $M_t = 100, 150, 200$ GeV; all masses are in GeV and angles in radians.

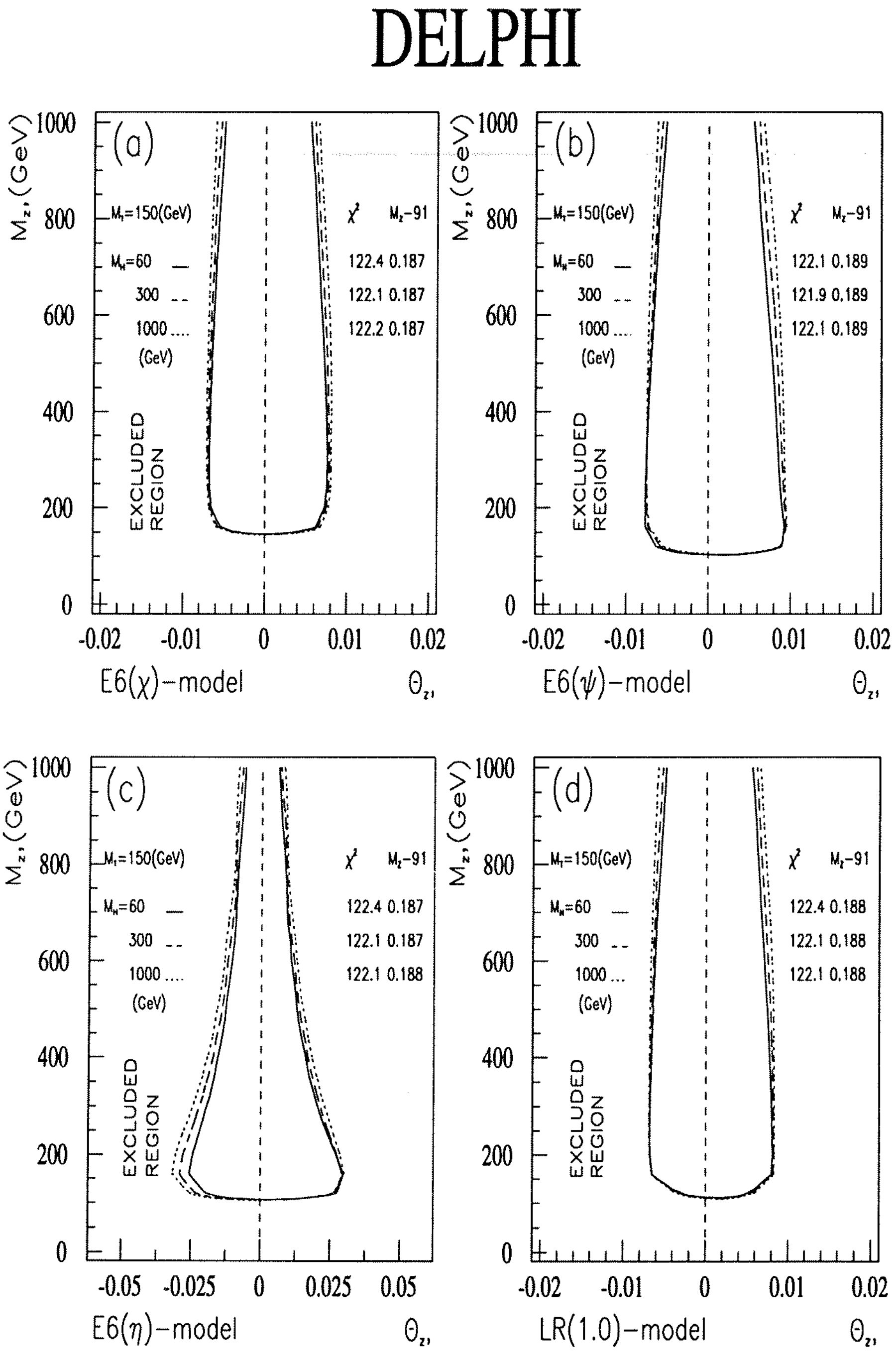

Figure 6.4: Curves corresponding to 95% confidence limits, dividing the $M_{Z'} - \theta_{Z'}$ plane into allowed and excluded regions; for $M_t = 150$ GeV and $M_H = 60, 300, 1000$ GeV; all masses are in GeV and angles in radians.

6.2 Y and Y_L models

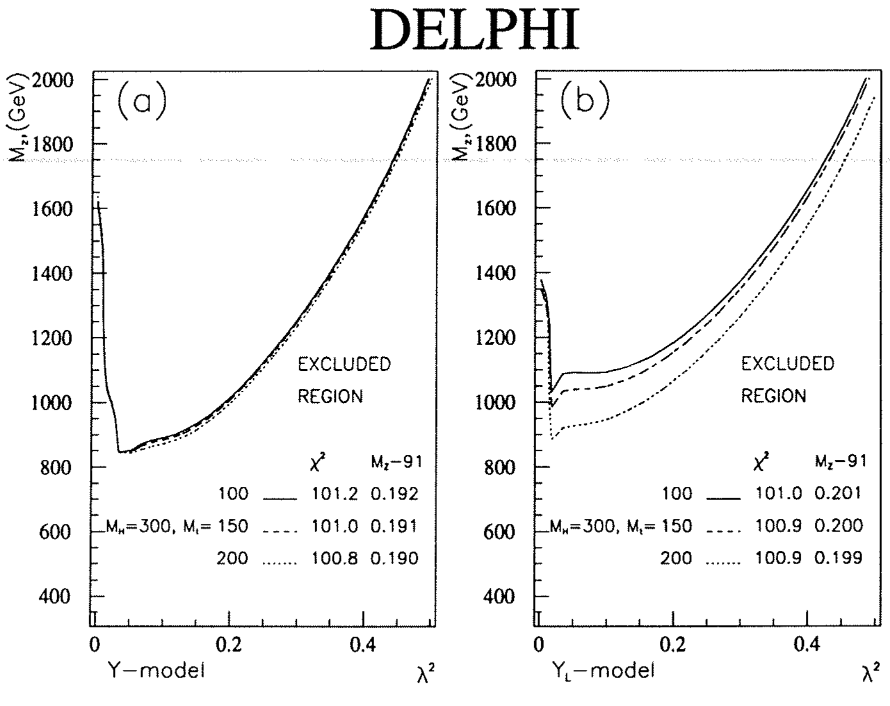

Figure 6.5: Curves corresponding to 95% confidence limits, dividing the $M_{Z'} - \lambda^2_{Y,Y_L}$ plane into allowed and excluded regions; for (a) the Y model and (b) the Y_L model, with $M_H = 300$ GeV and $M_t = 100, 150, 200$ GeV; all masses are in GeV.

Cross section and asymmetry predictions as a function of the parameters of these models were calculated using a software package written by O.Yushchenko [62]. The measurements used in the fits are as described in the previous section, apart from the hadronic cross section measurements, which are excluded due to a limitation of the software package available. All the observed cross sections, with the effects of cuts present, are corrected to be Born level values without cuts, using the SM predictions of ZFITTER without Z' present. An analogous approach to the previous section is used to obtain limits on the additional parameters in these models.

The effects of Z' on the cross section for the Y and Y_L models were calculated in terms of the parameters $M_{Z'}$, the effective coupling λ^2_{Y,Y_L} and M_Z, for a series of values of M_t, M_H and α_S. The Z mass resulting from the fits is found to deviate from the SM fit result (assuming no Z') by about 0.014 GeV for the Y_L model. This relatively large deviation compared to the present error on M_Z occurs due to the hadronic cross section data not being used in this fit. For the Y_L model the inclusion of the low energy cross section measurements was found to change significantly the 95% C.L. contour, for example increasing the $\mathrm{M}_{Z'}$ limit at $\lambda^2_{Y_L} = 0.3$ from 1210 to 1350 GeV and reducing the $\lambda^2_{Y_L}$ limit at $\mathrm{M}_{Z'} = 1200$ GeV from 0.25 to 0.22. There was only a small improvement in the limits for the Y model.

The results are shown in Table 6.1 and Figure 6.5. Both these models yield an acceptable χ^2. The 95% C.L. contours show little dependence on the value of M_t.

6.3 Results

The best fit parameter values and 95% confidence level limits for all the models investigated are collected in table 6.1.

Model	$\mathrm{E}_6(\chi)$	$\mathrm{E}_6(\psi)$	$\mathrm{E}_6(\eta)$	L-R(1.)	L-R($\sqrt{2}$)	Y	Y_L
χ^2	122.1	121.9	122.1	122.1	121.9	101.0	100.9
ndf	121					104	
$\mathrm{M}_{\mathrm{Z}'}$	998.	175.	512.	279.	234.	2400.	1420.
$\theta_{\mathrm{Z}'}$(mrad),λ^2_{Y,Y_L}	0.31	0.96	-1.90	0.63	1.00	0.0046	0.0027
M_{Z}	91.187	91.189	91.187	91.188	91.189	91.191	91.200
$\mathrm{M}_{\mathrm{Z}'} >$	147.	105.	109.	126.	136.	847.	988.
$\mathrm{M}_{\mathrm{Z}'}(\theta_{\mathrm{Z}'} = 0) >$	147.	105.	109.	126.	139.		
$\theta_{\mathrm{Z}'} >$	-0.0070	-0.0075	-0.029	-0.0068	-0.0057		
$\theta_{\mathrm{Z}'} <$	0.0078	0.0095	0.029	0.0082	0.0077		

Table 6.1: 95% confidence-level limits on $\mathrm{M}_{\mathrm{Z}'}$ and $\theta_{\mathrm{Z}'}$ from fits to the predictions of several models, providing the number of degrees of freedom (ndf) and the χ^2 values obtained, together with the best fit values of $\mathrm{M}_{\mathrm{Z}'}$& $\theta_{\mathrm{Z}'}$ or λ^2_{Y,Y_L} as appropriate; all masses are in GeV and angles in radians. The parameter values used are $\mathrm{M}_t = 150$ GeV, $\mathrm{M}_H = 300$ GeV and $\alpha_S = 0.123$.

6.4 Existing Z′ limits

Mass limits

A compilation of mass limits from this and previous analyses is provided in table 6.2. The symbol Z_1 represents an additional gauge boson with the same couplings as the standard Z^0; such a particle is not present in any gauge model but it is useful for comparison purposes. Where L-R is referred to without a parameter value, the L-R($\sqrt{2}$) model is assumed. Best limits are provided by the direct search

	Z_1	$E_6(\chi)$	$E_6(\psi)$	$E_6(\eta)$	L-R
90% C.L.					
UA2('87) $\mathrm{p\bar{p}}$	180				
UA2('93)	252				
UA1('89) $\mathrm{p\bar{p}}$	173				
VENUS('90) e^+e^- [63]	426	231	105	125	
95% C.L.					
CDF('92) $\mathrm{p\bar{p}}$ [64](direct)	412	340	320	340	310
Langacker&Luo('92) [65]	756	322	158	181	389
CHARM2('94) νe [66]	398	262	135	100	253
L3('93) e^+e^- [67]		117	118	100	130
DELPHI('94) e^+e^- [1]		147	105	109	136
TOPAZ('92) e^+e^- [68]	290	146	134	100	
TRISTAN('92) e^+e^- [68]	430	166	245	145	

Table 6.2: 90&95% C.L. lower limits on $M_{Z'}$ in various models; comparing the results of this analysis (the DELPHI values) with previous limits. All masses are in GeV.

for Z′ boson decays to lepton pairs in $\bar{p}p$ collisions performed by the CDF collaboration [64] and the combined analysis of Langacker&Luo discussed in section 6.4, which uses the CDF measurement. The Z′ would be observed directly at CDF as high invariant mass lepton pairs; the invariant mass distributions obtained conform to SM expectations. The low LEP mass limits are due to the almost negligible direct contributions from virtual Z′-exchange for all but the lowest $M_{Z'}$. All the limits presented are without restriction on the Higgs' sector, with the parameter ρ free. As can be seen from expressions 2.14 and 2.15 restricting the Higgs' sector to doublets (setting $\rho = 1$), allows more stringent mass limits to be attained as the restrictions on the mixing angle contribute to the mass limit.

Strong limits, ~1 TeV, on gauge boson masses in E_6 models have been obtained by use of neutrino observations from supernova 1987A [69]. These limits depend on the existence of an almost massless right-handed neutrino, that couples to Z′ and which effects the energetics of supernova collapse.

Mixing angle limits

Deviations from SM expectations in the energy region $\sqrt{s} \sim M_Z$ arise primarily due to the mixing of Z′ and Z^0, as discussed in section 2.6. This makes LEP the ideal environment in which to obtain limits on the Z′-Z^0 mixing angle $\theta_{Z'}$ (defined by equation 2.6). Mixing angle limits from this analysis and previous studies are

		Z_1	$E_6(\chi)$	$E_6(\psi)$	$E_6(\eta)$	L-R
L3('93) e^+e^- [67]	$\theta_{Z'}^{\rm min}$		-0.004	-0.003	-0.029	-0.002
	$\theta_{Z'}^{\rm max}$		0.015	0.020	0.010	0.015
Langacker&Luo [65]	$\theta_{Z'}^{\rm min}$	-0.0087	-0.0070	-0.0060	-0.038	-0.0048
(combined analysis)	$\theta_{Z'}^{\rm max}$	0.0020	0.0094	0.012	0.002	0.0079
DELPHI('94) [1]	$\theta_{Z'}^{\rm min}$		-0.0070	-0.0075	-0.029	-0.0057
(this analysis)	$\theta_{Z'}^{\rm max}$		0.0078	0.0095	0.029	0.0077

Table 6.3: 95% C.L. limits on the lower $\theta_{Z'}^{\rm min}$ and upper $\theta_{Z'}^{\rm max}$ limits on the mixing angle in various models; comparing the results of this analysis with previous limits. All angles are in radians.

presented in table 6.3. The analysis of Langacker&Luo [65] is one of many combined analyses [70] that attempt to obtain the most stringent limits by using all available data, from LEP and CDF together with weak neutral-current, atomic-parity violation and M_W measurements. These combined analyses take an indirect approach, where the data are used to obtain model independent quantities which are then compared to the predictions of Z′ models.

The limit determination presented in this Chapter and in [1], follows a more direct approach, as previously used by L3 [67]. Radiatively corrected cross sections and asymmetries are predicted for the Z′ models allowing direct fits to be made to these observed quantities, so that limits can be placed on the parameters of the models.

Conclusions

The differential cross sections of final state photons as a function of photon energy and of the angle between the photon and the muon are found to conform to Standard Model expectations.

The cross section measurements below the Z^0, in the energy range 17–86 GeV, for the process $e^+e^- \to \mu^+\mu^-$ agree with Standard Model expectations. There are no statistically significant deviations throughout the energy range. The previous cross section measurement in this energy region made by the OPAL collaboration [58] is repeated with 6 times higher statistics.

These measurements, together with the DELPHI cross section and asymmetry measurements at the LEP energies from 1990 to 1992, are used to determine limits on the Z^0-Z' gauge boson mixing angle and on the Z' mass. There is no indication of the existence of a Z'; the mixing angle $\theta_{Z'}$ is consistent with zero for all models. The limits on $\theta_{Z'}$ for the E_6 and L-R models, are consistent with and substantially improve upon the existing limits set by L3 [67] and by the indirect studies [70]. In most cases the 95% confidence level limits on $\theta_{Z'}$ are almost symmetric about zero with $|\theta_{Z'}| < 0.009$. The mass limits for the Y and Y_L models are considerably improved over the existing limit of $M_{Z'} > 250$ GeV [72] to $M_{Z'} > 847$ and 988 GeV respectively.

References

[1] DELPHI Collaboration, P.Abreu et al., "A Study of Radiative Muon-Pair Events at Z^0 Energies and limits on an additional Z' Gauge Boson", preprint CERN PPE 94-121, Submitted to Z. Phys. **C**.

[2] M. Sakuda, "New Results from TRISTAN Experiments", preprint KEK 93-124, Sep 1993.

[3] I.J.R.Aitchison and A.J.G.Hey, "Gauge Theories in Particle Physics", Adam Hilger (1989).
P.B.Renton, "Electroweak Interactions", Cambridge University Press (1990).
F.Mandl and G.Shaw, "Quantum Field Theory", Wiley (1984).

[4] G.'t Hooft, Nuc. Phys. **B35** (1971) 167.

[5] S.L.Glashow, Nuc. Phys. **B22** (1961) 579;
S.Weinberg, Phys. Rev. Lett. **19** (1967) 1264;
A.Salam, in: "Elementary Particle Theory", ed. N.Svartholm, Stockholm (1968), p 367.

[6] Z Physics at LEP 1, Volume 1, edited by G.Altarelli, R.Kleiss and C.-Verzegnassi, CERN 89-08 (1989).

[7] M.Böhm and W.Hollik, "Forward-Backward asymmetries", in [6] p. 203.

[8] M.Consoli and W.Hollik, "Electroweak radiative corrections for Z physics", in [6] p. 7.

[9] F.Berends, "Z line shape", in [6] p. 89.

[10] S.G.Gorishny, A.L.Kataev and S.A.Larin, Phys. Lett. **B259** (1991) 144.;
L.R.Surguladze and M.A.Samuel, Phys. Rev. Lett. bf 66 (1991) 560.

[11] CDF Collaboration, F.Abe et al., "Evidence for Top Quark Production in $\bar{p}p$ Collisions at $\sqrt{s} = 1.8$ TeV", Preprint FERMILAB-PUB-94/097-E.

[12] Particle Data Group, "Review of Particle Properties", Phys. Rev. **D45**, Part 2 (1992).

[13] D.Schaile, "Tests of the Electroweak Theory at LEP", Preprint CERN PPE 93-213.

[14] ZFITTER is a package, produced by the Dubna-Zeuthen radiative correction group, for fitting Z^0 data in either a quasi-model independent way or within the MSM.
D.Bardin et al., Phys. Lett. **B229** (1989) 405;

[15] "Unity of Forces in the Universe", ed. A.Zee, World Scientific, Singapore, 1982.

[16] H.E.Haber and G.L.Kane, "The search for supersymmetry", Phys.Rep.C117 (1985) p. 75.
"Supersymmetry", ed. S.Ferrara, North Holland, Amsterdam and World Scientific, Singapore, 1987.

[17] Z Physics at LEP 1, Volume 2, edited by G.Altarelli, R.Kleiss and C.-Verzegnassi, CERN 89-08 (1989).

[18] F.Boudjema and F.M.Renard, "Compositeness", in [17] p. 182.

[19] S.S.Gershtein, A.A.Likhoded, A.A.Pankov and O.P.Yushchenko, "Effects of additional isoscalar vector bosons in $e^+e^- \to f\bar{f}$ processes at the TRISTAN and LEP energies", Z.Phys.**C56** (1992) 279;
U.Baur, M.Linder and K.H.Schwarzer, "Testing the Standard Model versus a composite structure of weak interactions in high precision experiments at LEP and SLC" Nucl.Phys.**B291** (1987) 1;
M.Kuroda, D.Schildknecht and K.H.Schwarzer, "Phenomenology of weak isoscalar vector bosons" Nucl.Phys.**B261** (1985) 432.

[20] "Superstrings", ed. J.H.Schwartz, World Scientific, Singapore, 1985.

[21] "Beyond the Standard Model", L.Ibanez p.131 in Proc. CERN School of Physics (1990)

[22] D.London and J.L.Rosner, "Extra gauge bosons in E_6", Phys.Rev.**D34** (1986) 1530.

[23] R.W.Robinett, J.L.Rosner, Phys.Rev.**D25** (1982) 3036;
C.N.Leung, J.L.Rosner, Phys.Rev.**D29** (1982) 2132.

[24] J.Maalampi, "Signatures of left-right symmetry at high energies", Proceedings, Helsinki University preprint, HU TFT 93-51.

[25] A.Leike, S. Riemann and T. Riemann, Munich University preprint LMU-91/06, and FORTRAN program ZEFIT; and Phys. Lett. **B291** (1992) 187.

[26] P.B.Renton, Z.Phys. **C56** (1992) 355;

[27] DELPHI Collaboration, P. Abreu et al., "Determination of Z^0 resonance parameters and couplings from its hadronic and leptonic decays", Nucl. Phys. **B367** (1991) 511.

[28] DELPHI Collaboration, P. Abreu et al., "Measurements of the Lineshape of the Z^0 and Determination of Electroweak Parameters from its Hadronic and Leptonic Decays", preprint CERN PPE 94-08, submitted to Nucl. Phys **B**.

[29] DELPHI Collaboration, P. Abreu et al., "Improved measurements of cross sections and asymmetries at the Z^0 resonance", preprint CERN PPE 94-31, to be published in Nucl. Phys.**B**

[30] S. Myers, "The LEP Collider, from Design to Approval and Commissioning", CERN 91-08.

[31] The LEP injector study group, LEP Design Reports -
"Vol I - The LEP Injector Chain", CERN-LEP/TH/83-29, and
"Vol II - The LEP Main Ring", CERN-LEP/84-01.

[32] The Working Group on LEP Energy, L. Arnaudon et al., "Measurement of the mass of the Z boson and the energy calibration of LEP", Phys. Lett., **B307** (1993) p 187;
"The energy calibration of LEP in 1991", CERN PPE 92-125

[33] DELPHI Collaboration, P. Aarnio et al., Nucl. Instr. & Meth. **A303** (1991) 233.

[34] DELPHI Collaboration, N. Bingefors et al., "The DELPHI microvertex detector", Nucl. Instr. & Meth. **A328** (1993) 447.

[35] F. Hartjes et al., "A drift chamber with variable drift velocity", Nucl. Instr. & Meth. **A256** (1987) 55.

[36] C. Brand et al., "The DELPHI time projection chamber", Nucl. Instr. & Meth. **A283** (1989) 567.

[37] A. Amery et al., “The DELPHI Outer Detector”, Nucl. Instr. & Meth. **A283** (1989) 502.

[38] DELPHI Collaboration, “DELPHI Technical Proposal”, DELPHI 83-66.

[39] DELPHI Collaboration, P.Abreu et al., “A measurement of the mean lifetimes of the charged and neutral B-hadrons”, Phys. Lett. **B312** (1993) 253.

[40] DELPHI Collaboration, D. Johnson, D. Reid and W. Trischuk, “A beamspot Database for Lifetime Measurements”, DELPHI 92-36 PHYS 168 (Geneva, 18 March 1992)

[41] K. Kleinknecht, “Detectors for particle radiation”, Cambridge University Press.

[42] DELPHI Collaboration, M.Feindt & O.Podobrin, “PXPHOT - Third Stage Pattern Recognition for DELPHI’, in prepartion.

[43] R.C. Fernow, “Introduction to experimental particle physics”, Cambridge University Press.

[44] DELPHI Collaboration, “DELPHI Data Analysis Program (DELANA) User's Guide”, DELPHI 89 - 44 PROG 137 (1989).

[45] “TANAGRA User's Guide”, DELPHI 87–95 PROG 98.

[46] Y. Sacquin, “DELPHI DST Content Version 2.80”, DELPHI 91 - 22 PROG 161 Rev3, November 1992.

[47] DELPHI Collaboration, “DELSIM: DELPHI Event Generation and Detector Simulation — User's Guide”, DELPHI 89 - 67 PROG 142 (1989).

[48] J.E. Campagne and R. Zitoun, Z. Phys. **C43** (1989) 469; and Proc. of the Brighton Workshop on Radiative Corrections, Sussex, July 1989.

[49] S. Jadach et al., “The Monte Carlo program KORALZ, version 4.0, for the lepton or quark pair production at LEP/SLC energies” CERN TH 7075-93 (1993). Submitted to Comput. Phys. Commun.

[50] T. Sjostrand, Comput. Phys. Commun. **28** (1983) 227;
T. Sjostrand, Comput. Phys. Commun. **39** (1986) 347.

[51] B. van Eijk, “EURODEC User Manual Version 2.3”, DELPHI 89-39 PROG 136 (1989).

[52] J. Wickens, “DELANA Tags for 1991 Data”, DELPHI 91-20 PROG 160 (1991).

[53] J. Wickens, "Physics Team Tagging in PXTAG", DELPHI 92-44 PROG 184 (1992).

[54] DELPHI Collaboration, P. Abreu et al., "A Measurement of the Tau Lifetime", preprint CERN PPE 93-12, to be published in Phys. Lett. **B**

[55] C.J.Beeston, "A Study of the Reaction $e^+e^- \to \mu^+\mu^-$ Around the Z^0 Pole", Oxford University, D.Phil. Thesis (1992).

[56] R.Lindner, private communication.

[57] HPC Group, "Pattern Recognition and Reconstruction of Photons and Charged Particles using the HPC Electromagnetic Calorimeter in the DELPHI Detector", DELPHI 91-39 PROG 174.

[58] OPAL Collaboration, D.P.Acton et al., "A measurement of photon radiation in lepton pair events from Z^0 decays", Phys. Lett. **B273** (1991) 338.

[59] Z.Was and S.Jadach, Phys. Rev. **D41** (1990) 1425.

[60] TOPAZ Collaboration, B. Howell et al., "Cross sections and charge asymmetries for $e^+e^- \to \mu^+\mu^-$ and $e^+e^- \to \tau^+\tau^-$ reactions at $\sqrt{s}$=52-61.4 GeV", Phys. Lett. **B291** (1992) 206.

[61] D.S. Koltick, "Precision measurement of the total cross section and charge asymmetry at TOPAZ for $e^+e^- \to \mu^+\mu^-$ and $e^+e^- \to \tau^+\tau^-$", American Institute of Physics, Conference proceedings, Dallas (1992), p716.

[62] Oleg Iouchtchenko (Email: ioucht@vxcern.cern.ch, Institute: IHEP Serpukhov), private communication.

[63] VENUS Collaboration, K.Abe et al., "Experimental limits on extra Z bosons from e^+e^- annihilation data with the VENUS detector at $\sqrt{s}$=50-64 GeV", Phys. Lett. **B246** (1990), 297.

[64] CDF Collaboration, F. Abe et al., Phys. Rev. Lett. **68** (1992) 1463.

[65] P.Langacker and M.Luo, "Constraints on additional Z bosons", Phys. Rev. **D45** (1992) 278.

[66] CHARM2 Collaboration, P.Vilain et al., "Constraints on Additional Z Bosons Derived from Neutrino-Electron Scattering Measurements", preprint CERN PPE 94-80.

[67] L3 Collaboration, O. Adriani et al., "Search for a Z′ at the Z Resonance", Phys. Lett. **B306** (1993) 187.

[68] B.L. Howell, "Measurement of $e^+e^- \to \mu^+\mu^-$ and $e^+e^- \to \tau^+\tau^-$ Processes with the TOPAZ Detector", KEK-Proceedings 93-2, p 13.

[69] J.A.Grifols, E.Masso and T.G.Rizzo, "Mass bounds on new neutral gauge bosons in E_6 models from SN 1987A data", Phys. Rev. **D42** (1990), 3293.

[70] G.Altarelli, Phys. Lett., **B318** (1993) 139;
P.B.Renton, Z.Phys. **C56** (1992) 355;
E.Nardi, E.Roulet and D.Tommasini, Phys. Rev. **D46** (1992) 3040;
F. del Aguila, W.Hollik, J.M.Moreno and M.Quiros, Nucl. Phys. **B372** (1992) 1;
M.C.Gonzalez-Garcia and J.W.F.Valle, Phys. Lett. **B259** (1991) 365;

[71] DELPHI Collaboration, P. Abreu et al., Z. Phys. **C59** (1993) 21.

[72] M.Kuroda, D.Schildknecht and K.H.Schwarzer, Nucl. Phys. **B261** (1985) 432.

[73] W.T.Eadie et al. Statistical Methods in Experimental Physics, p.166;
N.J. Kjaer and R. Moller, "Reconstruction of invariant masses in multi-jet events", DELPHI 91-17 PHYS 88.

Appendix A

DELPHI Members

P.Abreu[20], W.Adam[7], T.Adye[37], E.Agasi[30], I.Ajinenko[43], R.Aleksan[39], G.D.Alekseev[14], A.Algeri[13], S.Almehed[23], S.J.Alvsvaag[4], U.Amaldi[7], A.Andreazza[27], P.Antilogus[24], W-D.Apel[15], R.J.Apsimon[37], Y.Arnoud[39], B.Åsman[45], J-E.Augustin[18], A.Augustinus[30], P.Baillon[7], P.Bambade[18], F.Barao[20], R.Barate[12], G.Barbiellini[47], D.Y.Bardin[14], G.J.Barker[34], A.Baroncelli[41], O.Barring[7], J.A.Barrio[25], W.Bartl[50], M.J.Bates[37], M.Battaglia[13], M.Baubillier[22], K-H.Becks[52], M.Begalli[36], P.Beilliere[6], Yu.Belokopytov[43], P.Beltran[9], D.Benedic[8], A.C.Benvenuti[5], M.Berggren[18], D.Bertrand[2], F.Bianchi[46], M.Bigi[46], M.S.Bilenky[14], P.Billoir[22], J.Bjarne[23], D.Bloch[8], J.Blocki[51], S.Blyth[34], V.Bocci[38], P.N.Bogolubov[14], T.Bolognese[39], M.Bonesini[27], W.Bonivento[27], P.S.L.Booth[21], G.Borisov[43], H.Borner[7], C.Bosio[41], B.Bostjancic[44], S.Bosworth[34], O.Botner[48], B.Bouquet[18], C.Bourdarios[18], T.J.V.Bowcock[21], M.Bozzo[11], S.Braibant[2], P.Branchini[41], K.D.Brand[35], R.A.Brenner[7], H.Briand[22], C.Bricman[2], L.Brillault[22], R.C.A.Brown[7], J-M.Brunet[6], L.Bugge[32], T.Buran[32], H.Burmeister[7], A.Buys[7], J.A.M.A.Buytaert[7], M.Caccia[7], M.Calvi[27], A.J.Camacho Rozas[42], R.Campion[21], T.Camporesi[7], V.Canale[38], K.Cankocak[45], F.Cao[2], F.Carena[7], L.Carroll[21], C.Caso[11], M.V.Castillo Gimenez[49], A.Cattai[7], F.R.Cavallo[5], L.Cerrito[38], V.Chabaud[7], A.Chan[1], M.Chapkin[43], Ph.Charpentier[7], J.Chauveau[22], P.Checchia[35], G.A.Chelkov[14], L.Chevalier[39], P.Chliapnikov[43], V.Chorowicz[22], J.T.M.Chrin[49], V.Cindro[44], P.Collins[34], J.L.Contreras[18], R.Contri[11], E.Cortina[49], G.Cosme[18], F.Couchot[18], H.B.Crawley[1], D.Crennell[37], G.Crosetti[11], J.Cuevas Maestro[33], S.Czellar[13], E.Dahl-Jensen[28], J.Dahm[52], B.Dalmagne[18], M.Dam[32], G.Damgaard[28], E.Daubie[2], A.Daum[15], P.D.Dauncey[34], M.Davenport[7], J.Davies[21], W.Da Silva[22], C.Defoix[6], P.Delpierre[26], N.Demaria[46], A.De Angelis[7], H.De Boeck[2], W.De Boer[15], S.De Brabandere[2], C.De Clercq[2], M.D.M.De Fez Laso[49], C.De La Vaissiere[22], B.De Lotto[47], A.De Min[27], H.Dijkstra[7], L.Di Ciaccio[38], J.Dolbeau[6], M.Donszelmann[7], K.Doroba[51], M.Dracos[7], J.Drees[52], M.Dris[31], Y.Dufour[7], F.Dupont[12], D.Edsall[1], L-O.Eek[48], P.A.-M.Eerola[7], R.Ehret[15], T.Ekelof[48], G.Ekspong[45], A.Elliot Peisert[35], M.Elsing[52], J-P.Engel[8], N.Ershaidat[22], M.Espirito Santo[20], D.Fassouliotis[31], M.Feindt[7], A.Fenyuk[43], A.Ferrer[49], T.A.Filippas[31], A.Firestone[1], H.Foeth[7], E.Fokitis[31], F.Fontanelli[11], K.A.J.Forbes[21], J-L.Fousset[26], S.Francon[24], B.Franek[37], P.Frenkiel[6], D.C.Fries[15], A.G.Frodesen[4], R.Fruhwirth[50], F.Fulda-Quenzer[18], H.Furstenau[15], J.Fuster[7], D.Gamba[46], M.Gandelman[17], C.Garcia[49], J.Garcia[42], C.Gaspar[7], U.Gasparini[35], Ph.Gavillet[7], E.N.Gazis[31], J-P.Gerber[8], P.Giacomelli[7], D.Gillespie[7], R.Gokieli[51], B.Golob[44], V.M.Golovatyuk[14], J.J.Gomez Y Cadenas[7], G.Gopal[37], L.Gorn[1], M.Gorski[51], V.Gracco[11], A.Grant[7], F.Grard[2], E.Graziani[41], G.Grosdidier[18], E.Gross[7], B.Grossetete[22], P.Gunnarsson[45], J.Guy[37], U.Haedinger[15], F.Hahn[52], M.Hahn[45], S.Hahn[52], S.Haider[30], Z.Hajduk[16], A.Hakansson[23], A.Hallgren[48], K.Hamacher[52], G.Hamel De Monchenault[39], W.Hao[30], F.J.Harris[34], V.Hedberg[23], T.Henkes[7], R.Henriques[20], J.J.Hernandez[49], J.A.Hernando[49], P.Herquet[2], H.Herr[7], T.L.Hessing[21], I.Hietanen[13], C.O.Higgins[21], E.Higon[49], H.J.Hilke[7], T.S.Hill[1], S.D.Hodgson[34], T.Hofmokl[51], S-O.Holmgren[45], P.J.Holt[34], D.Holthuizen[30], P.F.Honore[6], M.Houlden[21], J.Hrubec[50], K.Huet[2], K.Hultqvist[45], P.Ioannou[3], P-S.Iversen[4], J.N.Jackson[21], R.Jacobsson[45], P.Jalocha[16], G.Jarlskog[23], P.Jarry[39], B.Jean-Marie[18], E.K.Johansson[45], M.Jonker[7], L.Jonsson[23], P.Juillot[8], G.Kalkanis[3], G.Kalmus[37], F.Kapusta[22], M.Karlsson[45], E.Karvelas[9], S.Katsanevas[3], E.C.Katsoufis[31], R.Keranen[7], B.A.Khomenko[14], N.N.Khovanski[14], B.King[21], N.J.Kjaer[7], H.Klein[7], A.Klovning[4], P.Kluit[30], A.Koch-Mehrin[52], J.H.Koehne[15], B.Koene[30], P.Kokkinias[9], M.Koratzinos[32], K.Korcyl[16], A.V.Korytov[14], V.Kostioukhine[43], C.Kourkoumelis[3], O.Kouznetsov[14], P.H.Kramer[52], M.Krammer[50], C.Kreuter[15], J.Krolikowski[51], I.Kronkvist[23], W.Krupinski[16], K.Kulka[48], K.Kurvinen[13], C.Lacasta[49], C.Lambropoulos[9], J.W.Lamsa[1], L.Lanceri[47], P.Langefeld[52], V.Lapin[43], I.Last[21], J-P.Laugier[39], R.Lauhakangas[13], G.Leder[50], F.Ledroit[12], R.Leitner[29], Y.Lemoigne[39], J.Lemonne[2], G.Lenzen[52], V.Lepeltier[18], T.Lesiak[16], J.M.Levy[8], E.Lieb[52], D.Liko[50], J.Lindgren[13], R.Lindner[52], A.Lipniacka[18], I.Lippi[35], B.Loerstad[23], M.Lokajicek[10], J.G.Loken[34], A.Lopez-Fernandez[7], M.A.Lopez Aguera[42], M.Los[30], D.Loukas[9], J.J.Lozano[49], P.Lutz[6], L.Lyons[34], G.Maehlum[32], J.Maillard[6], A.Maio[20], A.Maltezos[9], F.Mandl[50], J.Marco[42], M.Margoni[35], J-C.Marin[7], C.Mariotti[41], A.Markou[9], T.Maron[52], S.Marti[49], C.Martinez-Rivero[42], F.Martinez-Vidal[49], F.Matorras[42], C.Matteuzzi[27], G.Matthiae[38], M.Mazzucato[35], M.Mc Cubbin[21], R.Mc Kay[1], R.Mc Nulty[21], J.Medbo[48], C.Meroni[27], W.T.Meyer[1], M.Michelotto[35], I.Mikulec[50], L.Mirabito[24], W.A.Mitaroff[50], G.V.Mitselmakher[14], U.Mjoernmark[23], T.Moa[45], R.Moeller[28], K.Moenig[7], M.R.Monge[11], P.Morettini[11], H.Mueller[15], W.J.Murray[37], B.Muryn[16], G.Myatt[34], F.Naraghi[12], F.L.Navarria[5], P.Negri[27], S.Nemecek[10], W.Neumann[52], R.Nicolaidou[3], B.S.Nielsen[28], B.Nijjhar[21], V.Nikolaenko[43], P.E.S.Nilsen[4], P.Niss[45], A.Nomerotski[35], V.Obraztsov[43], A.G.Olshevski[14], R.Orava[13], A.Ostankov[43], K.Osterberg[13], A.Ouraou[39], P.Paganini[18], M.Paganoni[27], R.Pain[22], H.Palka[16], Th.D.Papadopoulou[31], L.Pape[7], F.Parodi[11], A.Passeri[41], M.Pegoraro[35], J.Pennanen[13], L.Peralta[20], H.Pernegger[50], M.Pernicka[50], A.Perrotta[5], C.Petridou[47], A.Petrolini[11], G.Piana[11], F.Pierre[39], M.Pimenta[20], S.Plaszczynski[18], O.Podobrin[15], M.E.Pol[17], G.Polok[16], P.Poropat[47], V.Pozdniakov[14], P.Privitera[38], A.Pullia[27], D.Radojicic[34], S.Ragazzi[27], H.Rahmani[31], J.Rames[10], P.N.Ratoff[19], A.L.Read[32], M.Reale[52], P.Rebecchi[18], N.G.Redaelli[27], M.Regler[50], D.Reid[7], P.B.Renton[34], L.K.Resvanis[3], F.Richard[18], J.Richardson[21], J.Ridky[10], G.Rinaudo[46], A.Romero[46], I.Roncagliolo[11], P.Ronchese[35], C.Ronnqvist[13], E.I.Rosenberg[1], E.Rosso[7], P.Roudeau[18], T.Rovelli[5], W.Ruckstuhl[30], V.Ruhlmann-Kleider[39], A.Ruiz[42], K.Rybicki[16], H.Saarikko[13], Y.Sacquin[39], G.Sajot[12], J.Salt[49], J.Sanchez[25], M.Sannino[11,40], S.Schael[7], H.Schneider[15], M.A.E.Schyns[52], G.Sciolla[46], F.Scuri[47], A.M.Segar[34], A.Seitz[15], R.Sekulin[37], M.Sessa[47], R.Seufert[15], R.C.Shellard[36], I.Siccama[30], P.Siegrist[39], S.Simonetti[11], F.Simonetto[35], A.N.Sisakian[14], G.Skjevling[32], G.Smadja[39,24], N.Smirnov[43], O.Smirnova[14], G.R.Smith[37], R.Sosnowski[51], D.Souza-Santos[36], T.Spassov[20], E.Spiriti[41], S.Squarcia[11], H.Staeck[52], C.Stanescu[41], S.Stapnes[32], G.Stavropoulos[9], F.Stichelbaut[2], A.Stocchi[18], J.Strauss[50], J.Straver[7], R.Strub[8], B.Stugu[4], M.Szczekowski[7], M.Szeptycka[51], P.Szymanski[51], T.Tabarelli[27], O.Tchikilev[43], G.E.Theodosiou[9], A.Tilquin[26], J.Timmermans[30], V.G.Timofeev[14], L.G.Tkatchev[14], T.Todorov[8], D.Z.Toet[30], O.Toker[13], A.Tomaradze[2], B.Tome[20], E.Torassa[46], L.Tortora[41], D.Treille[7], W.Trischuk[7], G.Tristram[6], C.Troncon[27], A.Tsirou[7], E.N.Tsyganov[14], M.Turala[16], M-L.Turluer[39], T.Tuuva[13], I.A.Tyapkin[22], M.Tyndel[37], S.Tzamarias[21], B.Ueberschaer[52], S.Ueberschaer[52], O.Ullaland[7], V.Uvarov[43], G.Valenti[5], E.Vallazza[7], J.A.Valls Ferrer[49], C.Vander Velde[2], G.W.Van Apeldoorn[30], P.Van Dam[30], M.Van Der Heijden[30], W.K.Van Doninck[2], J.Van Eldik[30], P.Vaz[7], G.Vegni[27], L.Ventura[35], W.Venus[37], F.Verbeure[2], M.Verlato[35], L.S.Vertogradov[14], D.Vilanova[39], P.Vincent[24], L.Vitale[47], E.Vlasov[43], A.S.Vodopyanov[14], M.Vollmer[52], M.Voutilainen[13], V.Vrba[41], H.Wahlen[52], C.Walck[45], F.Waldner[47], A.Wehr[52], M.Weierstall[52], P.Weilhammer[7], A.M.Wetherell[7], J.H.Wickens[2], M.Wielers[15], G.R.Wilkinson[34], W.S.C.Williams[34], M.Winter[8], M.Witek[16], G.Wormser[18], K.Woschnagg[48], A.Zaitsev[43], A.Zalewska[16], D.Zavrtanik[44], E.Zevgolatakos[9], N.I.Zimin[14], M.Zito[39], D.Zontar[44], R.Zuberi[34], G.Zumerle[35], J.Zuniga[49]

---

[1] Ames Lab. and Dept. of Physics, Iowa State University, Ames IA 50011, USA
[2] Physics Dept., Univ. Instelling Antwerpen, Universiteitsplein 1, B-2610 Wilrijk, Belgium and IIHE, ULB-VUB, Pleinlaan 2, B-1050 Brussels, Belgium
[3] Physics Laboratory, University of Athens, Solonos Str. 104, GR-10680 Athens, Greece
[4] Department of Physics, University of Bergen, Allégaten 55, N-5007 Bergen, Norway
[5] Dipartimento di Fisica, Università di Bologna and INFN, Via Irnerio 46, Bologna, Italy
[6] Collège de France, Lab. de Physique Corpusculaire, F-75231 Paris Cedex 05, France
[7] CERN, CH-1211 Geneva 23, Switzerland
[8] Centre de Recherche Nucléaire, F-67037 Strasbourg Cedex, France
[9] Institute of Nuclear Physics, N.C.S.R. Demokritos, GR-15310 Athens, Greece
[10] FZU, Inst. of Physics of the C.A.S. High Energy Physics Division, Czechoslovakia
[11] Dipartimento di Fisica, Università di Genova and INFN, Genova, Italy
[12] Institut des Sciences Nucléaires, Université de Grenoble 1, Grenoble, France
[13] Research Institute for High Energy Physics, SEFT, University of Helsinki, Finland
[14] Joint Institute for Nuclear Research, Dubna, Moscow, Russian Federation
[15] Institut für Experimentelle Kernphysik, Universität Karlsruhe, Karlsruhe, Germany
[16] High Energy Physics Lab., Institute of Nuclear Physics, Krakow, Poland
[17] Centro Brasileiro de Pesquisas Físicas, rua Xavier Sigaud 150, Rio de Janeiro, Brazil
[18] Université de Paris-Sud, Lab. de l'Accélérateur Linéaire, F-91405 Orsay, France
[19] School of Physics and Materials, University of Lancaster, GB-Lancaster LA1 4YB, UK
[20] LIP, IST, FCUL - Av. Elias Garcia, 14-1°, P-1000 Lisboa Codex, Portugal
[21] Dept. of Physics, University of Liverpool, P.O. Box 147, GB-Liverpool L69 3BX, UK
[22] LPNHE, Universités Paris VI et VII, 4 place Jussieu, Paris, France
[23] Department of Physics, University of Lund, Sölvegatan 14, S-22363 Lund, Sweden
[24] Université Claude Bernard de Lyon, IPNL, F-69622 Villeurbanne Cedex, France
[25] Universidad Complutense, Avda. Complutense s/n, E-28040 Madrid, Spain
[26] Univ. d'Aix - Marseille II - CPP, F-13288 Marseille Cedex 09, France
[27] Dipartimento di Fisica, Università di Milano and INFN, Via Celoria 16, Milan, Italy
[28] Niels Bohr Institute, Blegdamsvej 17, DK-2100 Copenhagen 0, Denmark
[29] NC, Nuclear Centre of MFF, Charles University, Areal MFF, Praha 8, Czechoslovakia
[30] NIKHEF-H, Postbus 41882, NL-1009 DB Amsterdam, The Netherlands
[31] National Technical University, Physics Department, GR-15773 Athens, Greece
[32] Physics Department, University of Oslo, Blindern, N-1000 Oslo 3, Norway
[33] Dpto. Fisica, Univ. Oviedo, C/P.Jimenez Casas, S/N-33006 Oviedo, Spain
[34] Department of Physics, University of Oxford, Keble Road, Oxford OX1 3RH, UK
[35] Dipartimento di Fisica, Università di Padova and INFN, Via Marzolo 8, Padua, Italy
[36] Depto. de Fisica, Pontificia Univ. Católica, C.P. 38071 RJ-22453 Rio de Janeiro, Brazil
[37] Rutherford Appleton Laboratory, Chilton, GB - Didcot OX11 OQX, UK
[38] Dipartimento di Fisica, Università di Roma II and INFN, Tor Vergata, Rome, Italy
[39] Centre d'Etude de Saclay, DSM/DAPNIA, F-91191 Gif-sur-Yvette Cedex, France
[40] Dipartimento di Fisica-Università di Salerno, I-84100 Salerno, Italy
[41] Istituto Superiore di Sanità, INFN, Viale Regina Elena 299, I-00161 Rome, Italy
[42] C.E.A.F.M., C.S.I.C. - Univ. Cantabria, Avda. los Castros, S/N-39006 Santander, Spain
[43] Inst. for High Energy Physics, Serpukov P.O. Box 35, Protvino, Russian Federation
[44] J. Stefan Institute and Dept. of Physics, University of Ljubljana, Ljubljana, Slovenia
[45] Fysikum, Stockholm University, Box 6730, S-113 85 Stockholm, Sweden
[46] Dipartimento di Fisica Sperimentale, Università di Torino and INFN, Turin, Italy
[47] Dipartimento di Fisica, Università di Trieste and INFN, Trieste, Italy
[48] Department of Radiation Sciences, University of Uppsala, P.O. Box 535, Uppsala, Sweden
[49] IFIC, Valencia-CSIC, and D.F.A.M.N., U. de Valencia, Burjassot (Valencia), Spain
[50] Institut für Hochenergiephysik, Österr. Akad. d. Wissensch., A-1050 Vienna, Austria
[51] Inst. Nuclear Studies and University of Warsaw, Ul. Hoza 69, PL-00681 Warsaw, Poland
[52] Fachbereich Physik, University of Wuppertal, Wuppertal, Germany

Appendix B

DELPHI Coordinate System

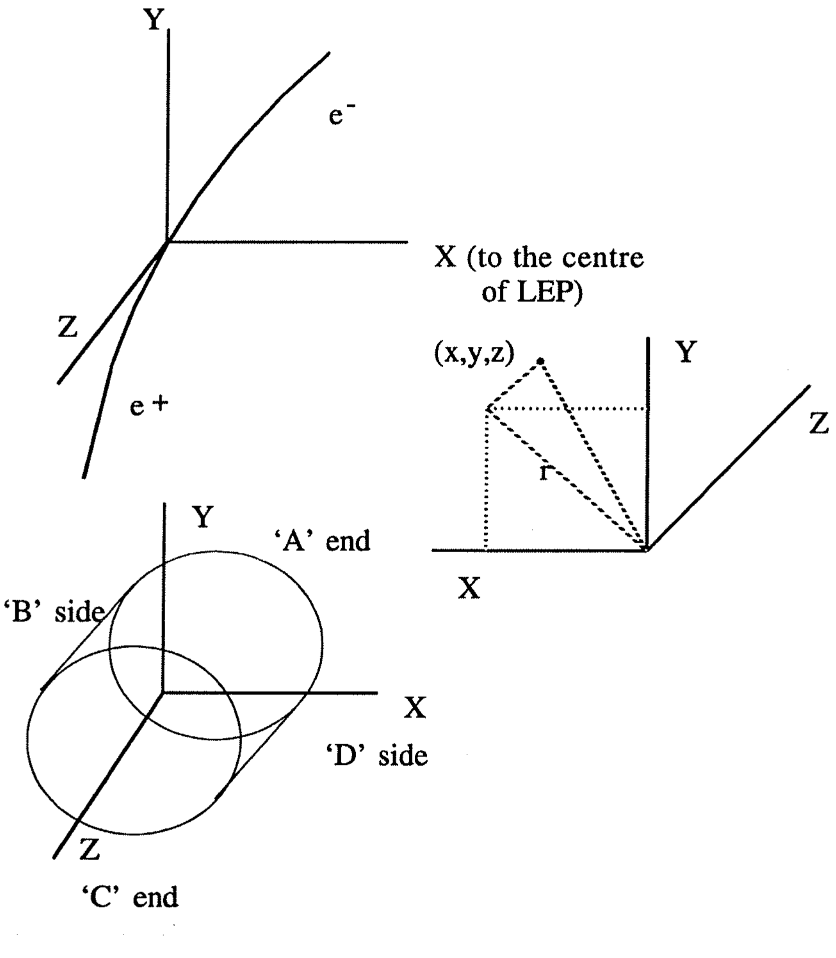

Figure B.1: DELPHI coordinate system.

Appendix C

Contents of Leptonic Microdst

On the microdst, all angles are given in degrees, distances in cm, energies in GeV and momenta in GeV/c. The data is organised in a modular form for storage efficiency and ease of use. The information for each event is as follows.

General event information

1) Run Number
2) Event number
3) LEP fill number
4) File sequence number
5) Centre of mass energy
6) Magnetic field
7) # reconstructed charged tracks
8) # reconstructed neutral tracks
9) # unassociated muon chamber TEs
10) Acolinearity (of two tracks with highest momentum)
11) Word containing B1 trigger bits
12) Word with Pythia trigger bits
13) Spare word
14) # energy clusters (TEs) in electromagnetic and hadronic calorimeters
15) Spare word
16) Number of data blocklets for the event:
= #reconstructed charged tracks + #reconstructed neutrals
+ 1 for extra muon hits
+ 1 for simulation blocklet
+ 1 for VD blocklet
+ #calorimetric TEs

then 1 word per blocklet:

17)
... 17+(# blocklets)-1) blocklet identifier+(blocklet length)*100

the blocklet identifiers are:

50:charged track, 51:neutral track, 52:extra muon hit, 53:simulation, 54:VD, 55:calorimeter TEs

For the two highest momentum tracks

The blocklets incorporate track information (24 words) and calorimeter information for one associated shower from CCA, ECA and HCA (12*3 words) together with associated muon chamber information (4+2*(#layers hit) words).

General track information

1) Blocklet identifier = 50
2) Quality word: bits flagging which detectors used in track fit
   bits 1-5 : ID, TPC, OD, FCA, FCB
3) Momentum
4) Theta of the track at the perigee
5) Phi of the track at the perigee
6) Charge
7) $\delta(p)/p$
8) $\delta(\theta)$
9) $\delta(\phi)$
10) track length
11) χ^2 of the fitted track
12) Isolation angle
13) DELANA mass code assigned to the track
14) Impact parameter (signed) - closest approach in Rϕ
15) z at closest approach in Rϕ
16) Time of flight from TOF
17) Error on time of flight
18) Word for outer detector timing information - not yet available
19) Total energy associated with the track by the Combined Calorimetry code
20) Total energy in the electromagnetic calorimeters associated with the track
21) Total energy in the hadron calorimeters associated with the track
22) Number of muon chamber hits associated with the track
23) TOF information (TDC+256*ADC) external
24) TOF extra blocklet word 8 (TDC+256*ADC) internal

Associated calorimetric information

1) sub-blocklet identifier for Combined Calorimetry (CCA)
2) Total associated energy (E) in CCA
3) $\delta(E)$
4) x coordinate of the start of the shower
5) y coordinate of the start of the shower
6) z coordinate of the start of the shower

7) θ direction of the shower
8) ϕ direction of the shower
9) DELANA mass identifier of the shower
10) dummy Three dummy words
11) dummy to make CCA blocklet
12) dummy standard

13) sub-blocklet identifier for electromagnetic calorimetry
14) Total associated energy (E) in FEMC and HPC
15) $\delta(E)$
16) x coordinate of the start of the shower
17) y coordinate of the start of the shower
18) z coordinate of the start of the shower
19) θ direction of the shower
20) ϕ direction of the shower
21) DELANA mass identifier of the shower
22) Layer information: number of layers hit
23) Layer pattern - if layer n is hit then bit $n-1$ is set
24) Detector identifier, so that FEMC can be distinguished from HPC

25) sub-blocklet identifier for hadron calorimetry
26) Total associated energy (E) in HCAL
27) $\delta(E)$
28) x coordinate of the start of the shower
29) y coordinate of the start of the shower
30) z coordinate of the start of the shower
31) θ direction of the shower
32) ϕ direction of the shower
33) DELANA mass identifier of the shower
34) Layer information: number of layers hit
35) Layer pattern - if layer n is hit then bit $n-1$ is set
36) Detector identifier

Associated muon chamber information

1) sub-blocklet identifier = 52
2) Number of layers in muon chambers associated with the track by EMMASS
3) Global χ^2
4) Expected number of missed layers

For each TER associated (up to 7), hit information:

1) Detector id*10 + submodule id*1000 + and doublet/triplet flag*10000 + whether TER is active(1)/deactive(0) after EMMASS
2) layer χ^2

Other charged tracks (up to 6)

For up to 6 tracks in addition to the two highest momentum tracks, a reduced track information blocklet (22 words) is included.

1) Blocklet identifier = 50
2) Quality word (as for first two tracks)
3) Momentum
4) θ
5) ϕ
6) Charge
7) $\delta(p)/p$
8) $\delta(\theta)$
9) $\delta(\phi)$
10) Track length
11) χ^2 of the fitted track
12) Isolation angle
13) DELANA mass code
14) Impact parameter (signed) - closest approach in Rϕ
15) z at closest approach in Rϕ
16) Time of flight from TOF, 9999 if there is no information
17) Error on TOF
18) Word for outer detector timing information (not yet available)
19) Total energy associated with the track by the Combined Calorimetry code
20) Total energy in the electromagnetic calorimeters associated with the track
21) Total energy in the hadron calorimeters associated with the track
22) Number of muon chamber hits associated with the track

Neutral tracks (up to 10)

A calorimetry information blocklet (11 words) for up to ten reconstructed neutral showers, giving the shower coordinates of the first shower associated to the neutral (looking at CCA, HPC/FEMC and HCAL in turn) is included.

1) Blocklet identifier = 51
2) Detector identifier (bitted word - bit 1 CCA, bit 2 HPC/FEMC, bit 3 HCAL)
3) shower energy in CCA
4) shower energy in HPC/FEMC
5) shower energy in HCAL
6) x coordinate of start of shower
7) y coordinate of start of shower
8) z coordinate of start of shower
9) θ direction of the shower (for HPC, otherwise dummy)
10) ϕ direction of the shower (for HPC, otherwise dummy)
11) DELANA mass id

Unassociated muon chamber hits

Unassociated muon hit information for up to 20 hits is included in this blocklet (3+9*(#hits) words).

1) Blocklet identifier = 52
2) Number of TERs for which information is recorded below
3) Total number of TERs that were present

for each TER, hit coordinates:

a) Submodule identifier
b) R
c) Rϕ
d) z
e) x
f) y
g) θ
h) ϕ
i) Doublet/triplet flag

Simulation information (if any)

Truth information from simulation for up to 10 charged and 10 neutral particles constituting: 5+(#charged particles + #neutral particles)*8 + #(total generations) words; including mass id's for each generation are included.

1) Blocklet identifier = 53
2) Number of charged particles for which information is recorded below (max 10)
3) Total number of charged particles that were present
4) Number of neutral particles for which information is recorded below (max 10)
5) Total number of neutral particles that were present

For each simulated particle - charged particles first then neutrals:

1) Momentum
2) Energy
3) θ at production
4) ϕ at production
5) Charge
6) Mass identifier
7) Number of generations
8) Number of generations recorded (up to 10)
9)
...9+(#generations)-1) Mass id's of particles. From initial to final state particles.

Track perigee parameter information

This blocklet (of length: 3+(#charged tracks)+(11*(#charged tracks)*2 words) provides additional track perigee parameter information for the two(or one) highest momentum charged tracks, giving the number of VD hits associated to the tracks and including the full error matrix on the track parameter set (θ,ϕ,1/p).

1) Blocklet identifier = 54
2) Number of charged tracks
3) Beamspot quality - 0 is good

4)
... 4+(#tracks)-1) #VD hits associated with the track

Two sets of the following track perigee parameters and errors are stored, corresponding to the values relative to the (x,y) beamspot positions of the nominal (0,0) and a run-by-run determined (x_{beam},y_{beam}), as discussed in subsection 3.5.1. Where available the VD information is used in DELANA's track fit that determines these parameters (in 1990 a post DELANA refit was performed to incorporate VD hits in the track fit).

for each track, two sets of:

1) signed impact parameter
2) z
3) θ
4) ϕ
5) 1/p (signed)
6) $\delta[\theta]^2$
7) $\delta[\theta\phi]$
8) $\delta[\phi]^2$
9) $\delta[\theta(1/p)]$
10) $\delta[\phi(1/p)]$
11) $\delta[(1/p)]^2$

Full calorimetry information

This blocklet (of length: 4+#(showers stored)*12) contains the calorimetric information for all showers associated and unassociated, from both hadron and electromagnetic calorimeters.

1) Blocklet identifier = 55
2) Total #words in this blocklet.
3) #calorimeter showers (CCA,ECAL,HCAL) in event
4) #calorimeter showers (CCA,ECAL,HCAL) stored in this blocklet

for each shower stored:

1) length of shower information block
2) calorimeter identifier (31:CCA, 9:HPC, 26:EMF, 13:HAB/HAF, [18:SAT])

3) shower energy
4) x coordinate of the start of the shower
5) y coordinate of the start of the shower
6) z coordinate of the start of the shower
7) DELANA mass id
8) θ direction of the shower (for HPC, dummy otherwise)
9) ϕ direction of the shower (for HPC, dummy otherwise)
10) HPC: number of clusters in the shower, otherwise number of layers hit
11) spare word

Case 1

In the case $p_1 = p_2$ the above gives $\alpha_{23} = \alpha_{13} = \alpha$, which makes $\alpha_{12} = 2\pi - 2\alpha$. Leading to :

$$p_3 = \frac{e \sin(2\pi - 2\alpha)}{2\sin\alpha + \sin(2\pi - 2\alpha)} = \frac{e\cos\alpha}{\cos\alpha - 1} \tag{E.5}$$

Case 2

For the situation $p_1 = p_c$,

$$p_c + p_2 + p_3 = e, \tag{E.6}$$

indicating that the momentum conservation triangle can be viewed as being 'inscribed' within an ellipse where p_c joins the foci on the major axis as shown in figure E.1. Consideration of special cases leads to the major and minor axis values

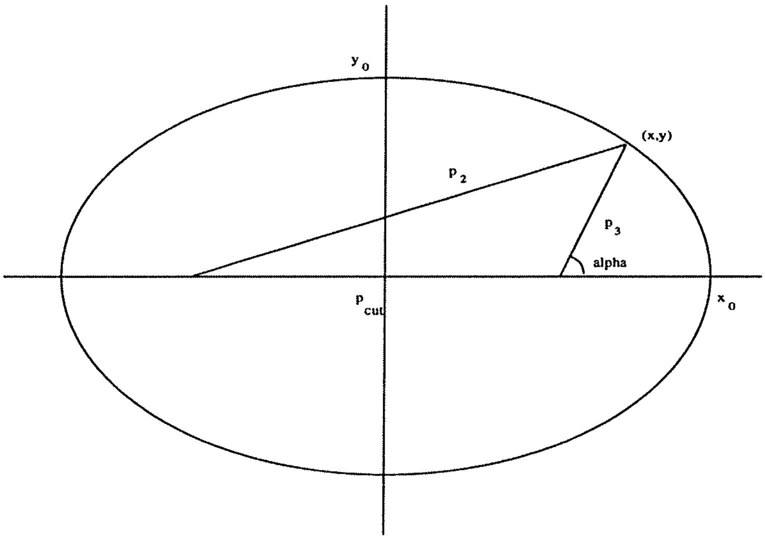

Figure E.1: Momentum conservation triangle 'inscribed' within an ellipse.

x_0 and y_0.

$$\begin{aligned} x_0 &= \frac{e - p_c}{2} \\ y_0 &= \sqrt{\left[\frac{e - p_c}{2}\right]^2 + \left[\frac{p_c}{2}\right]^2} \end{aligned} \tag{E.7}$$

The position (x,y) can be parameterized by ($\frac{p_c}{2} + p_3\cos\alpha$, $p_3\sin\alpha$). Thus in the equation of the ellipse, $(x/x_0)^2 + (y/y_0)^2 = 1$, a quadratic in p_3 is obtained. The positive root of the quadratic gives an expression for p_3 in terms of α, $p_3 = f_1(\alpha)$.

Appendix F

Glossary

BCO - Beam CrossOver
Blocklet - a piece of DELPHI data, beginning and ending with a word count, and having two words set aside for identifiers and error flags
CEB - Crate Event Buffer
CP - Crate Processor
C1-C5 - cuts made on charged tracks in the $\mu^+\mu^-$ analysis
DELANA - the DELPHI software for event reconstruction
DELFARM - the cluster of workstations where the DELPHI data is processed
DELGRA - the DELPHI graphics package
DELPHI - the DEtector with Lepton, Photon and Hadron Identification
DST - Data Summary Tape
E_{cm} - centre of mass energy
E_{em} - the amount of energy in the electromagnetic calorimeters associated with a track
E_h - the amount of energy in the hadron calorimeters associated with a track
E'_h - E_h with its angular dependence removed
with a track
FCA - Forward Chamber A
FCB - Forward Chamber B
FEMC - Forward Electromagnetic Calorimeter
FIP - Fastbus Intersegment Processor
FSR Event- an event with predominantly final state photons, as defined in section 5.2
HCAL - Hadron Calorimeter
HLB - Hit Latch Buffer
HOF - Forward Hodoscope (scintillators)
HPC - High density Projection Chamber - the barrel electromagnetic calorimeter
IBA - Improved Born Approximation, see section 1.6
ID - Inner Detector
ISR Event- an event with predominantly initial state photons, as defined in section 5.2
LEP - the Large Electron Positron collider
LES - Local Event Supervisor

LTD - LEP Time Digitizer
LT3P - Local Third level trigger process
MIP - Minimum Ionizing Particle
MSM - Minimal Standard Model
MUB - Barrel Muon Chambers
MUF - Forward Muon Chambers
MU1-MU3 - muon identification criteria for the $\mu^+\mu^-$ analysis
MWPC - MultiWire Proportional Chamber
N_{mux} - the number of hits in the muon chambers associated with a track
OD - Outer Detector
PS - Proton Synchrotron
PXDST - software which strips TANAGRA data down to DST data
RF - Radio Frequency
RICH - Ring Imaging CHerenkov detector
Run - Period of data taking
SAT - Small Angle Tagger - the luminosity monitor
SPS - Super Proton Synchrotron
TANAGRA - data structure for DELPHI data, containing information from all levels of the event reconstruction (TD to TV)
TB - Track bundle
TD - Track Data
TE - Track Element
TK - TracK
TV - Track Vertex
TOF - Time Of Flight scintillators
TPC - Time Projection Chamber
T1-4 - the first, second, third and fourth level triggers
VD - Vertex Detector